Skoltech

Skolkovo Institute of Science and Technology

Skolkovo Institute of Science and Technology

POLARITON LASING IN A DYE-FILLED ORGANIC MICROCAVITIES

Doctoral Thesis

by

TIMUR YAGAFAROV

DOCTORAL PROGRAM IN PHYSICS

Supervisor
Professor Pavlos Lagoudakis

Moscow - 2019

Abstract

Polaritons are half-light half-matter quasiparticles that arise from the interaction of confined in the microcavity photons with excitons in semiconductor material filling the cavity. Above a threshold density, polaritons are forming a macroscopic condensate in the ground polariton state, which decays through the microcavity mirrors in the form of photons. Thus, coherent emission observed from the microcavity and called polariton lasing. Large exciton binding energies are required to obtain the polariton lasing at ambient temperature. Electron-hole pairs localized on a single molecule in organic semiconductors represented by Frenkel excitons with high binding energies (0.5 - 1 eV), that is why organic materials are applicable in room temperature polaritonics. Polariton lasing in a strongly-coupled organic microcavity observed over a broad spectral range spanning 2.1 – 3 eV. However, tuneability over the polariton emission wavelength on a single material system has proven challenging.

In the present thesis, a material system is proposed to generate polariton lasing at room temperature over a broad spectral range. The active layer of a strongly-coupled microcavity based on boron-dipyrromethene fluorescent dye. The study utilized a single pulse dispersion imaging technique to probe the condensate properties within each pulse individually. We found that polaritons undergo non-linear emission over a broad range of exciton–cavity mode detuning, and polariton lasing achieved over a spectral range spanning 33 nm.

Another aspect of the work is a polariton condensates blueshift which is present across a diverse range of organic materials at increasing polariton density. While the mechanism for blueshifts in inorganic semiconductor microcavities hosting Wannier-Mott excitons corresponds to the interparticle Coulomb exchange interactions, the localized nature of Frenkel excitons in molecular semiconductors suppresses their contribution for organic polaritons. Thus, a new explanation for the ubiquitously observed blueshift is needed. We examine the contribution of intracavity optical Kerr-effect, gain induced frequency-pulling, quenching of the vacuum Rabi-splitting and renormalization of the cavity mode energy due to saturation of optical transition in strongly- and weakly-coupled

2

molecules, as well as the role of polariton-exciton and polariton-polariton scattering in the energy-shift of the polariton mode at condensation threshold in strongly-coupled molecular dye microcavities. We conclude that blueshifts in organic polariton condensates arise from the interplay of the saturation of molecular optical transitions and intermolecular energy migration. For the first time, we consider the role of weakly-coupled molecules and show a significant contribution of cavity mode renormalization on the observed polariton blueshift in organic microcavities. Our model predicts the commonly observed step-like increase of both the emission energy and degree of linear polarisation at polariton condensation threshold.

Keywords: blueshift, BODIPY-G1, fluorescent dyes, exciton-polaritons, light-matter interactions, organic microcavities, polariton lasers, polariton condensate, strong coupling.

Publications

1. D. Sannikov, T. Yagafarov, K. Georgiou, A. Zasedatelev, A. Baranikov, L. Gai, Z. Shen, D. Lidzey, and P. Lagoudakis, Room Temperature Broadband Polariton Lasing from a Dye-Filled Microcavity. *Advanced Optical Materials*, **7**, 1900163 (2019)

(SD and TY have an equal contribution, except samples fabrication).

2. Timur Yagafarov, Anton Zasedatelev, Denis Sannikov, Kyriacos Georgiou, Anton Baranikov, Oleksandr Kyriienko, Ivan Shelyk, Lizhi Gai, Zhen Shen, David G. Lidzey, Pavlos G. Lagoudakis, On the origin of blueshifts in organic polariton condensates, *ArXiv*. (2019) arxiv.org/abs/1905.02573

(TY contributed into this work, except samples fabrication (KG and DL), Z-scan measurements (AB), microscopic description of Rabi saturation (OK and IS) and numerical simulations (AZ)).

3. Pramod M Rajanna, Evgenia P. Gilshteyn, Timur Yagafarov, Alena K. Aleekseeva, Sergey Anisimov, Alex Neumüller, Oleg Sergeev, Sergey Bereznev, Jelena Maricheva, Albert G. Nasibulin, Enhanced efficiency of hybrid amorphous silicon solar cells based on single-walled carbon nanotubes and polymer composite thin film, *Nanotechnology*, **29**, 105404 (2018).

(TY contributed with optical characterization of Transmittance and Reflectance for films and study the effect of ARC of polymer).

There is no conflict of interests with authors of publications.

Acknowledgements

I want to express my appreciation to:

- My supervisor, Pavlos Lagoudakis, for taking me under his wing and performing weekly meetings, fool of fruitful discussions. Especially I am thankful for being the first team member and taking part in the creation of the beautiful Hybrid Photonics lab at Skoltech, which was perfectly organized by Pavlos and Mael Brossard.

- I am grateful to Mael Brossard for his attention, prompt response, and his care of us in various situations.

- Denis Sannikov, for being my scientific partner and friend during all the investigations present in this thesis. I am very thankful for his life advice, which he shared with me during countless hours of work in the lab.

- Anton Zasedatelev, whose strong knowledge and helpfulness in any time of the day were critical and supportive for me. I appreciate a lot his personal qualities that stimulated me to develop, to be like him.

- Sergey Alyatkin, whose in-depth methods of investigations impressed me a lot and who taught me in the very beginning of PhD. He has motivated me in the times I was upset about not having good results. Thank you, Sergey!

- My neighbour, colleague, and friend, Anton Baranikov, for his bright mind and infinite scientific discussions. I am happy that there is a friend I could always rely on and that we have done this way together with him.

- My colleague Kirill Sitnik for spending the night shifts on holidays with me in the lab – this time will always be in my memory, as well as his "Voyage" motivation.

Table of Contents

List of Figures

represent numerical simulations of time-integrated blueshifts, respectively. (b) The blueshift ΔE versus exciton-fraction for 5% (blue) and 10% (res) samples, solid curves show the best-fit results

transition, respectively. Here we saturate the transition for the 10 percent. (b) The ratio $\rho = \frac{\Delta E_{LPB}^{c}}{\Delta E_{LPB}^{\Omega}}$ shows relative contributions of renormalization in the cavity mode energy and the Rabi-quenching term to overall polariton blueshift as a function of exciton-photon detuning

List of Tables

Chapter 1. Introduction

A laser is a unique optical device with beneficial properties including directionality, monochromatic emission with high intensity and large coherence length. The first solid-state ruby laser [1] demonstrated in 1960 has caused a significant breakthrough in science and technology. The ability of precise control over spectral, spatial and temporal characteristics of lasers has modified the field of spectroscopy and provided previously hidden insights into the physics of the surrounding world with high orders of sensitivity and resolution [2]. Facilitated by the rapid development and improvements, lasers continuously introduced to the new fields. Nowadays, they are considered for medicine, telecommunications, microscopy, everyday life in the form of printers, DVD players, pointers, and so on. Typically, the above lasers are based on inorganic semiconductor materials and doped crystals. These materials have a significant disadvantage: generally, they are fragile, nonflexible, require expensive epitaxial grow techniques and high vacuum conditions. Moreover, realization of the wavelength tuneability in these systems is challenging [3,4].

Material studies have played an essential role in the development of new organic semiconductor lasers which have competitive advantages compared to inorganic ones. Due to ease in the processability of organic semiconductors, the organic laser can be fabricated on numerous types of substrates and realized in various optical resonator architectures and different states, for example, like a solution dye laser [5,6] or typical solid-state laser based on dyes in the polymer [7]. Diversity of organic materials with high quantum yield discovered to date and their emission spans over the broad range of wavelengths, providing

an opportunity to realize an efficient wavelength-tuning in a visible spectral range. The mentioned advantages lead to the low cost, broadly tuneable organic lasers which are suitable for spectroscopy applications or the optical devices, where the reach colors are required, for example, in the light-emitting diodes or microdisplays.

However, other benefits and further improvements could appear if polaritonics concepts applied to organic laser. In the usual laser device, lasing can only happen when population inversion is achieved. In contrast, the polariton lasing does not require population inversion due to the final state bosonic stimulation mechanism, and polariton lasing takes place before population inversion builds up. Described concept of polariton laser with potentially low activation threshold has been theoretically investigated by Imamoglu [8] in 1996 and was then experimentally demonstrated in 2006 by Deng *et al*. [9]. For the study, Deng used an inorganic microcavity and found that the threshold for polariton lasing was ~ 2 orders lower than the threshold for inversion of population. In 2016 Dietrich *et al*. [10] performed a similar experiment on reduced threshold observation in a fluorescent protein-based organic microcavity. These investigations gave the possibility of fabrication of ultra-low threshold organic polariton lasers. That is why organic polaritonics is a rapidly developing and perspective field today.

Initially, polaritonics was mainly considered in frames of inorganic materials with Wannier-Mott type of excitons, where low binding energies of latter limited the polaritonics application to cryogenic temperatures operations. However, in organic materials, we meet another, Frenkel type of excitons, which feature is high binding energies of $0.5 - 1$ eV. As binding energies in organic semiconductors higher than room temperature

thermal energy (~30 meV), organic materials can be stable in ambient conditions and room temperature polariton lasing can be achieved. The first room-temperature organic polariton laser without population inversion has its roots in the late '90s. Specifically, in 1998, Lidzey *et al.* [11] managed to demonstrate the strong coupling in an organic microcavity at room temperature: confined in the microcavity photons interacted with excitons from tetra-(2,6-t-butyl)phenol-porphyrin zinc organic molecules dispersed in a polymer matrix. This light-matter interaction gave rise to the creation of new polariton modes in the system, which were observed from the angular reflectivity measurements of the microcavity. On that stage, the possibility of polariton lasing at room temperatures was only mentioned, and it took more than a decade to demonstrate it. In 2010, the first organic polariton lasing was shown on crystalline anthracene film by Kena-Cohen and Forrest [12]. Authors realized, that after some polariton density threshold, a non-linear polariton lasing, accompanied by a dramatic increase in emission intensity, blueshift and linewidth narrowing, observed from the cavity. This work has triggered intense studies on the various organic materials application to ambient polaritonics. The following material applied was conjugated MeLPPP polymer, and in 2013, Plumhoff *et al.* [13] produced a comprehensive set of experimental evidence for polariton lasing. Moreover, the emergence of long-range phase coherence was proved by interferometry measurement: the polariton emission sent into a Michelson interferometer and interference pattern of the inverted image, overlapped with the original one, was obtained.

To date, polariton lasing achieved on strongly-coupled organic microcavities, which utilize various organic materials: crystalline organic molecules [12], conjugated

polymers [13], oligofluorenes [14], fluorescent proteins [10,15] and molecular dyes [16,17]. Emission from these materials covers the significant part of the visible spectrum in a broad spectral range spanning 2.1 – 3 eV. However, tuneability over the polariton emission wavelength on a single material system has proven to be challenging and was not studied to date.

One remarkable feature of the organic polariton lasing observations [13,14,16–18] is a polariton condensates blueshift which causes the change of the polariton lasing emission wavelength and complicates the precision of wavelength tuneability. The blueshift is present across diverse organic materials at increasing polariton density. While the mechanism for blueshift in inorganic semiconductor microcavities with Wannier-Mott excitons corresponds to the interparticle Coulomb exchange interactions [19,20], the localized nature of Frenkel excitons in molecular semiconductors suppresses such interactions for organic polaritons. Thus, a new explanation for the largely observed non-linear response is needed.

In the present thesis, original and novel investigations manifesting the possibility of precise control over a polariton lasing emission wavelength and explanations of the mechanisms underlying blueshifts in organic polariton condensates are described. These results can potentially pave the way to the creation of a cost-effective and perspective type of room-temperature organic polariton lasers based on strongly-coupled microcavities with high precision of wavelength tuneability.

1.1 Outline

In Chapter 2, the brief introduction into the light-matter coupling principles will be given. It starts with the consideration of the photons and excitons confined in the planar microcavity and the strong-coupling condition, which provides rise to exciton-polaritons in organic microcavities. The exciton-polaritons states will be described. Finally, we will consider the polariton condensation (lasing) process in the organic microcavities, as well as mechanisms which are contributing to the condensate formation.

Chapter 3 is addressed to the polariton lasing wavelength tuneability realization at room-temperature. Organic microcavity with the specific architecture will be described, as well as the developed experimental setup. Room-temperature strong coupling and lasing, observed in a broad spectral range, will be reported.

Chapter 4 is dedicated to the investigation of the blueshift origin in organic polariton condensates. The same strongly-coupled molecular dye microcavities from the previous Chapter 3 were used to find the new explanation for the widely-observed non-linear response. The different processes which could cause the blueshift were examined: the contribution of intracavity optical Kerr-effect, gain induced frequency-pulling, quenching of the vacuum Rabi-splitting and renormalization of the cavity mode energy due to saturation of optical transition in strongly- and weakly-coupled molecules, as well the role of polariton-exciton and polariton-polariton scattering in the energy-shift of the polariton mode at condensation threshold in strongly-coupled molecular dye microcavities. Finally, we will provide evidence that the blueshifts in organic polariton condensates arise from the interplay of the saturation of molecular optical transitions and intermolecular

energy migration. For the first time, the role of weakly-coupled molecules will be considered, and significant contribution of cavity mode renormalization on the observed polariton blueshift in organic microcavities will be shown. Additionally, the model which predicts the commonly observed step-like increase of both the emission energy and degree of linear polarization at the polariton condensation threshold will be suggested.

Chapter 5 summarizes the conducted research. The primary outcomes will be stated, and further outlooks for improvements in the organic polaritonics field will be suggested.

Chapter 2. Light-matter coupling in organic microcavity

2.1 Strongly-coupled organic microcavity

The concept of polaritonics is based on the light-matter interaction principles, where the photons, which represent the light part, are strongly-coupled with the representatives of the matter part – the excitons. To have an opportunity for coupling both types of particles should be mixed up together and placed in the same confined area. Such localization could be performed when the microcavity structure is used.

2.1.1 Cavity photons

Microcavity is an optical resonator where light can be confined in the form of standing wave [21]. There are different types of the cavity realizations, but since in our experiments we are dealing with the light confinement in one direction, in this section, we will consider the planar Fabry-Perot microcavity. Such microcavity typically consists of two strictly parallel planar reflectors with the space between them. Usually, reflectors are represented by the metallic mirrors or by the distributed Bragg reflectors (DBRs); the latter were used in the studied structures. DBR is a periodic structure of two altering dielectric materials with low and high refractive indexes. By maximizing the materials' refractive index contrast and optimizing the thickness and number of the layers, a high-reflectivity DBR mirror with a broad region of efficiently reflected wavelengths (stopband) can be fabricated [22]. In **Figure 2.1**, the schematic is provided for the typical microcavity, which consists of two DBRs separated by the cavity material layer of thickness L_c and refractive index n_c.
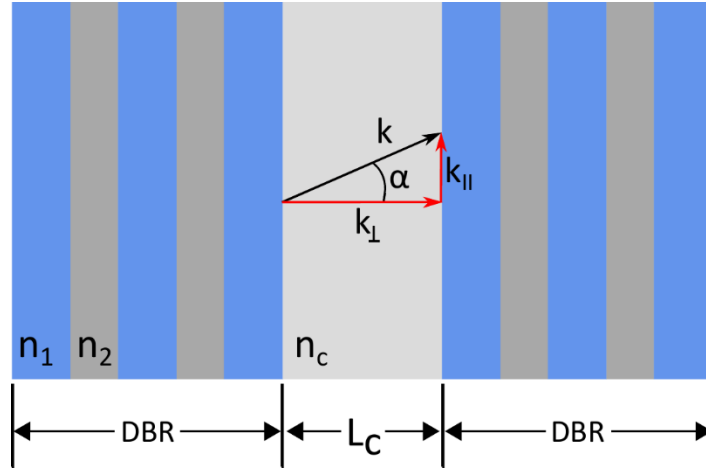
Figure 2.1. Schematic of a planar microcavity which consists of the layer with refractive index n_c and thickness L_c, placed between two DBRs. DBRs are composed of two materials of low and high refractive indexes n_1 and n_2, respectively. Photons are confined inside the cavity with total wavevector k_0 which is a composition of perpendicular $k_\perp$ and parallel $k_{||}$ parts.

Reflections of light waves between the cavity DBRs cause constructive or destructive interference with different wavelengths in the optical resonator, as a result of which, the standing electromagnetic waves, called modes, are confined inside the cavity [23]. The wavelength of the photons, which are restricted in the cavity, can be determined by the cavity thickness and reads as:

$$\lambda_c = \frac{2n_c L_c}{m} \cos \alpha \qquad (2.1)$$

where *m* corresponds to the number of half-wavelengths, which present in the cavity, and can have integer values ≥ 1, and α is the angle of propagation of photons with wavevector k measured from the DBR's normal plane, as shown in Figure 2.1. Wavevector k of confined photons can be written as:

$$k = \frac{2\pi}{\lambda_c} = \frac{\pi m}{n_c L_c \cos \alpha} \tag{2.2}$$

If we want to find the wavevector components, as one can mention from Figure 2.1, they can be easily expressed with $k_\perp = k \cos \alpha = \frac{\pi m}{n_c L_c}$ and $k_{||} = k \sin \alpha = \frac{\pi m}{n_c L_c} \tan \alpha$.

In order to find the energy of the photon mode inside the cavity, the following formula is used:

$$E_c = \hbar c k = \frac{\pi m \hbar c}{n_c L_c \cos \alpha} = E_0 (1 - \sin^2 \alpha)^{-\frac{1}{2}} \tag{2.3}$$

$$\text{where } E_0 = \hbar c k_\perp = \frac{\pi m \hbar c}{n_c L_c}$$

As we can see, the energy of the cavity mode can be described as a function of the angle of propagation, and that is why termed as the cavity mode dispersion. It is worth noting that α is the angle of propagation inside the cavity. Since we observe the light coming out from the cavity when performing the measurements, we need to make a correction which takes into account refraction of the light for an external observer. It is usually performed with the use of Snell's law with the outside medium refractive index equal to 1 (air) and an angle of observation α', which is calculated from the microcavity normal. In that way, the previous formula for the microcavity mode dispersion reads as follows:

$$E_c = E_0 \left(1 - \frac{\sin^2 \alpha'}{n_c^2} \right)^{-\frac{1}{2}} \tag{2.4}$$

To observe an angular distribution of the microcavity mode experimentally, one can perform the reflectivity measurement, which essence is the following. An angle of white light source incidence onto the microcavity (consisting from DBRs and free space between them) is gradually changed, and the detection angle symmetrically tuned (angle of incidence = angle of detection); by stitching the reflectivity spectra measured in described configuration, an angle-dependent reflectivity plot can be extracted. Simulations of the reflectivity plot from an empty microcavity, taken and adapted from [24], are shown in **Figure 2.2**. The cavity mode is observed approximately in the middle of the microcavity stopband at different angles.
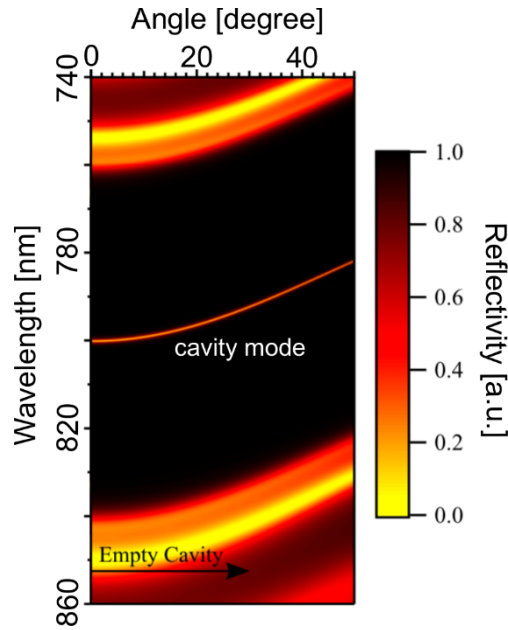
Figure 2.2. Angle-dependent reflectivity plot simulated for the empty microcavity. Adopted from [24].

An essential characteristic of the microcavity is the quality factor Q which physically compares the time of energy storage to the losses rate. It can be mathematically

extracted [25] from the microcavity mode wavelength, λ_c, and its full width at half of maximum, $\delta\lambda_c$, as:

$$Q = \frac{\lambda_c}{\delta\lambda_c} \tag{2.5}$$

The relationship between the Q factor and the lifetime of the resonator mode, or the same as the lifetime of photons, is:

$$Q = \omega_c \tau \tag{2.6}$$

$$\text{where } \omega_c = \frac{2\pi c}{\lambda_c}$$

2.1.2 Frenkel excitons

There are two main types of semiconductors, where we can observe the excitons – inorganic semiconductors with a crystalline structure and molecular organic semiconductors. As the latter used in the present thesis experiments, in this section, we will primarily focus on the excitons in organic semiconductors.

Exciton is a quasiparticle composed from the oppositely charged electron and hole which are bonded together by the Coulomb forces. Band structure of organic semiconductor consists of the molecular orbitals [26]. Usually, at room temperatures, an electron can be found at the highest occupied molecular orbital (HOMO), which is the ground state denoted as S_0. The lowest excited state of the electron is called the lowest unoccupied molecular orbital (LUMO) and denoted as S_1. Once the light absorption excites the electron ($S_0 \rightarrow S_1$ transition), the exciton is created, and it can recombine either radiatively with the emission of photon or non-radiatively through phonons (in inorganic

28

semiconductors) or vibrons (in organic semiconductors) emission. Vibron is the quantum of intermolecular vibration [26], and vibronic levels are usually denoted with index v in the energy state nomenclature $S_{1,v}$ [27].

The electron-hole pair distance is called the exciton Bohr radius and defined as:

$$a_B = \frac{4\pi\hbar^2\varepsilon\varepsilon_0}{\mu e^2} \tag{2.7}$$

where $\hbar$ is the reduced Plank constant, ε is the permittivity of the medium, ε_0 is the vacuum permittivity constant, e is the elementary charge and μ is the effective mass of the exciton. In organic semiconductors, the electron-hole pair is present on the same molecule, and such type of excitons is expressed by the Frenkel excitons [28]. The Bohr radius of Frenkel excitons possess the values of the order of ~ 10 Å (for inorganics' Wannier-Mott excitons [29,30] it is ~ 100 Å) and corroborates with the high exciton localization on the molecule [31]. Such localization also contributes to the exciton binding energy, which is the energy needed to ionize the electron-hole pair, and given by the formula:

$$E_B = \frac{\hbar^2}{2\mu a_B^2} \tag{2.8}$$

Mostly, for Frenkel excitons in organic materials, the binding energy is $\sim 0.1 - 1$ eV, and for Wannier-Mott excitons in inorganics, it is of the order of ~ 10 meV [31]. As the room temperature thermal energy approximately equals 30 meV, the binding energies comparison above makes it clear why the organic materials are stable, and inorganic – not stable at room-temperatures.

2.1.3 Exciton-polaritons

Since we already considered microcavity photons and excitons, now we can combine both of the worlds in order to describe the light-matter interaction which contributes to the rise of exciton-polaritons (here and after polaritons) in the organic-filled microcavity.

When an organic semiconductor material is placed inside the cavity and photons are introduced (microcavity mode in resonance with molecular optical transitions), photons can be absorbed by the cavity medium, and therefore excitons created. After some time, excitons will recombine and emit the photons again, which in turn can be reabsorbed and reemitted repeatedly with the characteristic energy exchange frequency Ω_0 called vacuum Rabi frequency. When the quality factor of microcavity is high enough, the lifetime of the photons will also be high, and they will stronger interact with the matter. Such interaction is usually affected by the microcavity photon decay rate γ_1 and the exciton decay rate γ_2. If the energy exchange between the photons and excitons in microcavity happens much faster than any dissipations in the system, $\Omega_0 >> (\gamma_1, \gamma_2)$, then the strong coupling regime is realized [32].

In the strong light-matter coupling regime, the efficient energy exchange between the cavity photons and the excitons results in the creation of the new quasiparticles – polaritons, which possess the properties of both the photon and the exciton [33]. The closest classical analogy to the interacting exciton and photon modes inside the microcavity is the coupled harmonic oscillators task. Imagine that we have two pendula, which initially oscillate at natural frequencies (like photon and exciton resonances). If we couple them

through the spring, as schematically shown in **Figure 2.3**, the energy exchange between pendula is realized. If the spring constant k much bigger than the oscillation dissipation rate of each oscillator (analogically to strong coupling condition above), we would expect that pendula will start to oscillate at different frequencies (like polariton modes occurring in microcavity) than each pendulum initially.
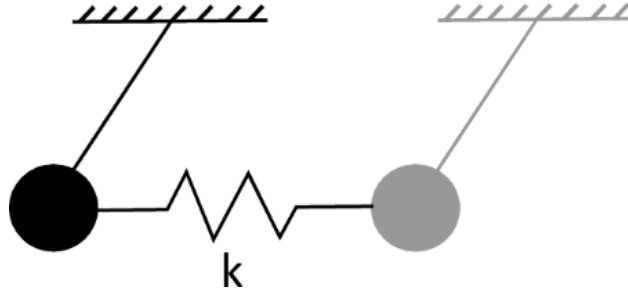
Figure 2.3. Two coupled pendula exchanging with energy through a spring.

The strong coupling criterion mentioned above is rather intuitive than strictly defined. The further clarification of strong coupling condition can be considered from the spectroscopic criterion which says that the measurable splitting of two polariton states can be resolved if the frequency splitting is bigger than the sum of the linewidths of loss rates $\Omega_0 > \frac{|\gamma_1 + \gamma_2|}{2}$, according to [34]. Sure, that definition is reasonable in terms of the experimental approach, however, if one wants to access the strength of the coupling, the proper figure of merit would be the ratio $\frac{\Omega_0^2}{\omega_0 \gamma}$, where $\gamma = \frac{(\gamma_1 + \gamma_2)}{2}$ is the loss rate, and ω_0 is the eigenfrequency of the bare oscillators. If the ratio $\frac{\Omega_0^2}{\omega_0 \gamma} > 1$, there is an efficient energy exchange between oscillators and the system appears in the strong coupling regime [35].

The coupled harmonic oscillator model [20,36] can be used for the extraction of the new eigenstates of the strongly-coupled system. The Hamiltonian of the system is described as:

$$\hat{H} = \begin{pmatrix} E_X & \dfrac{\hbar\Omega_0}{2} \\ \dfrac{\hbar\Omega_0}{2} & E_C \end{pmatrix} \tag{2.9}$$

where E_C is an angular-dependent cavity photon mode (see Equation 2.4), E_x is an exciton energy eigenstate (which is almost flat due to high exciton mass), $\dfrac{\hbar\Omega_0}{2}$ is the interaction potential of the cavity photon-exciton mode coupling. From the above Hamiltonian the standard expressions for polariton modes appearing in the strongly-coupled microcavity, Upper Polariton Branch (UPB) and Lower Polariton Branch (LPB), can be obtained in the following explicit form [23]:

$$E_{UPB,LPB} = \frac{1}{2}\left(E_C + E_X \pm \sqrt{\delta^2 + (\hbar\Omega_0)^2}\right) \tag{2.10}$$

where $\delta = E_C - E_X$ is the exciton-photon detuning, and $\hbar\Omega_0$ is the vacuum Rabi splitting.

A polariton wavefunction in terms of the bare photon and exciton states can be expressed as a coherent superposition of both components:

$$\psi_{pol} = |X|^2\psi_X + |C|^2\psi_C \tag{2.11}$$

where $|X|^2$ and $|C|^2$ are the Hopfield coefficients reflecting excitonic and photonic contributions, respectively. They can be found from:

$$|X|^2, |C|^2 = \frac{1}{2}\left(1 \pm \frac{\delta}{\sqrt{\delta^2 + (\hbar\Omega_0)^2}}\right) \tag{2.12}$$

The typical dispersions for LPB and UPB in the case of negative, zero, and positive detunings are shown in **Figure 2.4**. The top and bottom solid curves correspond to the UPB and LPB, respectively, and dashed curves are the bare cavity and exciton modes.
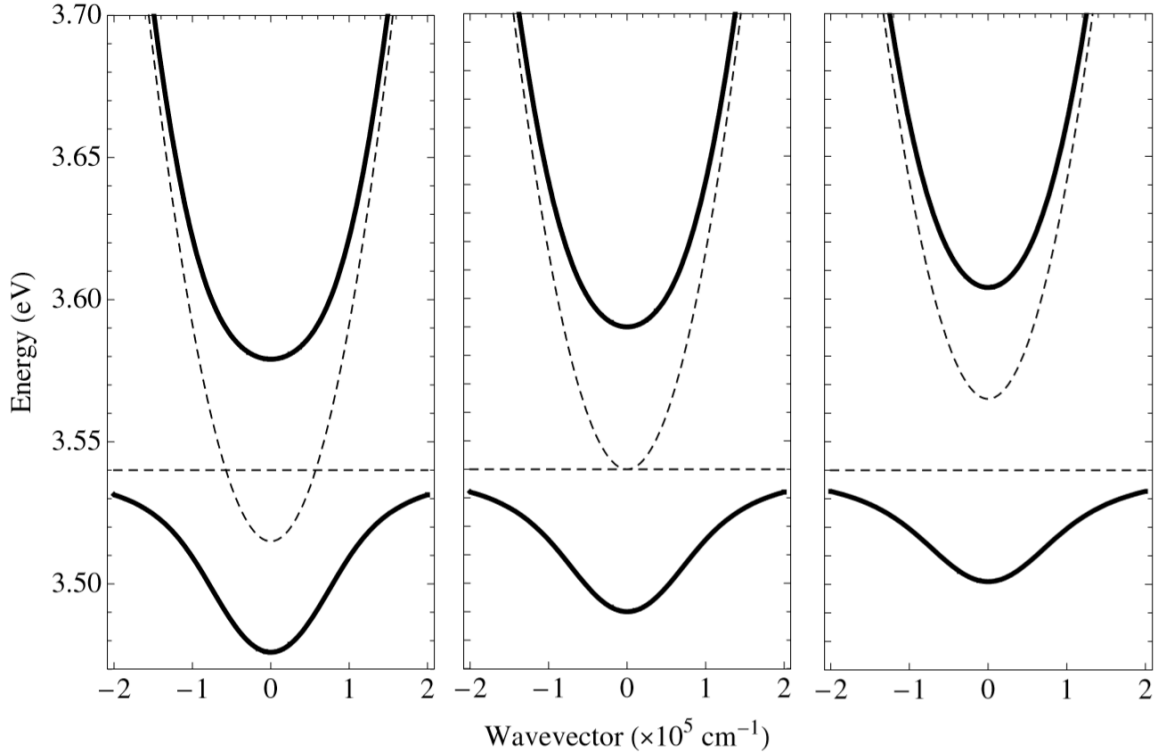
Figure 2.4. Energetic distribution of exciton-polariton modes at negative, zero and positive detunings (from left to right). Solid lines correspond to exciton-polariton modes dispersions, dashed – to the bare exciton and photon modes. The figure is adopted from [23].

Like in the case of microcavity mode dispersion (described in Section 2.1.1), one can perform the reflectivity measurement by exciting the strongly-coupled organic microcavity in the linear regime with white light at different angles of incidence. By stitching the spectra, the color-plot like in **Figure 2.5** can be obtained. The UPB and LPB are seen as the deeps in reflectivity spectra from organic-filled microcavity recorded at

various angles. Color-plot can be fitted by the coupled harmonic oscillator model described above; dashed lines are the fits of bare cavity and exciton modes, solid – of UPB and LPB.
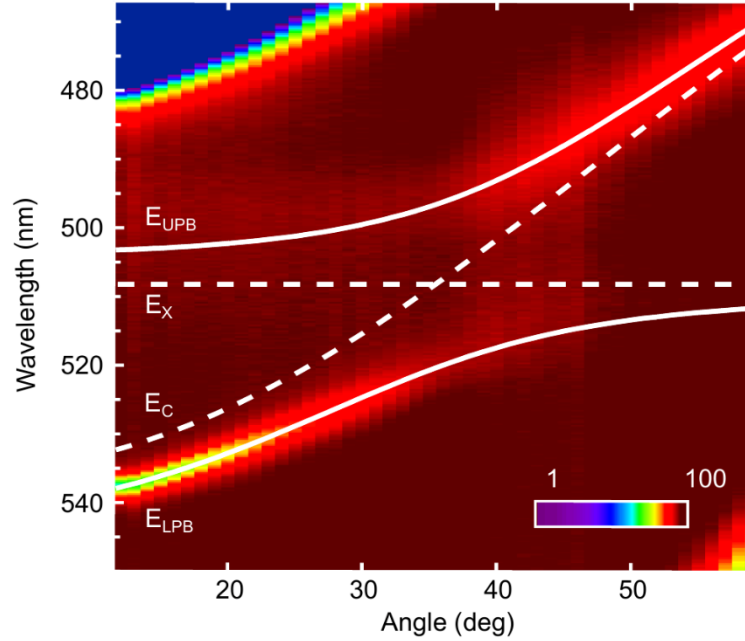
Figure 2.5. Angle-dependent reflectivity plot for strongly-coupled microcavity being fitted with coupled harmonic oscillator model. Color bar is the reflectivity scaling. Note, here the sides of the reflectivity stopband are seen in the corners.

2.2 Polariton lasing in organic microcavity

In the previous section, we considered the polaritons formation in strongly-coupled organic microcavities. It is worth mentioning that experimentally observed polariton modes (see Figure 2.5) are measured in the linear regime (i.e., before the condensation threshold). In the linear regime, polaritons are distributed along the polariton mode and leaking in the form of photons due to the microcavity lifetime; that is why the photoluminescence from the cavity is observed [37]. Once the polariton density is

34

increased, the non-linear regime (above the threshold of polariton condensation) can be realized, and polariton lasing observation is possible. In this section, we will consider the properties of the polariton lasing as well as the processes which are leading to the non-linear phenomenon in organic microcavities.

2.2.1 Mechanisms of polariton condensation in organic microcavity

As we already learned from section 2.1.3, polariton consists of two components, namely exciton and photon. Although exciton consists of electron and hole which are fermions, exciton by itself exhibit a bosonic nature. Since the photon is a boson too, the polariton will also demonstrate the bosonic behavior [38]. One of the essential characteristics of such behavior is that one state can be occupied by a number of bosons [39] (contradictory to the Pauli exclusion principle, which prohibits such occupation for fermions). Another significant property of bosonic particles is the final state bosonic stimulation mechanism [40], which rate of transition to the final state is proportional to ($N_{\text{final}} + 1$), where N_{final} is the final state occupancy. The combination of both bosonic properties leads to the stimulated relaxation of polaritons into the final state when their densities increased [41], i.e., polariton condensation. Once polariton condensation happened, a coherent emission from the microcavity can be detected, and it is called polariton lasing. (*Regarding the disputes on the terminology in polaritonics community [42–45], it will be worth to mention that further in the thesis we will use the term polariton condensation, or polariton lasing, in terms of collective behavior of bosonic

particles (polaritons), without the strict necessity of the system equilibrium – the property essential for Bose-Einstein condensates). The polariton lasing emission has common features with a conventional photon lasing; however, from a fundamental point of view, they are significantly different. The first difference is the relaxation process, which is being stimulated in case of polariton lasing, and spontaneous for photon lasing. Secondly, there is no need for population inversion for polariton lasing, that is why the power thresholds can be lower than for photon lasing [8–10]. The last difference is that in polaritonic systems, coherence builds-up upon the polariton condensation in the final state, while in the photon laser the stimulated emission of radiation coming from the cavity is the final bosonic state. Due to the last property, we can externally study the polariton state inside the cavity by observation of the photons, which are flying out from the system and carrying all the information about the polariton condensate energy, wavevector, phase, and polarization.

The next thing to consider is the relaxation mechanisms of excitons into polariton state. It is worth noting that in the experiments, which will be described in the next chapter, we used non-resonant excitation, that is why here we would be limited to the consideration of the case of non-resonant optical excitation of the organic microcavity. Corresponding mechanisms are schematically shown in **Figure 2.6**. Under optical excitation of high energy E_{pump}, excitons relax to the incoherent state of energy E_0 by emitting the vibrons, which were mentioned in Section 2.1.2. This excitonic state is called exciton reservoir, and energy E_0 usually corresponds to the molecular optical transition of the intracavity material. Once the exciton reservoir is formed, it can contribute to the polariton states

population either radiatively, or non-radiatively. In the first case, the light emission (usual PL) directly populates the upper and lower polariton coherent states. In the second case, excitons are relaxing via emission of the vibrons and populate the states of the lower polariton branch.
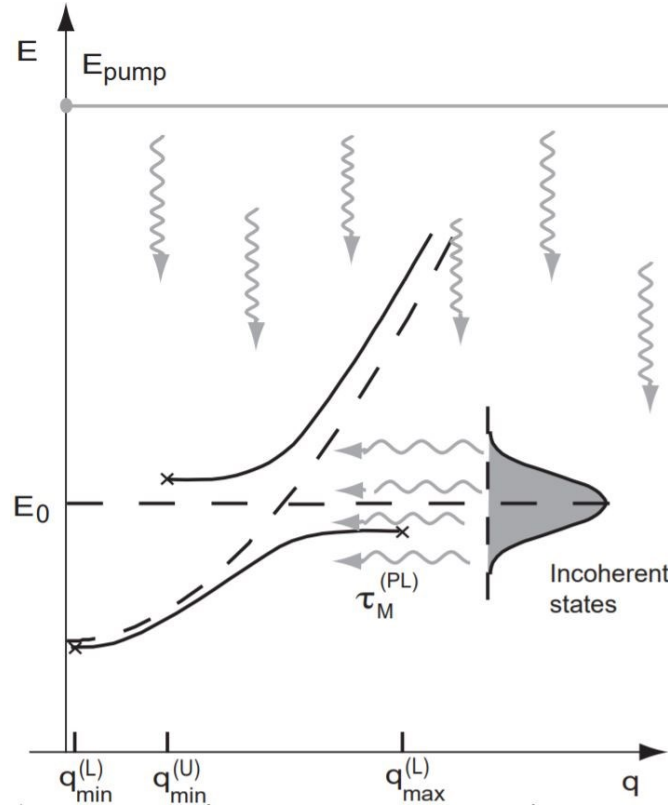
Figure 2.6. Schematic of the relaxation processes in the organic microcavity under non-resonant excitation E_{pump}. After vibronic relaxation, excitons are forming the reservoir in E_0 and can contribute to the polariton state via further radiative or vibronic relaxation mechanisms. Adopted from [46].

For the experimental observation of the polariton lasing dispersion and concepts described above, the well-established Fourier plane imaging technique in 2f-configuration is typically used [47]. Recorded with the use of such a method exemplary dispersion images of the polariton distribution in non-resonantly pumped organic microcavity are

presented in **Figure 2.7**. Here, we can observe only the part of the lower polariton branch which is limited by the numerical aperture of the collection objective. Since microcavity is the system with losses, there is a pump power threshold where polariton condensation and corresponding lasing can occur. Below that threshold, polaritons are distributed along the LPB (Figure 2.7(a)), like in reflectivity measurements (as was shown in Figure 2.5). Nevertheless, above the threshold, polaritons collapse to the lower polariton branch bottom as shown in Figure 2.7(b), and polariton lasing is observed with the characteristic intensity increase, linewidth narrowing, and the blueshift. Latter will be discussed in Chapter 4.
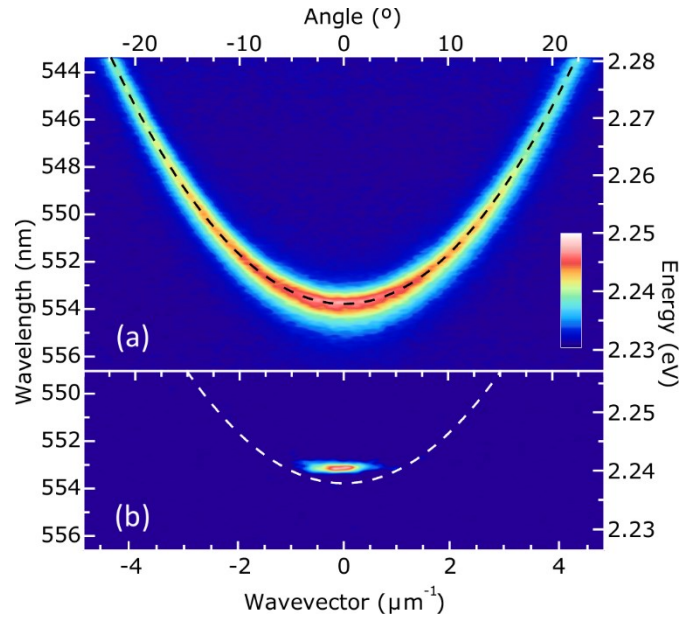
Figure 2.7. Polariton dispersions of non-resonantly pumped organic dye-filled microcavity taken below(a) and above(b) the condensation threshold. Above the threshold, initially distributed along the LPB polaritons (dashed line) collapse to the bottom of LPB and form the macroscopic condensate.

Chapter 3. Room temperature broadband polariton laser

3.1 Introduction

Exciton-polaritons induced intense research around different disciplines last decades. As a result, the new field of polaritonics appeared, which is rapidly developing today. Initially, optoelectronics driven by light-matter strong coupling principle [23] was mainly focused on GaAs-based inorganic semiconductor microcavities [33]. However, several crucial points make an application of inorganic III-V semiconductors into polaritonics field complicated. The first reason - is the challenging and expensive growth techniques used in wide-bandgap semiconductors fabrication. Another limitation is dictated by Wannier-Mott excitons nature, which compulsory requires the use of cryogenic temperatures for longer lifetimes of excitons [48,49] and strong coupling possibility. That is why the broadest class of the developed to date strongly-coupled microcavities is represented by organic materials which do not have mentioned disadvantages; facilitated by the cheap and straightforward fabrication and possessing high binding energies, organic semiconductor microcavities permit the applications and physics of polaritonics being investigated at ambient conditions [11,50]. Collective behavior of exciton-polaritons in a polaritonic system leads to the non-linear phenomena, and polariton lasing is the most distinctive one. Polariton lasing, driven by a stimulated relaxation to a coherent state, does not require the electronic inversion of population. Thus, the potential for room temperature organic polariton lasers with significantly lower thresholds than in usual photon lasers of the same device configuration is discovered [9,10,51].

Developed to date polariton lasers based on strongly-coupled organic microcavities utilize various classes of materials, such as biologically produced fluorescent proteins [10], crystalline organic molecules [12], conjugated polymers [13], oligofluorenes [14], and molecular dyes [16,17]. All mentioned materials showed the possibility to obtain a polariton lasing in a broad visible spectrum range of 2.1 – 3 eV. However, the realization of the tuneable control over polariton lasing wavelength in frames of a single material system remains challenging. Here, in chapter 3, we investigate the potential of broadband tuneable polariton lasing based on organic microcavity filled with boron-dipyrromethene (BODIPY) fluorescent dye molecules, which dispersed in transparent polystyrene (PS) matrix.

3.2 Sample fabrication and characterization

All samples used in the present thesis were fabricated in the University of Sheffield by our collaborators. For the active medium, the typical representative of the BODIPY dye family was used, namely, the molecular dye BODIPY-G1, which is owning both high extinction coefficients and high photoluminescence quantum yield [52].

3.2.1 BODIPY-G1 film

The active medium film for microcavity has been prepared in the following sequence. To create an optically inert matrix solution, PS with a molecular weight of M_w = 192000 was dissolved in toluene at a concentration of 35 mg mL^{-1}. After that, the BODIPY-G1 dyes powder was dispersed in a prepared matrix solution at 10% concentration by PS mass. The use of polymer is essential since it allowed to disperse the

molecular dyes uniformly in the solution and the final solid film; moreover, PS is optically transparent for the visible spectral range [53,54], that is why it is commonly used as the matrix in the various spectroscopic application [55–57]. Following the described procedure, a solution for the active medium layer was prepared.

To study the optical properties of the film, which have to be applied to the microcavity, we prepared the control bare (non-cavity) film for absorption and photoluminescence (PL) measurements. We used a widely employed spin-casting technique, which is proven to be cost-effective, highly reproducible, and reliable for microstructures fabrication [58]. The concept of spin-casting method is simple: a viscous solution of the material that has to be deposited (in our case, it is a BODIPY-G1 dye and PS dissolved in toluene) is cast on the fixed planar substrate which is then accelerated up to a high rotational speed. Due to the centrifugal force, a significant part of the solution rapidly flies away from the substrate. Remaining on the substrate film continue to become thinner due to the material outflow and solvent evaporation (toluene in our case), and finally, a thin solid film on the substrate created from a polymer with dyes dispersed in it. By the control over material concentration in the solvent, rotational speed, and processing time, the different film thicknesses could be obtained.

An absorption of 172 nm thickness control bare film from BODIPY-G1 in PS matrix created on quartz glass was measured on "Fluoromax 4, Horiba" fluorometer equipped with a Xe lamp. For PL measurement, the film was excited using a 473 nm laser diode, and PL was then detected using an "Oriel MS-125" spectrograph. A normalized absorption and photoluminescence spectra are represented in **Figure 3.1** with black and

red curves, respectively. The absorption maximum of the film occurs at 507 nm with the photoluminescence being Stokes shifted to 524 nm. Inset corresponds to the chemical structure of the BODIPY-G1 molecule.
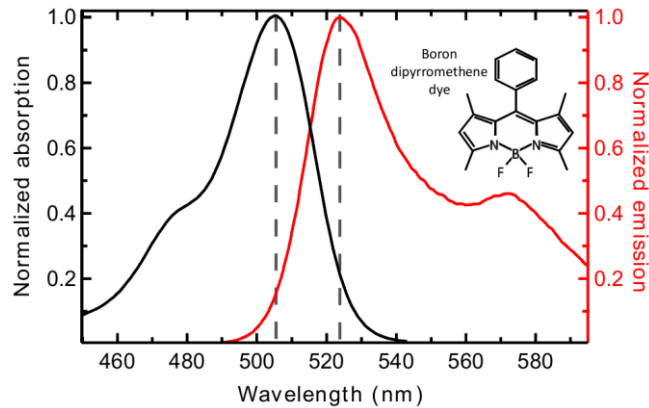
Figure 3.1. Normalized absorption (black) and photoluminescence spectrum (red) of a 172 nm thick film from the BODIPY-G1 dye dispersed into a polystyrene matrix. Inset is the chemical structure of BODIPY-G1.

Another essential characteristic of the active medium is a material optical gain. The material gain spectral region is usually indicated by the amplified spontaneous emission (ASE) [59,60]. ASE is a process where spontaneously emitted luminescence is amplified. This process has non-linear dependence on pumping density and occurs when population inversion is achieved. On the same control film, we explored ASE using the stripe excitation method [61], which is schematically shown in **Figure 3.2**. A 355 nm wavelength pulsed laser at 1 kHz repetition rate (v) with 350 ps pulse width was focused with a 25 mm cylindrical lens on the sample. Excitation had a stripe profile with dimensions of 1470 μm x 80 μm. ASE emission from the control bare film was detected from the edge of the film, in a direction perpendicular to the propagation of the incident pump beam, using an "Andor Shamrock" CCD spectrometer. Measurement results, shown in **Figure 3.3**, revealed that

BODIPY-G1 undergoes optical gain. The maximum of the optical gain spectrum was centered at 547 nm as indicated by the fluorescence emission narrowing at a pump power of $P_{th} = 6 \, mW$, or incident excitation density of:

$$\frac{P_{th}}{S * v} = \frac{6 * 10^{-3} \, [W]}{1470 * 80 * 10^{-8} \, [cm^2] * 1000 \, [Hz]} = 5.1 \, [mJ \, cm^{-2}]$$
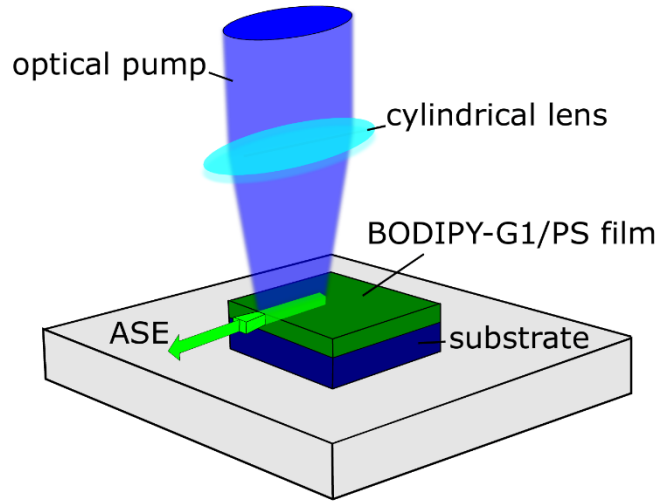
Figure 3.2. Schematic of the ASE setup. The cylindrical lens focuses the optical pump in the stripe on the film. ASE observed from the side of the film.
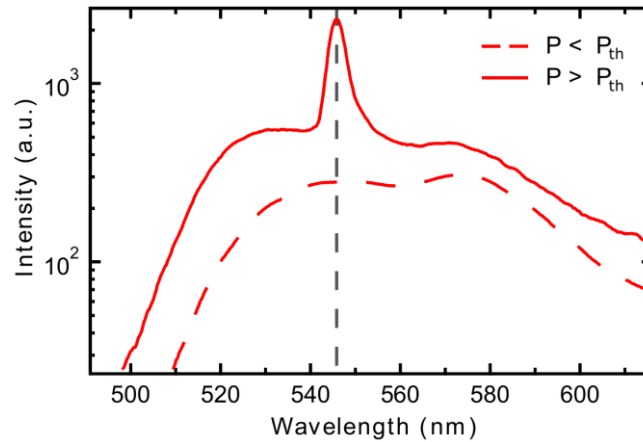
Figure 3.3. Emission spectra (dashed) of the bare film under stripe beam excitation. The dye molecules undergo amplified spontaneous emission (solid) at an incident excitation density of ≈ 5 mJ cm^{-2}, with the maximum of the material gain occurring at 547 nm.

43

3.2.2 BODIPY-G1 microcavity

To fabricate organic microcavities for polariton lasing and its tuneability investigations, a bottom DBR, consisting of ten pairs of SiO_2/Nb_2O_5, was deposited onto a quartz-coated glass substrate using an ion-assisted e-beam [62] for Nb_2O_5 and reactive sublimation [63] for SiO_2. On top of the bottom DBR, the BODIPY-G1/PS film was spin-casted following the same receipt as for control bare film above. Microcavity was then completed by eight-paired top DBR deposited onto organic film; during the deposition of first layers, ion-gun was kept turned-off to avoid damage of the organic material by ions. Microcavity is schematically illustrated in **Figure 3.4**. The produced structure allowed achieving the detuning variation due to the wedge-like thickness gradient of the cavity material, which occurred during the spin-casting process. As the centrifugal force induced casting solution to move toward the edges of the substrate, and toluene evaporated during
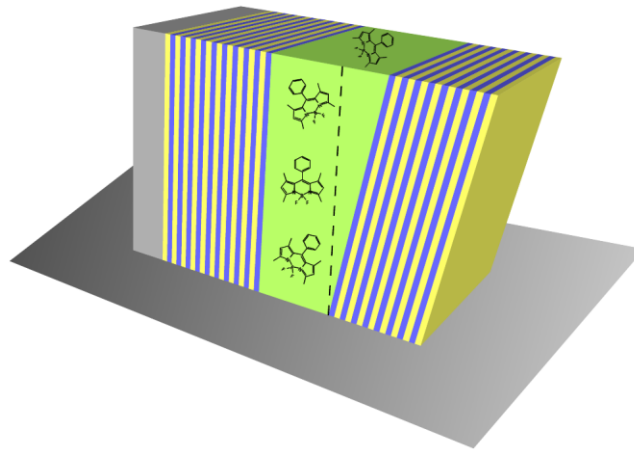
Figure 3.4. Schematical representation of the dye-filled microcavity with a wedge architecture.

the process, the viscosity of the remaining solution increased for the time film being formed. As a result, the film thickness gradually increased (up to 10 nm/cm) toward the

44

edges of the sample. Therefore, the cavity length and corresponding cavity mode E_C were changing. It is clear that polariton states, which are dependent on vacuum Rabi splitting energy $\hbar\Omega_0$, exciton mode E_X, cavity mode E_C, and detuning $\delta = E_C - E_X$, should also be changed according to:

$$E_{UPB,LPB} = \frac{1}{2}\left(E_C + E_X \pm \sqrt{\delta^2 + (\hbar\Omega_0)^2}\right) \qquad (3.1)$$

From a practical point of view, such microcavity architecture is beneficial to use. It allows to access controllably different cavity lengths, and thus, select preferred energy of the ground polariton state. Thereby, the wavelength of polariton lasing, which expected to emit from the lower polariton state, has an opportunity to be tuned. However, this idea will work only if the strong coupling is kept over a whole range of detuning conditions.

To prove the concept, we fabricated four microcavities with different exciton-photon detunings by controlling the thickness of the active medium layer (was ranging from 130 to 180 nm) via the substrate rotation speed during spin-casting. The next was to check if the fabricated microcavities supported a strong coupling regime in the full detuning range. For that purpose, we performed an angular reflectivity measurement with the fiber-coupled "Ocean Optics DH-2000" Halogen–Deuterium white light source. The angle incidence on the sample of the white light source was controlled via a motorized arm. The reflected from the sample light was coupled into an optical fiber mounted on a second motorized arm which controlled the detection angle. The collected PL was then coupled to the "Andor Shamrock" charge-coupled device spectrometer. A typical angular-dependent reflectivity color plot measured from one spot on microcavity is represented in **Figure 3.5**.
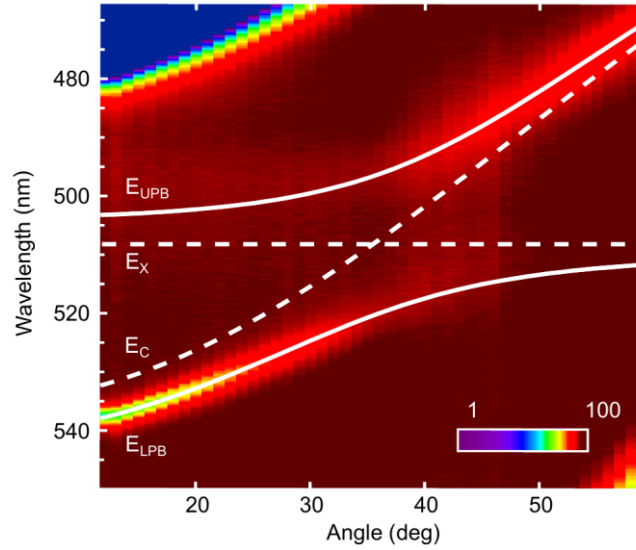
Figure 3.5. Angle-dependent reflectivity color plot for the BODIPY-G1 dye-filled microcavity (log scale). The solid lines show the calculated upper and lower polariton branches. The dashed lines correspond to the bare cavity and exciton modes. UPB, LPB, cavity and exciton modes were extracted from the coupled harmonic oscillator model.

Here the upper and lower polariton branches appeared in the angular reflectivity plot and underwent an avoided crossing at ~ 507 nm; a wavelength near the $S_0 \rightarrow S_1$ optical transition of the molecular dye. The presence of anticrossing of the upper and lower polariton modes at ~ 35° is the evidence that the system supports a strong coupling regime [11,23,50]. We observed the same strong coupling behavior in every measured point for all microcavities; and it is worth noting that the detuning was varying from sample to sample, as well as from point to point in frames of one sample. To find a whole accessed detuning range, we fitted the angular dependent reflectivity data (as shown in Figure 3.5) with the coupled harmonic oscillator model, considered in section 2.1.3. The microcavity effective refractive index n_{eff} and the cut-off energy of the cavity mode $E_c(0)$ were variable parameters; exciton energy eigenstate $S_{1,0}$ was $E_x = 2.446\ eV$.

According to the fitting results presented in Table 1, the refractive index homogeneously distributed along 1.81 ± 0.024 across the broad negative exciton-photon detuning range spanning $[-240; -120]\ meV$. The vacuum Rabi splitting $\hbar\Omega_0 = 116 \pm 2\ meV$ was almost invariant with respect to the detuning and fitted nicely within the vacuum Rabi splittings range observed in organic microcavities in the recent review paper on organic polaritonics [49]. With increasing of the detuning value, we observed a gradual rise of the exciton fraction $|X_{k_\parallel=0}|^2$ from 5% to ~ 13%.

δ, meV	n_{eff}	$\hbar\Omega_0, meV$	$|X_{k_{\parallel}=0}|^2$	$|C_{k_{\parallel}=0}|^2$
-239	1.77	114	0.049	0.951
-230	1.80	118	0.055	0.945
-226	1.80	118	0.057	0.943
-209	1.81	114	0.061	0.939
-195	1.79	116	0.070	0.930
-189	1.79	116	0.074	0.926
-187	1.78	120	0.079	0.921
-180	1.79	116	0.080	0.920
-175	1.80	116	0.083	0.917
-165	1.84	116	0.091	0.909
-160	1.82	116	0.095	0.905
-156	1.82	117	0.100	0.900
-148	1.84	114	0.104	0.896
-140	1.84	117	0.116	0.884
-135	1.83	114	0.118	0.882
-129	1.84	114	0.125	0.875
-127	1.84	112	0.125	0.875
Average + STD	*1.81±0.024*	*116±2*		

Table 1. Fitting results for the effective refractive index n_{eff}, Rabi splitting $\hbar\Omega_0$, exciton fraction $|X_{k_{\parallel}=0}|^2$, and photon fraction $|C_{k_{\parallel}=0}|^2$ extracted from particular points of reflectivity measurement for all fabricated microcavities.

From the performed investigations, we concluded that organic microcavities filled with BODIPY-G1 dyes support a strong coupling regime in the whole accessible range of negative detuning and, therefore, can be tested further for the polariton lasing wavelength tuneability realization.

3.3 Experimental setup

To investigate polariton lasing and its tuneability, a single pulse dispersion imaging setup, schematically presented in **Figure 3.6**, was designed and assembled. We used single pulses of 2 ps duration from "Coherent Libra" Ti:Sapphire laser which were frequency-doubled through a barium borate crystal providing a non-resonant excitation of microcavity at 400 nm wavelength. After the filtering, the pump beam was focused onto a microcavity by "Nikon Plan Fluor 4X" microscope objective (numerical aperture of 0.13) in ≈ 12 μm full width at half maximum (FWHM) spot size. Microcavity was fixed on 3D-scanning stage which allowed to access the whole surface of the sample and thus select the different exciton-photon detunings. Afterward, outcoming photoluminescence was collected in transmission configuration (see top right inset in Figure 3.6) using "Mitutoyo Plan Apo 20X" microscope objective with a numerical aperture of 0.42. To cut the residual light from the excitation beam off, a long-pass filter "Semrock LP02-442RU" used after the collection objective. Filtered photoluminescence from microcavity coupled into a "Princeton Instruments SP2750" 750 mm focal length spectrometer, which was equipped with an electron-multiplying charge-coupled device camera "Princeton Instruments ProEM-HS 1024×1024". To record dispersions, we introduced a k-space lens which was positioned to image the Fourier plane [64] (one focal length behind a collection objective) onto the

Single pulse dispersion imaging setup
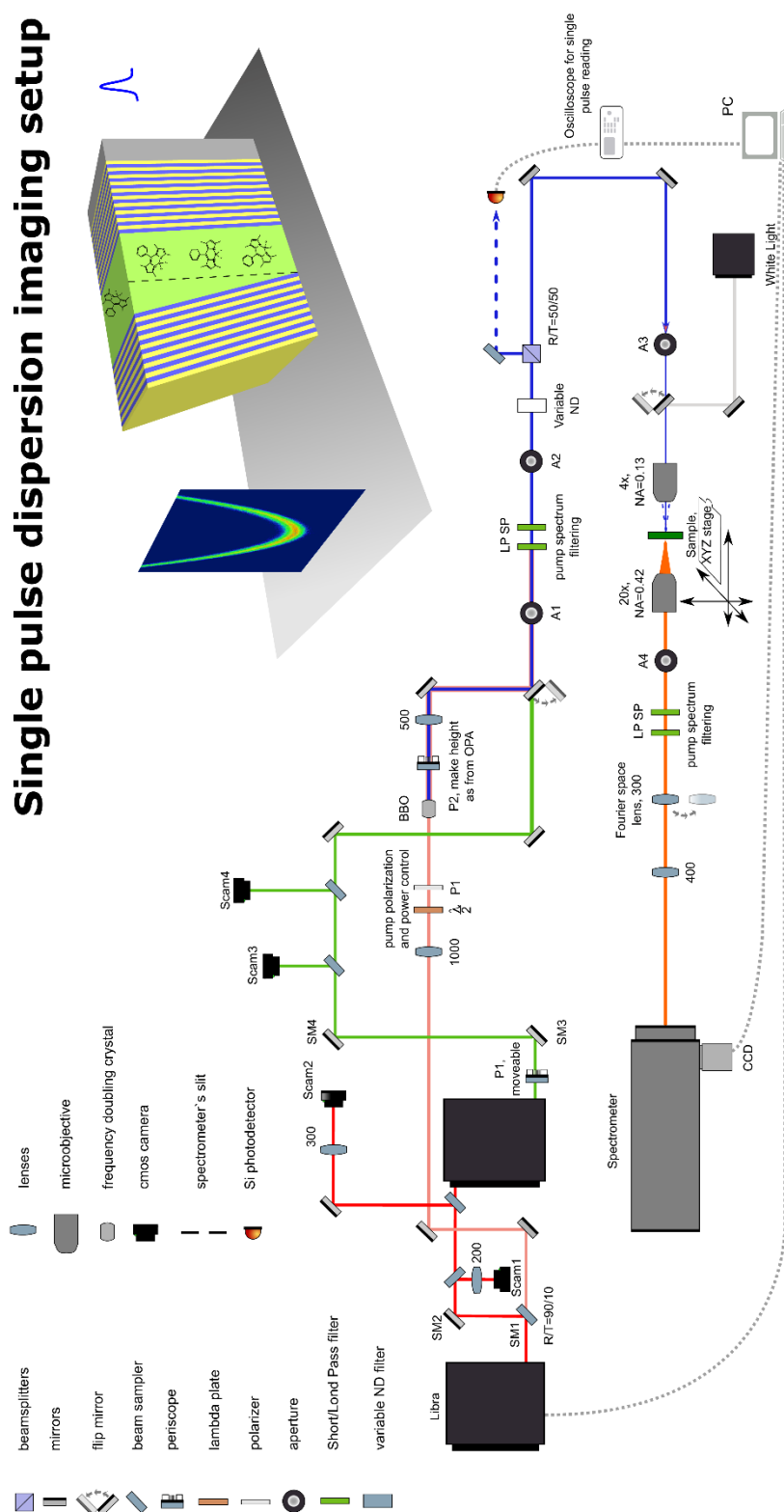
Figure 3.6. Scheme of single pulse dispersion imaging experimental setup designed for tuneable polariton lasing investigations.

49

spectrometer slit. A 20 µm entrance slit and 1200 grooves mm^{-1} grating were used to achieve a spectral resolution of 0.03 nm. The CCD recorded a polariton emission dispersion for each excitation pulse of known power, which was measured with the initially calibrated "Thorlabs DET10A" Si-detector connected to the "Keysight DSOX2012A" digital oscilloscope. The experiment with the control over all variable parameters was automated with the self-produced LabView code. All measurements were performed in ambient conditions at room temperature.

3.4 Results and discussions

3.4.1 Polariton lasing in the BODIPY-G1 molecular dye-filled microcavities

All microcavities were measured in the described above configuration. By scanning the strongly-coupled microcavities, we observed the polariton lasing dispersion images over the full detuning range. The typical polariton dispersion at the most negatively detuned point on the sample (−248 meV) is shown in **Figure 3.7**. The right half-panel represents a normalized time-integrated (note, that emission intensity from single pulse below the threshold was extremely low, that is why we integrated ~ 100 pulses) polariton photoluminescence distribution collected from the part of the lower polariton branch (approximately ± 7°) below the condensation threshold. Once the pump power of a single pulse became higher than the condensation threshold, the polariton photoluminescence from microcavity collapsed to the bottom of the LPB (approximately ± 0.5°) as shown on the left half-panel of Figure 3.7. The red dashed curve is the LPB fit, and the white dashed curve is the fit for the corresponding cavity mode.

50
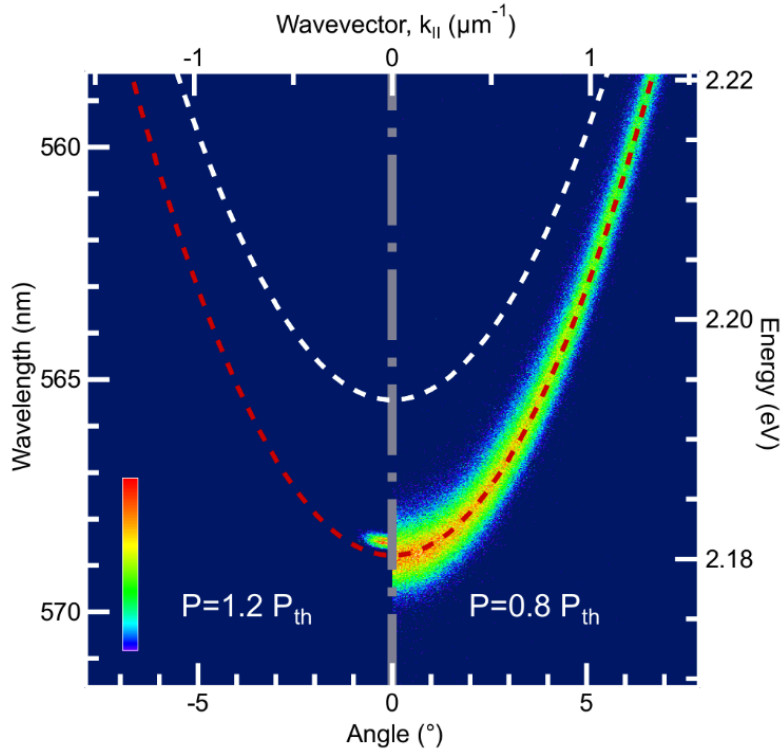
Figure 3.7. Normalized E,k - dispersion of polariton photoluminescence below (right) and above (left) the condensation threshold. Red and white dashed curves are attributed to the lower polariton branch and the bare cavity mode, respectively.

To understand the polariton lasing behavior on excitation density, we measured the dependence of photoluminescence intensity, FWHM, and energy shift as a function of the pump fluence, which was incident on the microcavity (measurements were taken in the same spot as dispersions described above). These analyses we performed by measuring the dispersions at different pump fluences. The photoluminescence intensity was integrated over ±1° at $k_{II} = 0$ (which corresponds to normal incidence on the sample). The result of excitation density dependence is shown in **Figure 3.8(a)**. Initially linear growth of the polariton emission intensity followed by a rapid increase of 2 orders occurring at ≈ 6 mJ cm^{-2} of incident excitation density - the process indicative for a threshold of the nonlinear
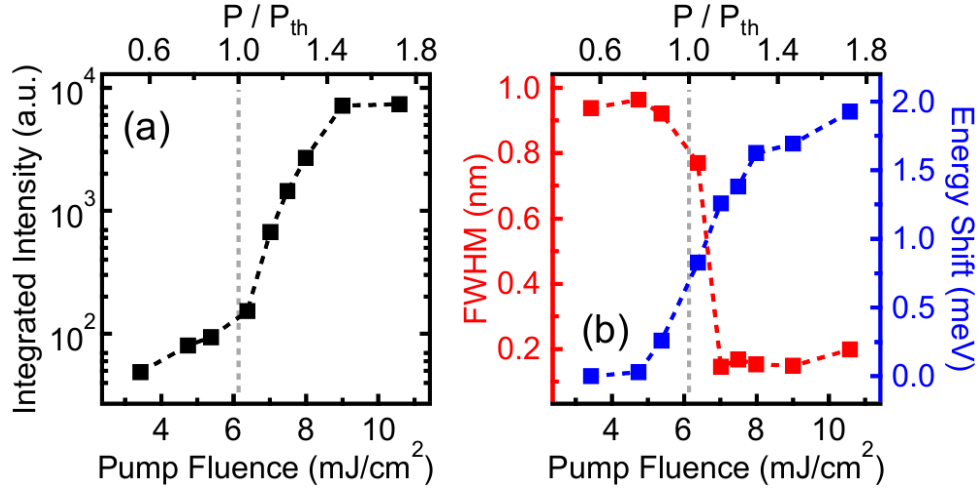
Figure 3.8. a) Dependence of the polariton photoluminescence intensity on incident pump fluence. b) The linewidth of polariton photoluminescence at FWHM (red) and the energy shift of the polariton mode at $k_{II} = 0$ (blue) versus pump fluence.

regime. In Figure 3.8 (b), the FWHM of the emission linewidth (red curve corresponding to the left axes) and the polariton condensate energy shift (blue curve, right axes) dependences on excitation density are depicted. The data was extracted from the Gaussian fit of the intensity profiles of polariton dispersions integrated over $\pm 1°$ around $k_{II} = 0$. The energy of the LPB at the lowest pump density was taken as zero level to define an energy shift value. At excitation density of the condensation threshold, we observed a narrowing of the emission linewidth, which is typical for a lasing process, and blueshift of the lower polariton mode commonly associated with the polariton lasing in the strongly-coupled microcavities. The tenfold linewidth narrowing from 1 to 0.1 nm reflected a high degree of coherence of ≈ 1 ps.

3.4.2 Polariton and photon lasing threshold comparison

An important thing to note is that during the experimental realizations of polariton

52

lasing, we have not observed photon lasing. To understand where the photon lasing might take place, we performed a comparison of the ASE threshold with the threshold for polariton lasing observation. As was described in section 3.2.1, the ASE threshold for the bare film was found at 5.1 mJ cm^{-2} of incident excitation density. For the sake of precision in comparison, we should rely on an absorbed excitation density. Thus, the incident pump fluence corresponding to the ASE threshold can be recalculated in absorbed pump fluence with the use of Burger law: $A = -log(\frac{I}{I_0})$, where A – absorbance of the sample (measured in section 3.2.1), I – the intensity of light leaving the sample, and I_0 – the intensity of light incident on the sample. The difference between incident and leaving intensities will provide us with an absorbed component. From absorbance measurement, we found that absorbance for BODIPY-G1 film is A = 0.025 at 355 nm excitation wavelength. Thus, an absorbed pump fluence at the ASE threshold:

$$I_0 - 10^{-A} * I_0 = 5.1\ [mJ\ cm^{-2}] - 10^{-0.025} * 5.1\ [mJ\ cm^{-2}] = 285\ [\mu J\ cm^{-2}]$$

The polariton lasing from microcavity occurred at 6 mJ cm^{-2} of the incident pump fluence at 400 nm. To find the pump fluence absorbed in the intracavity film, we used the same approach described above, but with a correction for a definition of the light intensity incident on the intracavity film, (I_0), which will be reduced by the reflection of the first microcavity DBR. For that purpose, we implemented the method described in Appendix 1 and found out that after the first DBR only 4.8 mJ cm^{-2} is incident on the BODIPY-G1 film inside the cavity. The absorbance of the film at 400 nm was found to be 0.011. Using the Burger law, we obtained an absorbed pump fluence for the polariton lasing:

$$I_0 - 10^{-A} * I_0 = 4.8 \, [mJ \, cm^{-2}] - 10^{-0.011} * 4.8 \, [mJ \, cm^{-2}] = 120 \, [\mu J \, cm^{-2}]$$

Following this analysis, we concluded that the threshold for polariton lasing (120 μJ cm-2) was ~ 2.5 times lower than for ASE (285 μJ cm-2). It is worth noting that this is the rough approach to estimate the absorbed pump fluence threshold. In real systems, the threshold for polariton lasing is expected to be less than the estimated value because of scatterings and the leaky tunneling modes [65] which are usually present inside the microcavity. Moreover, for the ASE threshold, we also note that the area excited on the sample (1470 μm x 80 μm) was much bigger than the tightly focused spot we used in lasing realization (d ≈ 18 μm). Since the ASE threshold power reduces when the excitation area is increased [66], we expect a higher threshold value than estimated.

From the comparison performed, one can expect that the photon lasing requires at least 2.5 times higher pump fluence compared to the threshold for polariton lasing. We found that the microcavity samples photo-degraded at absorbed pump fluence two times higher than the polariton lasing threshold value. Thus, we were not able to reach the photon lasing threshold, which could appear from the cavity mode indicated by white dashed parabola in Figure 3.7.

3.4.3 Polariton lasing emission tuneability

Having established a polariton lasing in the most negatively-detuned point, we proceeded to examine the fabricated structures in the full exciton–photon detuning range to investigate the wavelength tuneability. Almost four hundred polariton lasing observations recorded while scanning four microcavities. The single 400 nm pulse of ~1.2

P$_{th}$ has been used to pump the structures. The measurement results are depicted in **Figure 3.9** as a scatter plot of the polariton lasing wavelengths versus exciton-photon detunings. Polariton lasing emission from BODIPY-G1 organic-filled microcavity spanned a wide range in the green-yellow part of the visible spectrum from 537 nm to 570 nm. Emission from the microcavity with the most extensive detuning range of [-0.25; -0.16] eV covered the broad wavelength range from 547 nm up to 570 nm. The bare cavity mode (empty black circles) derived from the measured linear dispersion for each observation of polariton lasing in a way described in section 3.2.2. The black polygon on the chromaticity diagram
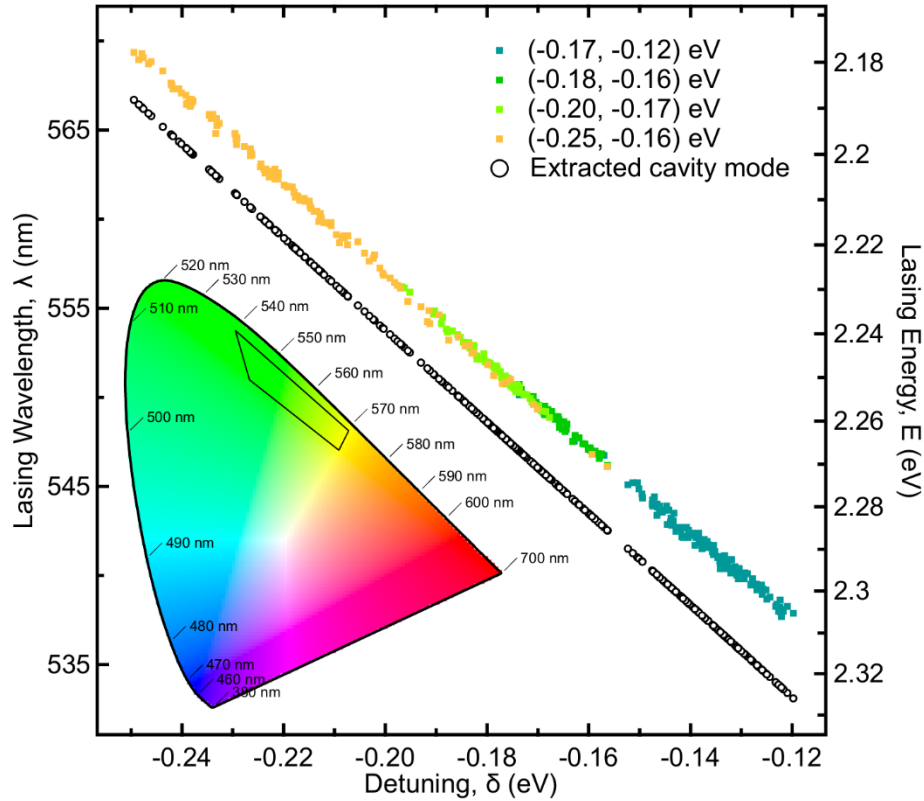
Figure 3.9. The wavelength (left axis) and photon energy (right axis) of observed polariton lasing versus corresponding exciton–photon detuning (colorized solid-squares). The top right inset shows the detuning ranges for each microcavity sample. The black open circles indicate the bare cavity mode corresponding to each lasing realization. Polariton lasing spans the green-yellow part of the visible spectrum, as shown with a solid black polygon on the CIE 1931 chromaticity diagram (bottom left inset).

corresponds to the color range [67], which one can obtain by using the characterized microcavities.

For each realization of polariton lasing presented here, we observed the same behaviour as have been shown in Figure 3.7: the LPB mode was lower than the corresponding cavity mode, and polariton lasing appeared blue-shifted to the bottom of LPB. Polariton dispersions for several detunings are plotted in **Figure 3.10**. It is worth to note that lasing emerged only from the LPB (dashed red line), i.e., polariton lasing.
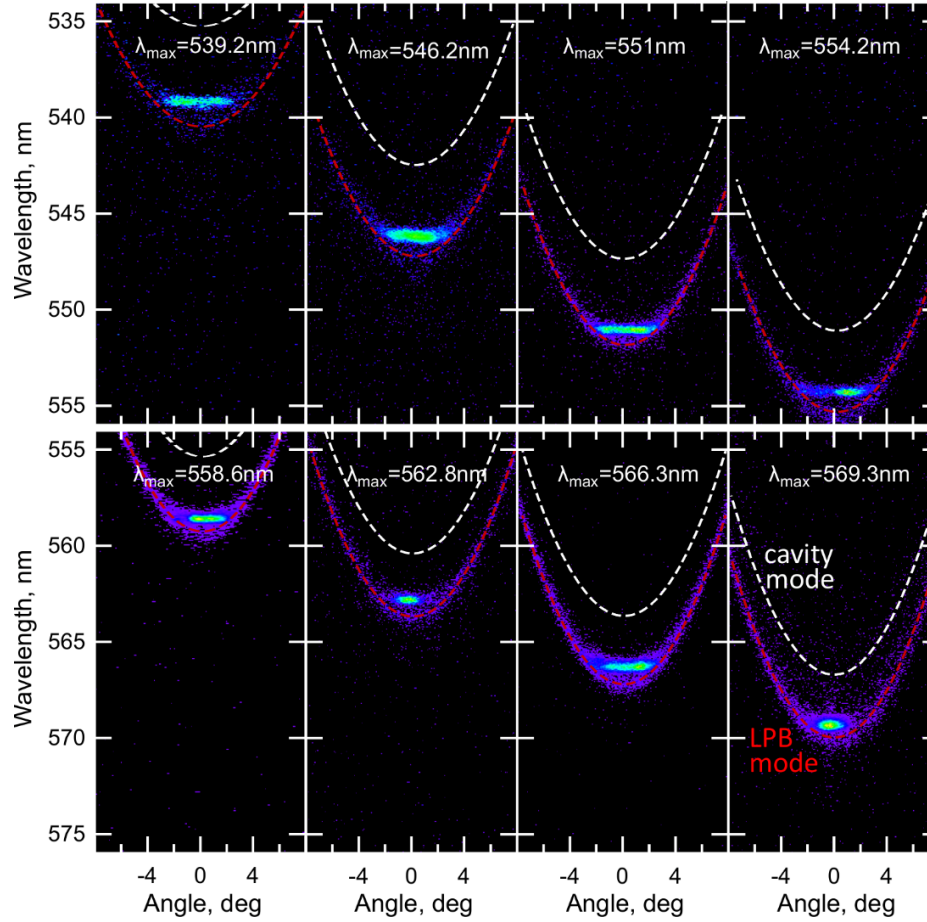
Figure 3.10. Polariton dispersion images recorded for several detuning values. Luminescence from the LPB (dashed red curve) identifies the linear regime, while the blue-shifted emission of high-intensity around normal incidence (green area) is indicative for the polariton lasing. The dashed white lines correspond to the bare cavity modes.

For a subset of presented wavelengths, we performed the full excitation density dependence, which allowed us to estimate the dependence of the polariton lasing threshold on the exciton–photon detuning δ. We observed a nearly constant condensation threshold across the entire detuning range with an average threshold value of ≈ 6.5 mJ cm^{-2} with a standard deviation of 1.5 mJ cm^{-2}.
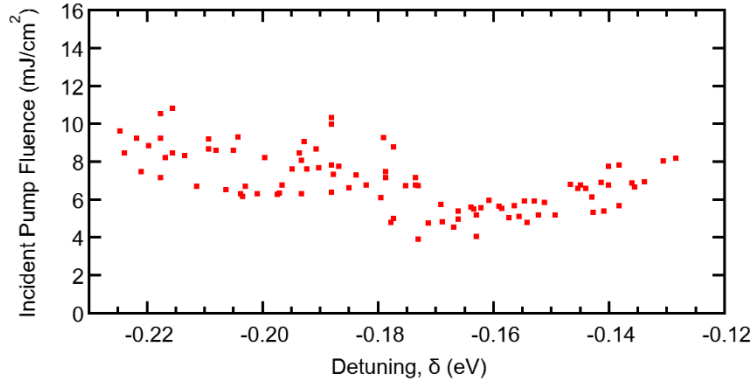
Figure 3.11. Polariton lasing threshold dependence versus the exciton-photon detuning. Nearly constant condensation threshold $\approx (6.5 \pm 1.5)$ mJ cm^{-2} observed across the entire detuning range.

3.4.4 Organic polariton lasing efficiency

One of the essential characteristics, which should also be estimated, is the polariton lasing efficiency [68] of fabricated structures. It defines how much of the input energy can be efficiently converted into the output lasing energy. For estimation, we pumped the microcavity with the pump beam of Gaussian profile with diameter d = 18 µm at one over the e^2 level. The real space image of the linear polariton emission from the microcavity below the condensation threshold is shown in **Figure 3.12(a)**. Once we pumped the structure with a single pulse of 320 pJ of absorbed energy (~1.6 P$_{th}$), the lasing is observed from a small area with a diameter $d_{lasing} \approx 6$ µm as shown in Figure 3.12(b).
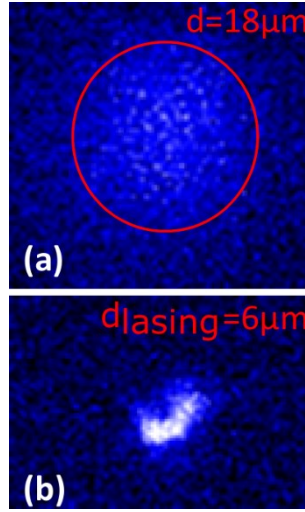
Figure 3.12. Real space images of the (a) linear polariton emission below and (b) polariton lasing above the condensation threshold. Red circle corresponds to the excitation pump spot of d =18 μm diameter at one over e^2 level. Above the threshold, polariton lasing appears from a small area with $d_{lasing} \approx 6$ μm.

By calibrating the CCD camera with the laser of the same wavelength as polariton emission, we were able to measure the energy of polariton lasing, leaving the microcavity, which found at ~5 nJ. Finally, the polariton lasing efficiency at 1.6 P_{th} was found:

$$Efficiency = \frac{E_{emitted}}{E_{absorbed}} = \frac{5 \ [pJ]}{320 \ [pJ]} * 100\% \approx 2\%$$

3.5 Conclusion

In the present chapter, we have demonstrated strong coupling and polariton lasing in the microcavities containing BODIPY-G1 fluorescent molecular dyes dispersed in the polystyrene matrix. By engineering a thickness gradient across the microcavities, we have accessed a broad range of exciton–photon detuning conditions. Using these structures, we have shown that BODIPY-G1 can undergo polariton lasing over a broad range of

58

wavelengths ($\approx$ 33 nm) across the green-yellow part of the visible spectrum, with a highly monochromatic emission line of 0.1 nm. We note here, that there are a number of related materials in the BODIPY dyes family [69], emission of which is spanning from the visible to the near-infrared wavelengths. Such materials are also expected to be good candidates for the tuneable polariton lasing realization. These results have a considerable potential to pave the way toward coherent lighting applications using strongly-coupled organic microcavities where the tuneability is needed.

The wavelength tuning on fabricated-like microstructures can be qualitatively performed in the broad ranges. However, a limitation for the tuning precision can occur. It originates from the blueshift of the polariton lasing emission wavelength. In all lasing realizations performed in chapter 3 (and, notably, as depicted in Figure 3.10), the emission wavelength is shifted from LPB bottom to 1-2 nm. Also, according to the power dependence in Figure 3.8(b), such an energy shift can growth further at increasing excitation densities. These crucial facts are affecting the precision of the wavelength tuning and making it complicated and even unpredictable. That is why the understanding of the blueshift origin is crucially needed to manage a precise control over lasing emission in polaritonic devices. The next Chapter 4 is dedicated to the described problem and contains an explanation for the origin of the blueshift which is ubiquitously observed in the organic polariton condensates.

Chapter 4. On the origin of blueshifts in organic polariton condensates

4.1 Introduction

From the very first observation of strong coupling in organic microcavities [11], organic polaritonics rapidly developed with the culmination in room-temperature polariton condensates observation and related phenomena. Organic polariton lasing, which has emission wavelengths spanning a broad range of the visible spectrum, was demonstrated on various molecular materials, and the polariton lasing wavelength tuneability has been recently investigated [17]. Furthermore, polariton condensation in organic microcavities gave rise to advanced polaritonic devices; for example, recently demonstrated polariton transistor operating at ambient conditions [70]. Due to the coherent nature of polariton condensates, the observation of superfluidity phenomenon [71] is possible with the further implementations into polariton circuits. However, despite the significant breakthrough performed in the field of organic polaritonics and the great potential for applications in devices, the mechanisms underlying polariton nonlinearities, such as a blueshift, remain poorly explored.

In inorganic semiconductor microcavities, Wannier-Mott nature of the excitons permits interparticle Coulomb exchange interactions [72]. Thus, the blueshift of polariton mode is considered to be the primary manifestation of polariton interactions in inorganic microcavities [19,20]. However, in organic semiconductors, electronic excitations are described as Frenkel excitons in which electron-hole pairs are strongly-coupled (0.5 – 1 eV) and localized on a single molecule. Therefore, such localizations of Frenkel excitons vastly reduce the Coulomb exchange interactions and interparticle scattering in organic

systems [73,74]. That is why the origin of the step-like blueshift, ubiquitously observed at condensation threshold and present across a broad range of organic materials [10,13,14,16–18,70], remains unexplored.

In the present chapter, we reveal the origin of polariton condensate blueshifts in organic microcavities. We are considering several processes which can contribute to the blueshift, and examine them experimentally. Namely, we examine the relative contribution of a number of processes, including intracavity optical Kerr-effect, gain induced frequency-pulling, polariton-exciton and polariton-polariton scattering, as well as the quenching of the Rabi splitting and renormalization of the cavity mode energy both induced by the saturation of molecular optical transitions due to states filling at higher excitation densities (Pauli blocking). Through performed analysis, we conclude that the blueshifts in organic polariton condensates arise from the interplay of the saturation of molecular optical transitions and intermolecular energy migration. For the first time, we consider the role of weakly-coupled molecules and show a significant contribution of cavity mode renormalization on the observed polariton blueshift in organic microcavities. Through a quantitative analysis, we found out that the step-like energy increase, observed at the threshold, results from an interplay between stimulated relaxation to the polariton ground-state and intermolecular energy transfer. The latter process results in a depolarization of the emission with respect to the polarization of the excitation beam. Our interpretation is qualitatively and quantitatively corroborated by a concomitant step-like increase of the degree of linear polarization of the emission at condensation threshold [10,13,14,18].

4.2 Samples optical characterization

In this study, we utilized the same samples from Chapter 3. To make an investigation on the energy shift more convenient, in this chapter, we represented all the measurements in terms of energy. First of all, we considered the spectral characteristics of the material used in the microcavities. The normalized absorption (Abs) and photoluminescence (PL) spectra of the bare BODIPY-G1 in PS film of 172 nm thickness were measured, as discussed in Section 3.2.1. The results are shown in **Figure 4.1**. The absorption maximum of the film occurred at ~ 2.446 eV, with the photoluminescence being Stokes-shifted to 2.336 eV.
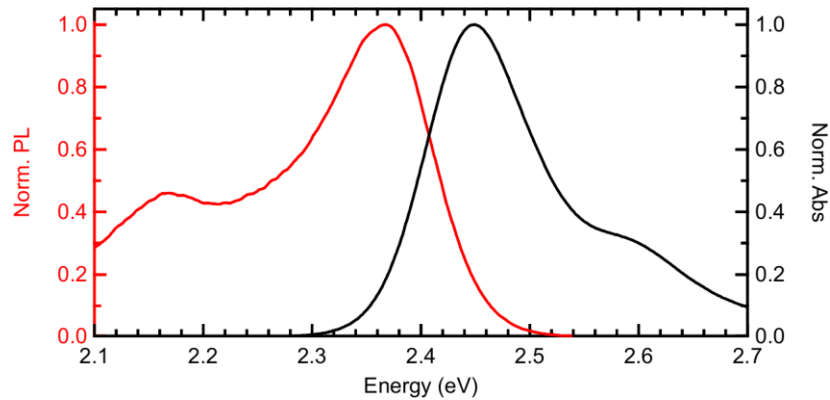
Figure 4.1. Normalized absorption (black) and photoluminescence (red) spectra of the bare BODIPY-G1 film of 172 nm thickness.

ASE measurement of the same film was performed in a way described in Section 3.2.1. Results, shown in **Figure 4.2**, revealed that BODIPY-G1 undergoes optical gain. The maximum of the optical gain spectrum occurred at ~ 2.272 eV, as indicated by the rapid intensity increase and narrowing of the fluorescence emission spectrum. An excitation threshold needed for the amplification of spontaneous emission was found at 5.1 mJ cm^{-2} of incident excitation density.
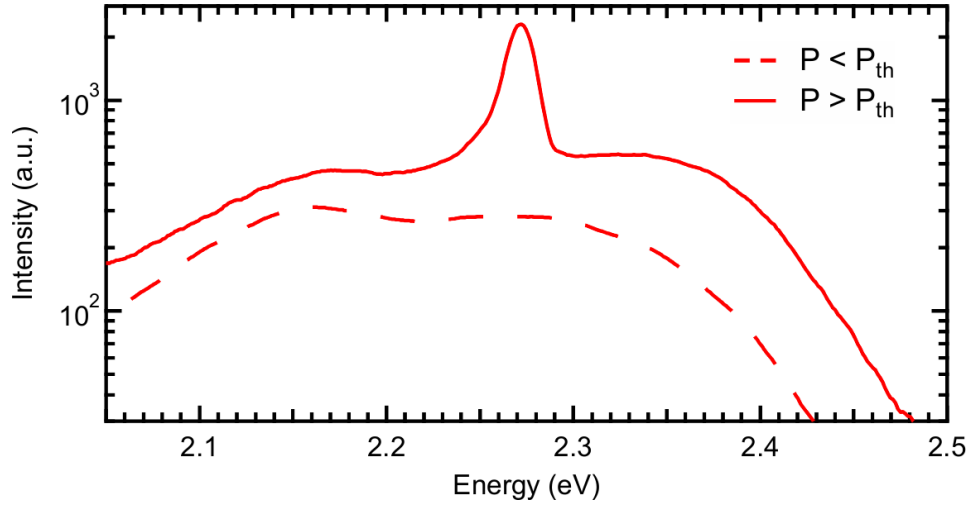
Figure 4.2. Amplified spontaneous emission of the neat 172 nm thin film below $P < P_{th}$ (dashed curve) and above $P > P_{th}$ (solid curve) amplification threshold of 5.1 mJ cm^{-2}.

We measured an angle-resolved reflectivity (method described in Section 3.2.2) of microcavity at the point where LPB energy at $k_{II} = 0$ appeared at ~ 2.24 eV (~553 nm). It is worth noting that in further investigations, we tried to keep the same LPB energy position to follow initial conditions. The typical reflectivity spectra recorded at 24, 30, and 36° are depicted in **Figure 4.3(a)** and proving the strong coupling. Upper and lower polariton branches became visible as the local minima in broad DBR reflectivity stop-band, and they split around the BODIPY-G1 absorption peak at 2.446 eV (507 nm). We created a dispersion plot which is displayed with red squares in Figure 4.3(b) by plotting the UPB and LPB energies (defined from the reflectivity) as a function of angle. We superimposed resulting points with a polariton dispersion obtained under non-resonant excitation at 400 nm in the linear excitation regime (color plot). With the use of the coupled harmonic oscillator model (as described in section 2.1.3) we fitted upper and lower polariton branches in Figure 4.3(b) (dashed lines) and obtained a vacuum Rabi splitting of

63

$\hbar\Omega_0 \sim 116\ meV$ (which is in agreement with results in Table 1) and an exciton-photon detuning of $(-160)\ meV$.
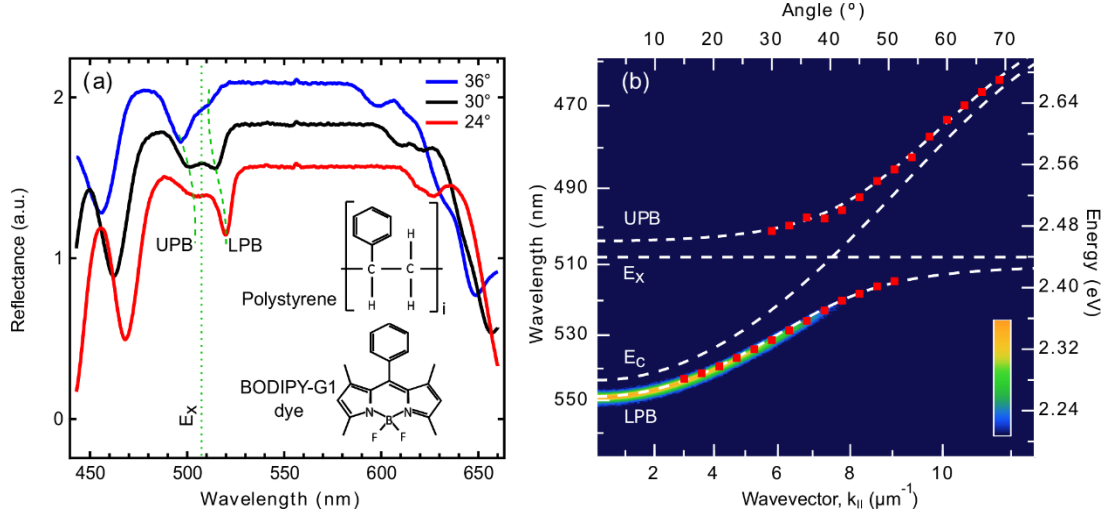
Figure 4.3. Strong light-matter interaction in dye-filled microcavities. (a) Angle-dependent reflectivity spectra of the microcavity recorded at different angles exhibit clear anti-crossing at the exciton resonance energy E_x (green dotted line) and indicate the formation of lower (LPB, dashed line) and upper (UPB, dashed line) exciton-polaritons branches. Polariton dispersion relation in (b) is plotted by combing the data of photoluminescence imaging acquired in a Fourier space (rainbow colour density plot in a log scale) with the polariton states extracted from angle-dependent reflectivity measurements (red squares). Fits for the LPB and UPB, together with the cavity mode E_c and energy of exciton resonance E_x are shown as a white dashed curves.

4.3 Experimental results on the blueshift measurements

We recorded the dispersion of polariton photoluminescence emission as a function of excitation density by pumping the microcavity in a transmission configuration (see description in Section 3.3) with single excitation pulses of 2 ps at 400 nm having a horizontal polarization. Distribution of the time-integrated polariton emission with $E_{k_{II}=0}$ at ~ 553 nm below the condensation threshold is shown in **Figure 4.4(a)**. Above the threshold, polariton emission collapsed to the bottom of the LPB as shown in Figure 4.4(b), and the polariton lasing happens not from the very bottom of LPB (dashed red curve), but

64
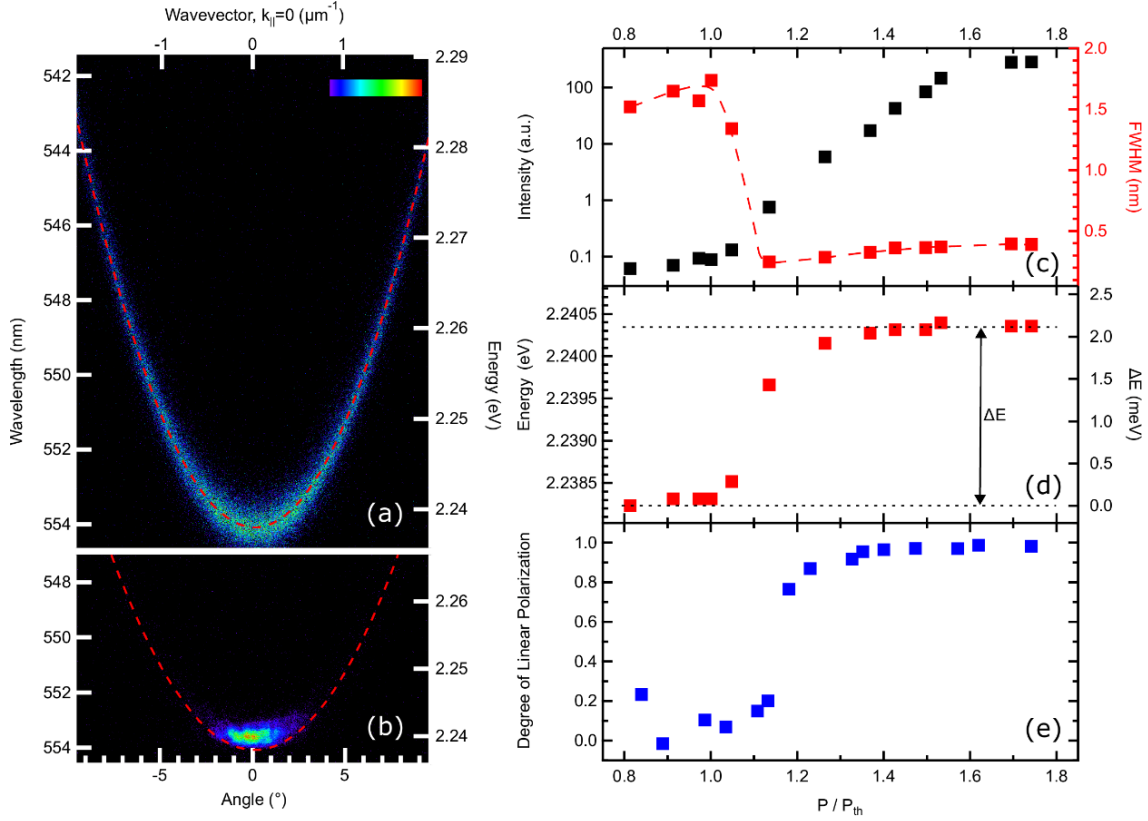
Figure 4.4. Normalized E,k polariton population (photoluminescence) images recorded (a) at 0.8 P_{th} and (b) at 1.4 P_{th}. Dashed red curves show lower polariton branch dispersion in the linear regime. (c) Photoluminescence intensity integrated into the range over ± 0.2 μm^{-1} at $k_{II} \sim 0$ (black squares) and full width at half maximum (red squares) versus pump power. The red dashed curve is a guide for the eye. (d) The energy of the ground polariton state versus pump-power. (e) Degree of linear polarization (blue squares) as a function of pump power.

it is shifted by ~ 2 meV to the blue, i.e., polariton condensate blueshift is observed. Figure 4.4(c) plots the photoluminescence intensity (left) and the FWHM of the emission linewidth (right axis) integrated over $\pm 1°$ (± 0.2 μm^{-1}) around normal incidence versus excitation density. Corresponding energy shift and the degree of linear polarization of the emission spectrum are depicted in Figures 4.4(d) and (e), respectively. At an excitation density of 120 μJ cm^{-2} of absorbed pump fluence (P_{th}), we observed a dramatic increase of

the photoluminescence intensity accompanied by linewidth narrowing from 1.6 nm to 0.25 nm and a step-like growth of the degree of linear polarization and a step-like blueshift of the emission spectrum.

Having performed an excitation density dependence in control point, we used the tuneability feature of our structures to explore polariton condensation energy-shift over a broad range of exciton-photon detuning. As the organic microcavity is a high-disordered system [75–77], we collected the statistics of the energy shifts measured in $\sim$ 400 single-shot realizations. The scatter plot of polariton condensation energy shift dependence on the energy of lower polariton ground state at $k_{\mathrm{II}} = 0$ is shown in **Figure 4.5**. For all experimental realizations, we observed only the blueshift of the condensate. For each measurement, the blueshift was defined by comparing the energy of the emission below and above the threshold. We avoided averaging over the intensity fluctuations of the laser by utilizing a single-shot dispersion imaging technique described in Section 3.3.
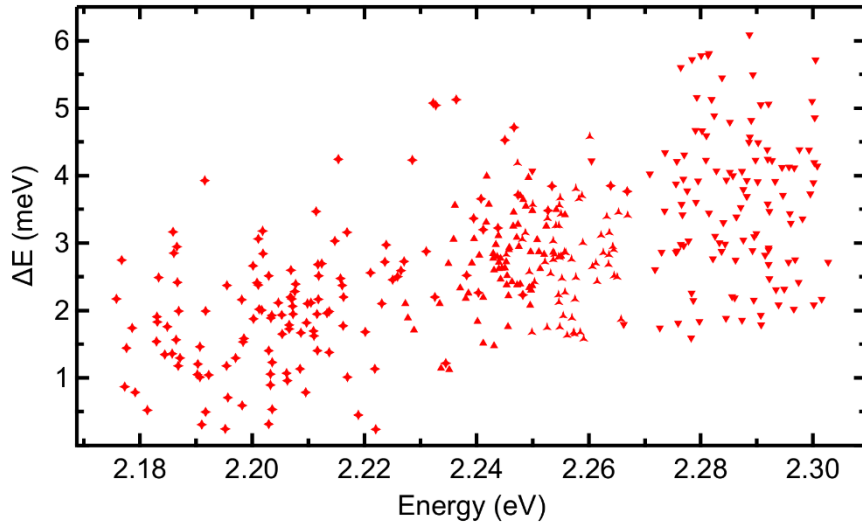
Figure 4.5. Scattering plot of single-shot blueshift realizations across the whole accessible detuning range.

4.4 Analyses on the origin of the blueshift

To explore the mechanism behind the blueshift observed in Figure 4.4(d), we examined the contribution of several processes, which can contribute to the blueshift. In this section, the discussion and analysis of the study outcomes will be provided.

4.4.1 Gain induced frequency pulling

We considered the gain induced frequency-pulling, which could be the reason for the blueshift at condensation threshold. Since fabricated microcavities were negatively detuned - in other words, the polariton mode has a sizeable photonic fraction, the gain pulling mechanisms is particularly important [3]. We explored the extent to which gain induced frequency-pulling affects the condensate's blueshift by analyzing the ASE spectrum (Figure 4.2) with the blueshift scatter plot from Figure 4.5. To make the scatter plot dependence trend more pronounced, we performed the binning with the Sturges' formula [78] which defines an optimal number of binning points for the data scattering reduction. According to the rule, the number of bins is $k = 1 + log_2(n)$, where n is the total amount of observations. Taking n = 378 into account, we got k = 9.56, i.e., nine bins of 14.1 meV width for the measured LPB energy range. In **Figure 4.6**, we superimposed the binned data points for blueshift (black squares) with the amplified spontaneous emission spectrum (red curve). If the gain-induced frequency pulling is a strong effect, then as the LPB frequency is swept across the peak of the ASE gain curve (2.272 eV), the emission frequency should get pulled towards this peak. As a result, the sign of the frequency shift should be different for LPB frequencies on either side of the gain peak: positive for LPB frequencies below the gain peak and negative for frequencies

67

above [79,80]. However, at the condensation threshold, the observed shifts are always positive, i.e., blue-shifted. Thus we conclude that gain-induced frequency pulling is not a dominant effect on the blueshift.
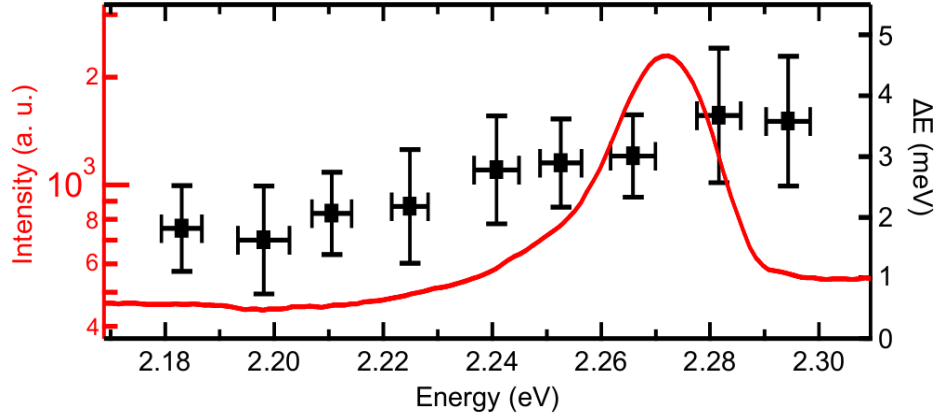
Figure 4.6. The ASE spectrum (red, left axes) and the blueshift, ΔE. Blueshift was extracted from the binning of scattering plot with Sturge rule (black squares with standard deviation, right axes).

4.4.2 Intracavity optical Kerr-effect[1*]

Another potential reason for the condensate blueshift is the nonlinear refractive index change of the intracavity polymer matrix by means of the conventional Kerr-effect [81,82], which could be induced at the threshold by a step-wise increase of the intensity of the polariton lasing electric field inside the cavity[2*]. To examine the contribution of the E-field induced difference in the refractive index, we measured optical nonlinearities of the polystyrene film using both a closed- and open-aperture Z-scan technique [83].

[1*] The results, presented in this section, were measured and extracted by Anton Baranikov; there is no conflict of interests of authors.

[2*] It is worth to note that we tried to perform the measurements on the BODIPY-G1 in PS film, but realized that film was photodegrading and optically damaged at relatively low energies.

For this study, we used a thin polystyrene film with a thickness of 600 nm. We carried out the measurements using the high-energy Ti:Sapphire regenerative amplifier system (Coherent Libra-HE), which pumped the optical parametric amplifier (Coherent OPerA SOLO) and provided 550 nm central emission wavelength which approximately coincided with the polariton condensate emission wavelength obtained in Figure 4.4. The pulse duration was 140 fs, and the repetition rate was 10 Hz. The pump beam was incident on the lens with a 100 mm focal length and focused into the spot of 16 μm radius. Data acquired with Si photodetectors (Thorlabs-Det10/M), which were connected to the oscilloscope (Keysight DSOX3054T). **Figure 4.7** schematically shows the experimental setup. Here, PD2 and PD3 are photodetectors recording open- and closed-aperture signals, respectively, PD1 is a reference photodetector. We fixed the sample on the motorized translation stage (Thorlabs TravelMax 50 mm driven by Thorlabs Trapezoidal Stepper Motor Drive).
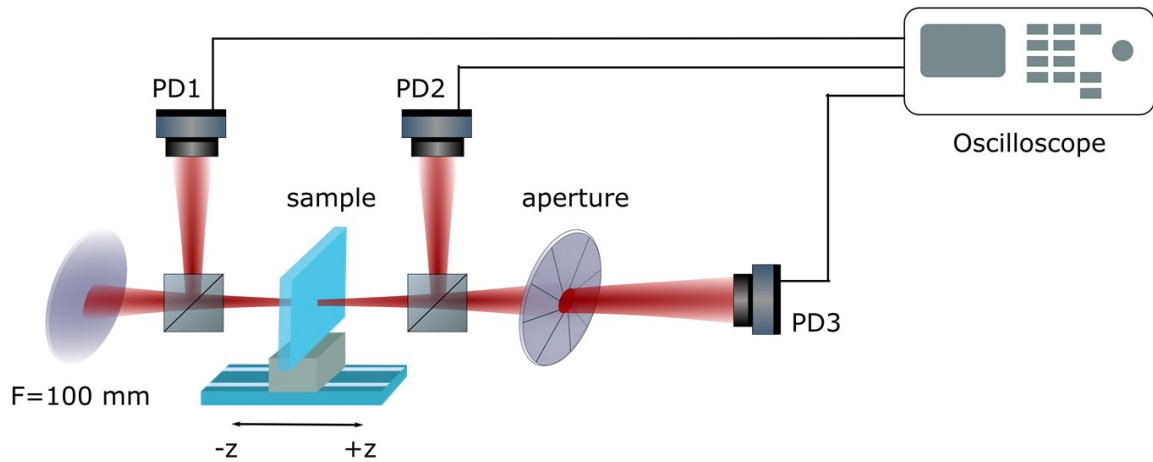
Figure 4.7. Sketch of an open- and closed-aperture Z-scan setup. PD 1-3 are the Si photodetectors. Sample moving along the z-axis is placed on the motorized translation stage.

The open- and closed-aperture Z-scan transmission measured at 9.5 nJ (black circles) and 438 nJ (red rhombs) pulse energies are shown in **Figure 4.8**. From these measurements, we found out that the nonlinearities took place when the 438 nJ excitation pulse induced an electric field inside the microcavity of 779 GW/cm^2 intensity at the foci.
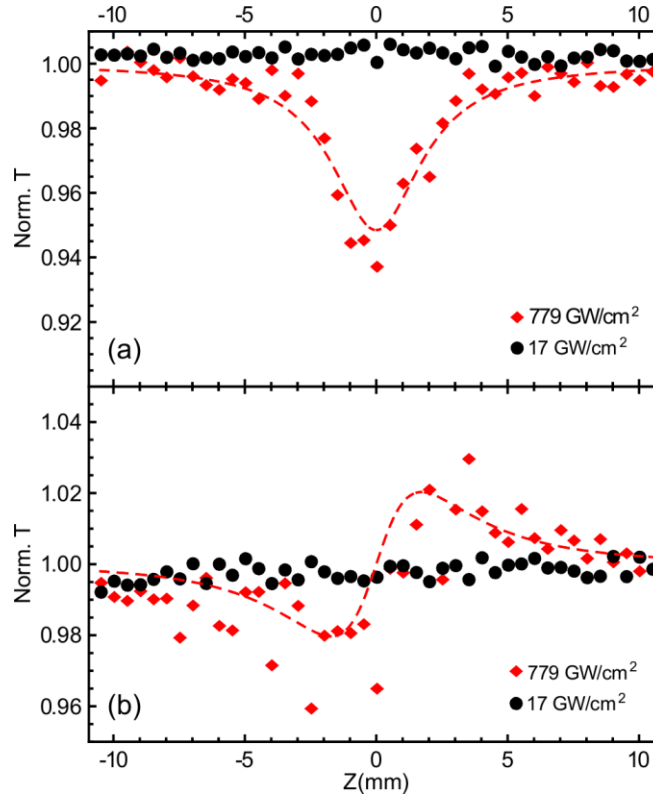
Figure 4.8. (a) Open- and (b) closed-aperture Z-scan data of the polystyrene film measured at two different pump energies: 9.5 nJ (black circles) and 438 nJ (red rhombs).

To understand if we reached such nonlinearities in measured microcavities, we performed the estimation of intracavity intensity. Initially, we calibrated the CCD camera with a 550 nm and 140 fs laser single pulse of known energy. By applying this calibration, we measured the energy, $W_c = 0.5$ pJ, of outgoing from the MC emission pulse at the pump of ~ 1.4 P_{th} condensation threshold. Therefore, outgoing emission intensity:

$$I_0 = \frac{2 \cdot W_c}{\tau \cdot \pi \cdot r^2} \cong 0.5 \cdot 10^7 \; W/cm^2$$

where $r = 8$ μm is the condensate profile radius, $\tau = 100$ fs is the polariton lifetime.

For simplicity, we considered the microcavity with two identical DBRs of the same reflectance. The outgoing emission intensity, I_0, recorded from one side of the microcavity is coupled with the intensity I_c inside the cavity as:

$$I_c \cong 4 \, Q/\pi \cdot I_0 \tag{4.1}$$

By introducing the microcavity quality factor, $Q = 350$, into the last formula, the intracavity intensity could be defined: $I_c = 2.2 \; GW/cm^2$.

From the open-aperture Z-scan, shown in Figure 4.8(a), we observed a reverse saturable absorption at the high electric-field intensity of $779 \; GW/cm^2$; at $17 \; GW/cm^2$ this nonlinearity was not observed. Therefore, we conclude that a reverse saturable absorption did not take place in our microcavities, in which the electric-field intensity at the condensation threshold was $\sim 2 \; GW/cm^2$.

From the closed-aperture Z-scan, presented in Figure 4.8(b), we observed that nonlinear effects did not occur at $17 \; GW/cm^2$. At the high electric-field intensity of $779 \; GW/cm^2$ inside the cavity, we found that the polystyrene falls for a weak self-focusing effect. It is worth noting, that even if such high electromagnetic fields could be generated within a microcavity, the extracted positive value of the nonlinear refractive index (n_2) $\sim$ $1.89 \cdot 10^{-14}$ cm^2/W would induce a red-shift (methods for extraction are described in [84,85]). Finally, we concluded that an optically induced change of the intracavity nonlinear refractive index is not responsible for the blueshift at the condensation threshold.

4.4.3 Polariton-exciton and polariton-polariton scatterings

The next process we investigated was the contribution of polariton-polariton and polariton-exciton scatterings into the blueshift at condensation threshold. Blueshifts, (ΔE), experimentally observed in semiconductor microcavities with Wannier-Mott excitons, are attributed to the combination of polariton-polariton ($g_{p-p}\,N_p$) and polariton-exciton ($g_{p-x}\,N_x$) interaction terms. In inorganic systems, this is usually expressed by the following equation [20,23]:

$$\Delta E = g_{p-p} \cdot N_p + g_{p-x} \cdot N_x \tag{4.2}$$

where, N_p - polariton and N_X - exciton reservoir densities, g_{p-p} is the polariton-polariton scattering interaction constant, which is related to the exciton-exciton scattering constant, g_{x-x}, via:

$$g_{p-p} = g_{p-x} \cdot |X|^2 = g_{x-x} \cdot |X|^4 \tag{4.3}$$

where X is the exciton fraction amplitude of the polariton state. Since the polaritons occupancy at the condensation threshold is not dependent on the exciton fraction, the experimental dependence of the blueshift scattering plot (Figure 4.5) represented from the exciton fraction, $|X|^2$, should reveal whether polariton-polariton or polariton-exciton interactions induce the blueshift.

To represent the measured blueshift scattering plot from the exciton fraction, we needed to describe the dependence of the experimentally-measured emission frequency of the polariton-state on its exciton fraction. The latter depends on the exciton-photon detuning, δ, and vacuum Rabi splitting, $\hbar\Omega_0$, through:

$$\left| X_{k_{\mathrm{II}}=0} \right|^2 = \frac{1}{2}\left(1 + \frac{\delta}{\sqrt{\delta^2 + (\hbar\Omega_0)^2}} \right) \tag{4.4}$$

By fitting (described in Section 3.2.2) the polariton dispersions obtained from white light reflectivity measurements in a linear regime without any excitation density-dependent energy shifts of the LPB, we defined all the parameters of the strongly-coupled system. In **Figure 4.9(b, c)**, we plotted the fitting results of the vacuum Rabi splitting and exciton-photon detuning versus the energy of the lower polariton state. The vacuum Rabi splitting
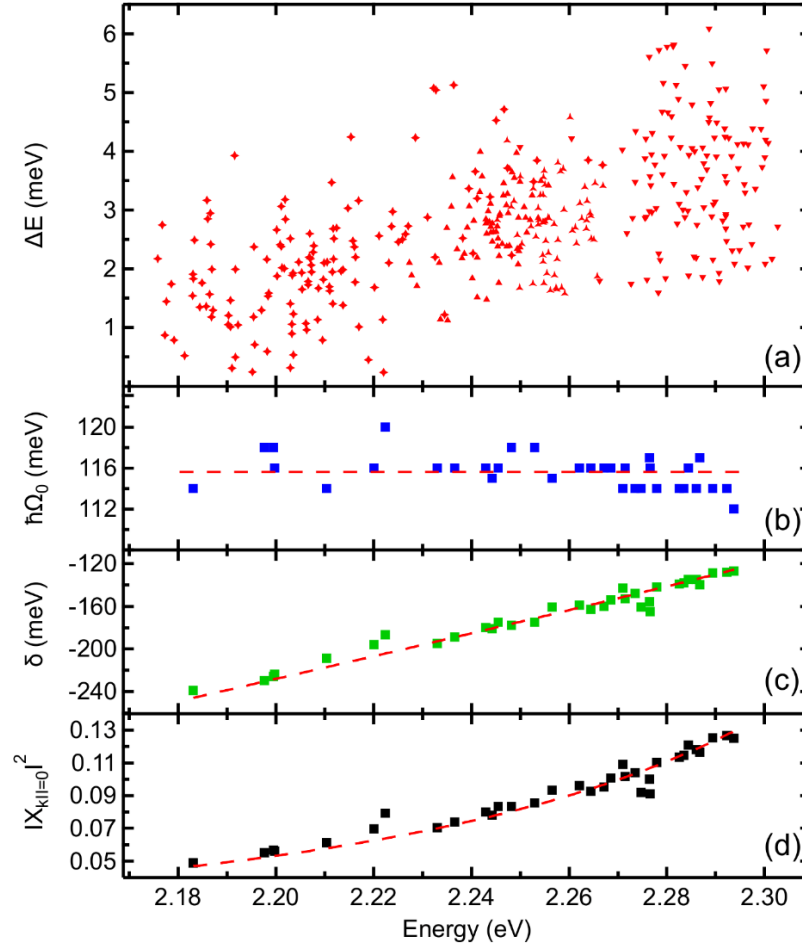
Figure 4.9. (a) Single-shot blueshift realizations measured for all samples. (b) Vacuum Rabi splitting, $\hbar\Omega_0$, and (c) detuning, δ, extracted from the angle-dependent reflectivity measurements. The Rabi splitting was almost invariant, with an average value of 116 meV ± 2 meV (dashed red curve). (d) An exciton fraction $|X_{K_{II}=0}|^2$ of the polariton wave function at $K_{II} = 0$, calculated from $\hbar\Omega_0$ and δ. Red dashed curves in (c) and (d) correspond to analytical fit functions for δ and $|X_{K_{II}=0}|^2$, respectively.

was almost invariant across the whole energy range, with the average value of (116 ± 2) meV. The exciton-photon detuning gradually changed in the range of $[-240, -120]$ meV. From the Rabi splitting and detuning dependences, we were able to find the exciton fraction $|X_{k_{II}=0}|^2$ utilizing Eq. 4.4 and plot its dependence on the lower polariton state energy, which is shown in Figure 4.9(d).

By the use of performed analyses, we have finally obtained the measured blueshift dependence on the exciton fraction $|X_{k_{II}=0}|^2$, which is shown in **Figure 4.10**. It indicates that the energy-shift, ΔE, of the polaritons has a sub-linear dependence on $|X_{k_{II}=0}|^2$; a result that firmly precludes pair-polariton scattering as the underlying mechanism for the observed blueshift and suggests that polariton-exciton scattering is also unlikely. Here the former process would result in a quadratic dependence on $|X_{k_{II}=0}|^2$, and the latter on a linear dependence (see Equation 4.2 and 4.3).
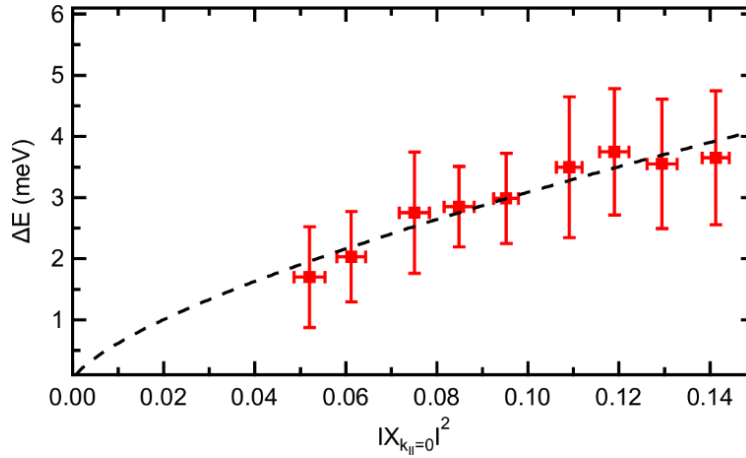
Figure 4.10. The blueshift, ΔE, versus exciton fraction. The dependence of the blueshift on the exciton fraction is calculated by binning the scattering plot (section 4.3.1) and taking into account the dependence of exciton fraction on the ground polariton state energy (Figure 4.9(d)). The dashed black line is the best-fit result by power-law $\Delta E \sim \left(|X_{k_{II}=0}|^2 \right)^{\beta}$ with variable parameter $\beta = 0.7$.

Additionally, in the absence of pair-polariton interactions and for a constant exciton fraction/detuning, we expect that polariton-exciton interactions should lead to a linear blueshift with increasing excitation and thus exciton density (as expressed by Equation (4.2)). At the condensation threshold, stimulated relaxation from the exciton reservoir to the polariton ground-state would lead to clamping of the exciton density and, therefore, of the energy shift. However, to date, all non-crystalline semiconductor microcavities undergo a nearly step-like increase of polariton blueshift at the condensation threshold [10,13,14,16,17,70] as shown in Figure 4.4(d). Thus, the step-like dependence precludes the polariton-exciton interactions to be the driving mechanism for the observed blueshifts; a conclusion that is also corroborated by the sub-linear dependence of the energy shift on $\left|X_{k_{\mathrm{II}}=0}\right|^2$. Such finding is also consistent with the high degree of localization of Frenkel excitons on a single molecule, as such exciton localization is expected to weaken Coulomb exchange interactions and suppress interparticle scattering dramatically.

4.4.4 Quenching of Rabi splitting and nonlinear change in the cavity refractive index n_{eff}

Having established that previously considered processes do not induce the blueshift, we suggest the last mechanism, which describes the observed blueshifts.

To describe the observed blueshifts, we propose a new mechanism that based on quenching of the Rabi splitting and nonlinear change in the cavity refractive index n_{eff}. Both are the consequences of the same initial nonlinear process, namely saturation of the molecular optical transition. Owing to the Pauli-blocking principle, excited (i.e., occupied) states cannot be filled twice that effectively reduce oscillator strength of the Frenkel

excitons. Therefore, occupied states do not contribute to the optical absorption at the exciton resonance and effectively reduce the Rabi splitting [14,86] through the relation:

$$\hbar\Omega(n_T) = \hbar\Omega_0\sqrt{1 - \frac{2n_T}{n_0}} \qquad (4.5)$$

(for a microscopic theory of Rabi-quenching see Appendix 2). Here, equation (4.5) describes the quenching of the vacuum Rabi splitting, $\hbar\Omega_0$, as a function of the total number of excitations, namely the sum of excitons and polaritons $n_x + n_p$, where n_0 is the total number of molecules contributing to the strong-coupling. Since the optical pump results in a saturation of the molecular optical transitions that contribute to strong coupling, we expect a partial quenching of the Rabi splitting; an effect that results in a measurable blueshift of the lower polariton mode with increasing excitation density. We note here that only a small fraction of molecules in the intracavity layer strongly-coupled to the cavity photon ($f_c = \frac{N_c}{N}$ is the fraction of coupled molecules), as has been described by Agranovich et al. [75]. Therefore, a renormalization of the light-matter interaction constant takes place in the strongly-coupled molecules exclusively while the rest molecules being weakly-coupled do not contribute to the blueshift through the Rabi quenching mechanism. However, non-resonant pumping leads to the uniform excitation of the molecules across the cavity length and populate both strongly- and weakly-coupled molecules equally. Then, the large reservoir of weakly-coupled molecules dispersed in the cavity can effectively contribute to the blueshift via renormalization of the cavity mode energy, since the quenching of oscillator strength for the transition decreases the effective refractive index of the cavity n_{eff}.

The change in the refraction under quenching of the oscillator strength inherently related by causality principle, a Kramers-Kronig relation, that couple real and imaginary parts of complex dielectric function [87]. The relation predicts a decrease in the refractive index above the induced absorption resonance and an increase below resonance resulting in anomalous dispersion that usually appears within a width of the optical transitions. Here we address the problem of refractive index change by general Kramers–Kronig analysis:

$$n(\omega) = \frac{1}{\pi} P.V. \int_{-\infty}^{+\infty} \frac{k(\omega')}{\omega - \omega'} d\omega' \tag{4.6}$$

where $P.V.$ means integration over Cauchy principal value.

In order to calculate the real part of the complex refractive index using Eq. (4.6), one needs to know an imaginary part $k(\omega')$, which is related to the absorption spectrum. We use the absorption spectrum of the bare film to extract $k(\omega)$; for details, please see Appendix 3. As the absorption spectrum can be perfectly decomposed by a couple of Gaussian distributions centred at 2.446 eV and 2.548 eV for the excitonic energy and its vibronic replica respectively, it is quite convenient calculating Eq. (4.6) through the known Hilbert transform of Gaussians in the form of the weighted sum over Dawson functions:

$$n(\omega) = -\frac{2}{\sqrt{\pi}} \sum_i A_i \cdot F[\frac{(\omega - \omega_{o,i})}{\sigma_i \sqrt{2}}] \tag{4.7}$$

where the imaginary part is taken in the form of the sum over the Gaussian distributions

$k(\omega) = \sum_i A_i e^{\frac{-(\omega - \omega_{o,i})^2}{2\sigma_i^2}}$ accordingly, and $F\left[\frac{(\omega - \omega_{o,i})}{\sigma_i \sqrt{2}}\right]$ is the Dawson function (integral)

with the argument $\frac{(\omega - \omega_{o,i})}{\sigma_i \sqrt{2}}$.

Equation (4.7) describes anomalous dispersion naturally appeared on top of the average effective cavity refractive index $n_{eff} = 1.81$ (see Table 1 in Section 3.2.2) as the consequence of molecular optical transitions. Therefore, with decreasing the imaginary part, one can observe a reduction in the real part of the refractive index overall the lower energy sideband. **Figure 4.11** shows the imaginary and real parts of the complex refractive index as the function of energy. Note that Δn is positive on the high-energy side of the exciton resonance and is negative on the low-energy side.
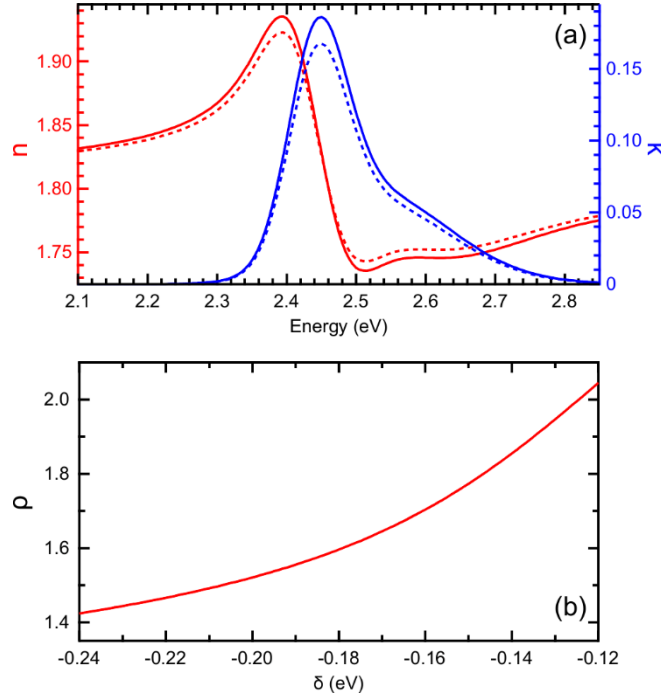
Figure 4.11. (a) Real (red) and imaginary (blue) parts of complex refractive index plotted for the case of unperturbed (solid) and saturated (dashed) molecular transition, respectively. Here we saturate the transition for the 10 percent. (b) The ratio $\rho = \frac{\Delta E^C_{LPB}}{\Delta E^\Omega_{LPB}}$ shows relative contributions of renormalization in the cavity mode energy and the Rabi-quenching term to overall polariton blueshift as a function of exciton-photon detuning.

The change in refractive index is evident over a range of energies on either side of the resonance that induces a correspondent energy shift of the cavity mode E_c by a value

of ΔE_c. For the small changes, $\Delta n \ll n_{eff}$, one can use the following approximate expression for the energy shift:

$$\Delta E_c \cong -E_c \frac{\Delta n}{n_{eff}} \tag{4.8}$$

where $n_{eff} = 1.81$ is the effective cavity refractive index.

Equation (4.8) describes the blueshift of lower polariton eigenstates following by change in the refractive index of the cavity due to the saturation of the molecular optical transition of weakly coupled molecules. The net effect of both: quenching of the vacuum Rabi splitting and cavity mode renormalization effects on the blueshift ΔE_{LPB} can be described through

$$\Delta E_{LPB} = 1/2 \cdot \left\{ E_x + E_c \left(1 - \frac{\Delta n}{n_{eff}} \right) - \sqrt{\left(E_c \left(1 - \frac{\Delta n}{n_{eff}} \right) - E_x \right)^2 + (\hbar\Omega)^2} \right\} - E_{LPB}^0 \tag{4.9}$$

where E_x, E_c are the energies of the bare-exciton and cavity modes respectively, and E_{LPB}^0 is the unperturbed energy of ground polariton-state in the limit of small excitation numbers (linear-regime), $\hbar\Omega$ and Δn are the density-dependent vacuum Rabi splitting and the change of refractive index respectively.

In the case of small saturation parameter ξ, namely $\xi = \frac{(n_x + n_p)}{n_0} \cong \frac{n_x}{n_0} \ll 1$, we can significantly simplify the above equation for the polariton blueshift. First, we describe the change in refractive index Δn by means of parameter ξ as follows

$$\Delta n \cong -\frac{1}{5} \xi \cdot \alpha \cdot F[d] \tag{4.10}$$

For the sake of simplicity here, we replaced the weighted sum over Dawson functions from

Eq. (4.7) to a single Dawson function with argument $d = \frac{|\delta| \cdot 2\sqrt{ln2}}{FWHM}$, where $\delta = E_c - E_x$ is

detuning parameter and $FWHM$ is the full width of half maximum of the main absorption

peak attributed with $S_{0,0} \rightarrow S_{1,0}$ singlet optical transition. Scaling parameter α in Eq. (4.10)

corresponds to oscillator strength of the optical transition as it is proportional to absorption

maximum (Abs_{max}): $\alpha = \frac{Abs_{max} \cdot \lambda_{max}}{L}$, L is the cavity thickness. Thus we can now

reformulate Eq. (4.9) for the total polariton blueshift in a more convenient way within the

approximation of small saturation parameter ξ:

$$\Delta E_{LPB} = \Delta E_{LPB}^{\Omega} + \Delta E_{LPB}^{C} = \frac{\xi}{2}\left\{\frac{s \cdot \hbar\Omega_0}{\sqrt{1+s^2}} + \frac{E_x - |\delta|}{5n_{eff}} F[d] \cdot \alpha \cdot \left(1 + \frac{1}{\sqrt{1+s^2}}\right)\right\} \qquad (4.11)$$

where $s = \frac{\hbar\Omega_0}{|\delta|}$ is the dimensionless parameter of strong coupling. Here we exploit the

reasonable assumption of $f_c \ll 1$.

Both terms in Eq. (4.11) reflect the influence of the same physical process of

saturation of the optical transition on the polariton eigenstates energy; but they rely on

different subsets of molecules. The first term in curved parenthesis corresponds to the

quenching of vacuum Rabi splitting in strongly-coupled molecules. The second term

corresponds to the energy renormalization of the cavity mode under the change in the

refractive index of weakly-coupled molecules. Surprisingly, we found out that the

renormalization of the cavity mode dominates over the Rabi quenching in the total

polariton blueshift as $\rho = \frac{\Delta E_{LPB}^{C}}{\Delta E_{LPB}^{\Omega}} = \frac{(E_x - |\delta|) \cdot F[d] \cdot \alpha \cdot (\sqrt{1+s^2} + 1)}{5n_{eff} \cdot s \cdot \hbar\Omega_0} > 1$ for the whole range of

exciton-photon detuning accessed within the sample area. Clearly, the ratio is invariant

over the saturation parameter ξ; it depends only on the strong-coupling parameters $\hbar\Omega_0$ and δ, properties of the optical transitions involved, namely absorption parameter α, its linewidth *FWHM,* and cavity thickness *L*. Figure 4.11(b) shows the ρ ratio versus detuning. Despite the great significance of the cavity mode energy-shift, it has never been taken into consideration before this study. The previous study explains polariton blueshifts solely by means of Rabi quenching [88]. Our analysis based on Eq. (4.11) reveals the Rabi quenching is likely a secondary process driven the polariton condensate blueshift in [88] since ρ equals to 1.3, despite the very large vacuum Rabi splitting ~540 meV reported. In view, the Eq (4.11) mentioned above ultimately describes the magnitude of polariton energy shift in strongly-coupled organic microcavities. However, neither both factors separately nor their superposition explains the ubiquitous step-like increase of the blueshift at P_{th}, but instead predicts a continuous increase of the blueshift with an increasing number of excitations in the system, characterized by ξ parameter.

4.5 Modeling

To explain the step-wise behavior of blueshift dependence, we construct the following model. Since the BODIPY-G1 molecules randomly distributed in the film inside the cavity and the molecule by itself has a particular dipole moment orientation [89], we construct a model which distinguishes between molecules that have a non-zero projection of their optical dipole moment aligned parallel ($N_0^{\parallel}$) and perpendicular ($N_0^{\perp}$) to the linear polarization of the excitation laser. In **Figure 4.12** schematic for the classification is presented. We assume that upon non-resonant optical excitation, only the parallel-aligned
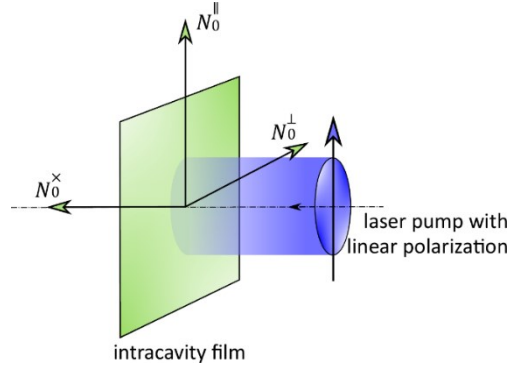
Figure 4.12. Schematical representation of the molecules' optical dipole moment alignment and laser polarization relation, considered in frames of the suggested model.

molecules are initially occupied. These molecules constitute an exciton reservoir ($N_x^{\parallel}$) whose population is then depleted through (i) energetic relaxation to the ground polariton state having the same optical alignment ($N_p^{\parallel}$), (ii) intermolecular energy transfer to perpendicular-aligned molecules as well as to other uncoupled molecules having some out-of-plane projection of the dipole moment $N_0^{\times}$ and (iii) decay via other non-radiative channels (γ_{NR}). We propose that intermolecular energy transfer from exciton reservoir $N_x^{\parallel}$ populates exciton reservoirs $N_x^{\perp}$ and $N_x^{\times}$, whose populations are in turn depleted through the same energy relaxation channels, with the $N_x^{\perp}$ reservoir creating polaritons which have an optical alignment that is perpendicular to the excitation laser ($N_p^{\perp}$). **Figure 4.13** shows
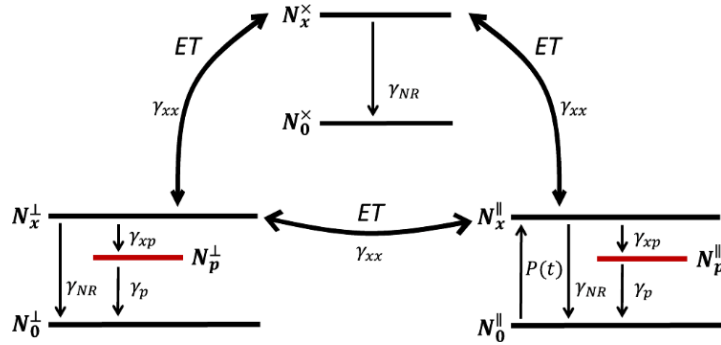
Figure 4.13. Schematic of the molecular transitions and relaxation paths of excited states considered within the theoretical model.

a schematic of molecular transitions and relaxation paths of excited states considered within the model.

In densely-packed organic films, intermolecular energy transfer is an efficient process that results in the ultrafast depolarization of fluorescence [90,91]. When such films are embedded in a strongly-coupled microcavity, intermolecular energy transfer below condensation thresholds is evidenced by a near-zero degree of linear polarization, as shown in Figure 4.4(e). With increasing excitation density and upon condensation threshold, energy relaxation to the ground polariton state becomes stimulated, resulting in sub-picosecond relaxation times, i.e., stimulated relaxation becomes faster than intermolecular energy transfer. Ipso facto polariton condensation occurs with optical alignment parallel to the excitation laser [10,13,14,18]. The interplay between stimulated relaxation to the ground polariton state and intermolecular energy transfer can qualitatively describe the step-wise increase of the degree of linear polarization at the condensation threshold, experimentally observed here in Figure 4.4(e). The quenching of intermolecular energy transfer upon condensation threshold effectively increases the occupation of $N_0^\parallel$-molecules, which in turn quenches the corresponding Rabi-splitting

$$\hbar\Omega^\parallel = \hbar\Omega_0^\parallel \sqrt{1 - \frac{2(N_x^\parallel + N_p^\parallel)}{N_0^\parallel}} \qquad (4.12)$$

and blue-shifts the ground polariton state by:

$$\Delta E_{LPB}^\Omega = 1/2 \cdot \left(E_x + E_c - \sqrt{(E_c - E_x)^2 + (\hbar\Omega^\parallel)^2}\right) - E_{\text{LPB}}^0 \qquad (4.13)$$

where E_{LPB}^0 is the energy of ground polariton state in a limit of small excitation numbers (linear regime), and E_x, E_c are the energies of the bare exciton and cavity modes,

respectively. Analogously, the blueshift accompanied with renormalization of the cavity mode can be described by density-dependent function

$$\Delta E_{LPB}^{c} = 1/2 \cdot \left\{ E_x + E_c \left(1 - \frac{\Delta n}{n_{eff}} \right) - \sqrt{\left(E_c \left(1 - \frac{\Delta n}{n_{eff}} \right) - E_x \right)^2 + (\hbar \Omega_0^{\parallel})^2} \right\} - E_{LPB}^{0} \quad (4.14)$$

where Δn is defined by Eq. (4.10). In the case of small saturation, namely $\frac{(N_x^{\parallel} + N_p^{\parallel})}{N_0^{\parallel}} \ll 1$, the net polariton blueshift ΔE_{LPB} is just a linear superposition of both contributions: $\Delta E_{LPB}^{\Omega} + \Delta E_{LPB}^{c}$ which is well-described by Eq. (4.11). The competition between stimulated relaxation to the ground polariton state and intermolecular energy transfer qualitatively predicts the saturation of the molecular optical transitions that are optically aligned with the excitation laser and the concomitant step-wise energy shift at condensation threshold shown in Figure 4.4(d).

To quantitatively describe the experimental dependences of the polariton emission intensity, energy shift and degree of linear polarization on the increasing excitation density (which have been shown in Figures 4.4(c-e)), we formulate the above model in terms of rate equations (for the details, see Appendix 4):

$$\frac{dN_0^{\parallel,\perp,\times}(t)}{dt} = -P^{\parallel,\perp}(t)N_0^{\parallel,\perp}(t) + N_p^{\parallel,\perp}(t)\gamma_p + N_x^{\parallel,\perp,\times}(t)\gamma_{NR} + N_x^{\parallel,\perp,\times}(t)2\gamma_{xx}$$
$$- N_x^{\times,\parallel,\perp}(t)\gamma_{xx} - N_x^{\perp,\times,\parallel}(t)\gamma_{xx}$$

$$\frac{dN_x^{\parallel,\perp,\times}(t)}{dt} = P^{\parallel,\perp}(t)N_0^{\parallel,\perp}(t) - N_x^{\parallel,\perp}(t)\{N_p^{\parallel,\perp}(t) + 1\}\gamma_{xp} - N_x^{\parallel,\perp,\times}(t)2\gamma_{xx} + N_x^{\times,\parallel,\perp}(t)\gamma_{xx}$$
$$+ N_x^{\perp,\times,\parallel}(t)\gamma_{xx} - N_x^{\parallel,\perp,\times}(t)\gamma_{NR}$$

$$\frac{dN_p^{\parallel,\perp}(t)}{dt} = N_x^{\parallel,\perp}(t)\{N_p^{\parallel,\perp}(t) + 1\}\gamma_{xp} - N_p^{\parallel,\perp}(t)\gamma_p$$

where $P^{\parallel,\perp}(t)$ is the term corresponding to pulsed optical excitation [in the case of linearly-polarized pump $P^{\perp}(t) = 0$], $\gamma_{NR} = 2.5 \cdot 10^8 s^{-1}$ is the nonradiative decay rate of the exciton reservoirs, $\gamma_p = 10^{13} s^{-1}$ is the polariton decay rate, $\gamma_{xx} = 3.33 \cdot 10^{10} s^{-1}$ are decay rates of intermolecular energy transfer between $N_x^{\parallel}$, $N_x^{\perp}$ and $N_x^{\times}$, $\gamma_{xp} = 1.75 \cdot 10^5 s^{-1}$ is the relaxation rate from exciton reservoirs $(N_x^{\parallel}, N_x^{\perp})$ towards the ground polariton states $(N_p^{\parallel}, N_p^{\perp})$, respectively. We note here that in the energy relaxation from the exciton reservoir to the ground polariton state we have included a stimulation term $N_x^{\parallel,\perp}(t) \{N_p^{\parallel,\perp}(t) + 1\} \gamma_{xp}$. The solid lines in **Figure 4.14** show the result of the numerical
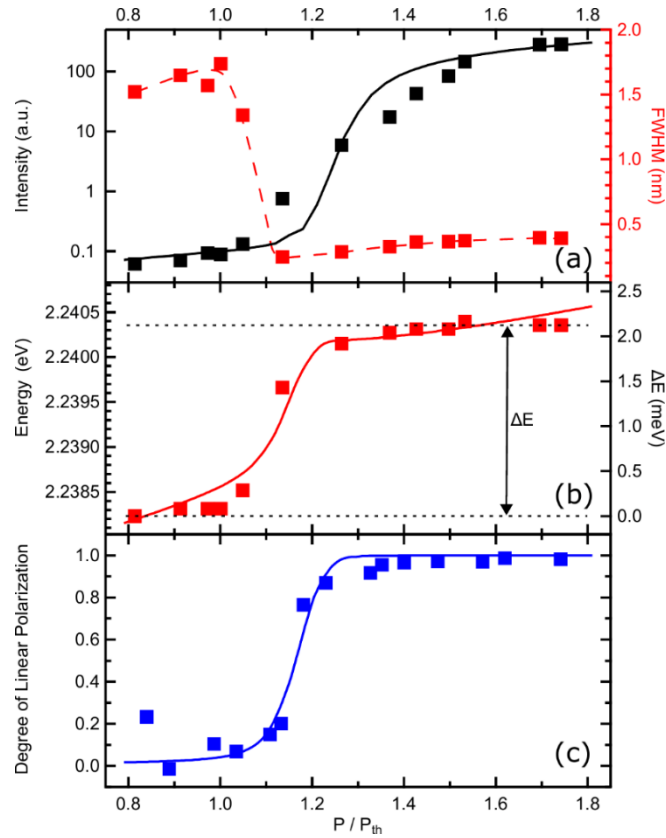
Figure 4.14. Solid curves are the numerical simulation for (a) time-integrated photoluminescence, (b) the ground state energy, and (c) degree of linear polarization pump power dependences compared with experimentally extracted data.

simulations, where we find good quantitative agreement with the experimental observations by using two variable parameters, exciton-to-polariton relaxation rate (γ_{xp}) and the fraction of strongly-coupled molecules (f_c); for details, see Appendix 4. We note here that by switching off intermolecular energy transfer ($\gamma_{xx} = 0$), we obtain a linear dependence of the energy-shift with increasing excitation density that saturates above condensation threshold (see Appendix 4).

We further extend our analysis for the similar strongly-coupled organic microcavities but loaded with the twice lower Bodipy-G1 concentration, 5% samples. With decreasing dye concentration, we observe a reduction in a vacuum Rabi splitting from 116 meV for 10% to 72 meV for 5% samples (see Appendix 5). **Figure 4.15** shows the blueshift versus pump power experimentally recorded for 10% (red) and 5% (blue) samples owing the same exciton fraction $\left|X_{k_{\text{II}}=0}\right|^2 \cong 0.05$. In the case of the 5% sample, we observe the considerably larger blueshift that cannot be explained by merely the Rabi quenching mechanism. Solid lines in Figure 4.15 correspond to numerical simulation containing a density-dependent energy shift due to Rabi quenching and cavity energy shift. Indeed, both the samples exhibit almost the same absorbed power at the threshold, while dye concentration is almost twice different ($\frac{C_{10}}{C_5} = 1.75$). Therefore, one may expect stronger saturation of the optical transition for a 5% sample so that the blueshift defined by the Rabi term in Eq. (4.11) is quite close for both samples. Figure 4.15 unambiguously shows the importance of the cavity energy renormalization term in Eq. (4.11). Since 5% sample exhibits smaller exciton-photon detuning (by means of its modulus $|\delta|$), we observe a

stronger impact of the cavity energy renormalization term on the overall condensate shift (see Appendix 5). Note the higher blueshift in 5% sample is not a matter of luck; we prove it by rigorous analysis of polariton condensates across the whole accessed range of exciton
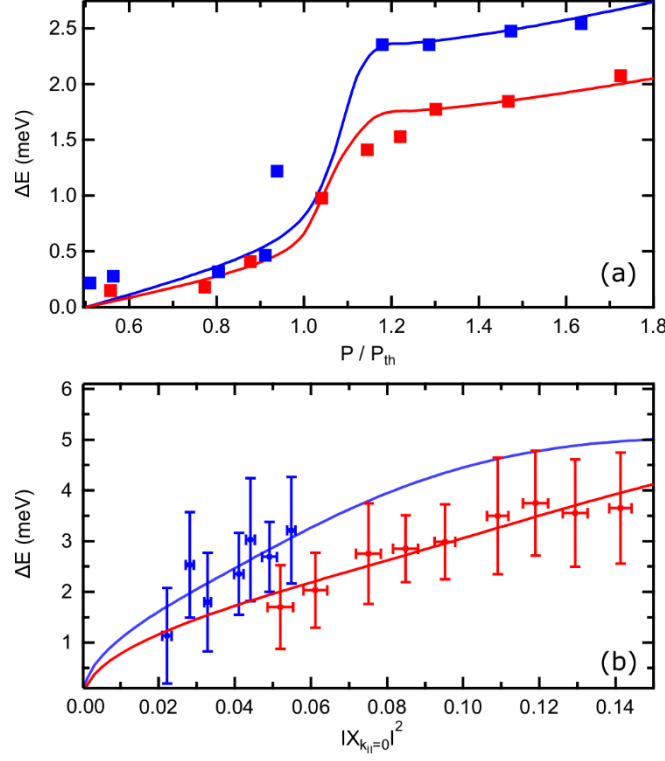
Figure 4.15. (a) The data for polariton blueshifts acquired for 5% (blue) and 10% (red) samples plotted as a function of threshold pump power. Blue and red solid-curves represent numerical simulations of time-integrated blueshifts, respectively. (b) The blueshift ΔE versus exciton-fraction for 5% (blue) and 10% (res) samples, solid curves show the best-fit results according to Eq. (4.11).

fraction. Figure 4.15(b) demonstrates blueshifts as a function of exciton fraction $\left|X_{k_\parallel=0}\right|^2$ plotted for 5% (blue) and 10% (red) samples respectively. We fit the data by Eq. (4.11), where saturation parameter ξ is the only variable, which seems very reasonable, taking into account nearly constant condensation threshold across the range of detuning values allowed (see Figure 3.11). According to the best-fit results, we have saturated the optical transition

for $\xi_{10\%} = 0.03$ and $\xi_{5\%} = 0.05$ for 10% and 5% samples, respectively. The values above correspond to the saturation at the condensation threshold. In the particular case of $\left|X_{k_{\text{II}}=0}\right|^2 \cong 0.05$, we have close contributions due to Rabi quenching ~0.8 meV (see Appendix 6), while renormalization of the cavity mode energy leads to stronger overall polariton energy shift as ΔE_{LPB}^c equals to 1.2 and 2.1 meV for 10% and 5% samples respectively.

Large polariton blueshifts for the "diluted" system is counterintuitive result elucidating the importance of uncoupled molecules. They effectively contribute to the blueshifts via the change in cavity refractive index under the saturation of the exciton transition and lead to peculiar non-monotonous dependence on the exciton fraction as we explore in Appendix 6.

4.6 Conclusion

Unlike inorganic semiconductor microcavities that bear Wannier-Mott excitons, interparticle Coulomb exchange interactions are virtually absent in organic microcavities due to the localized nature of Frenkel excitons in molecular semiconductors. In the absence of Coulomb interactions, the origin of blueshifts in organic semiconductor microcavities and in particular, the step-like energy-shift at condensation threshold have been explained via the interplay of vacuum Rabi splitting, a renormalization of cavity mode energy and intermolecular energy transfer. The ultrafast energy migration mechanism is omnipresent in densely-packed organic films and underlies the rapid depolarization of the emission upon optical excitations. We showed that the step-like blueshift occurs at the condensation

threshold when stimulated relaxation of optically aligned excitons to the ground polariton-state exceeds the rate of intermolecular energy transfer. The interplay of intermolecular energy transfer and stimulated exciton relaxation predicts a step-like increase of the degree of linear polarization related to the step-like blueshift at the condensation threshold which is also observed experimentally. We constructed a simple model of the transient dynamics of optically aligned excitons and polaritons that reproduces qualitatively and quantitatively the ubiquitous step-like blueshift at the condensation threshold in non-crystalline organic microcavities. We shed light on the role of a large reservoir of weakly-coupled molecules elucidating their dominant impact on experimentally observed polariton blueshifts. Finally, we proposed a simple analytic expression discriminating between the contributions to the polariton blueshift. We believe that polariton blueshifts define the energy and momentum distributions for the condensates and relate to their hydrodynamic properties accordingly. Analogously, the effect of the carrier density-dependent nonlinear refractive index change on the energy and momentum polariton distributions has been recently shown in inorganic ZnO microcavities [92].

Chapter 5. Summary and outlooks

In the present thesis, a room temperature polariton lasing has been studied in organic microcavities filled with boron-dipyrromethene fluorescent dyes. The particular wedge-like architecture of the intracavity film, which appeared during the spin-casting process, allowed us to reach the broad detuning range of [-250; -120] meV. We realized that fabricated structures supported strong coupling in whole detuning range; thus, tuneable polariton lasing spanning 33 nm achieved in a green-yellow part of the visible spectrum. However, tuneability precision limited by the blueshift, which has a step-wise dependence on the polariton density.

The origin of the omnipresent in organic microcavities blueshift has been studied by examining the following processes: material gain induced frequency pooling, non-linear effects of the intracavity film, interparticle polariton-polariton and polariton-exciton interactions, and the saturation of molecular optical transitions. We found out and ultimately showed that polariton blueshift in organic microcavities is originated from both the vacuum Rabi-quenching and cavity mode energy renormalization of strongly- and weakly-coupled molecules, respectively, which caused by the saturation of molecular optical transitions. Surprisingly, it turns out that the cavity mode energy renormalization term is the leading one, which drives polariton energy shifts. The present study on the origin of the blueshift is of high importance since the contribution of weakly-coupled molecules was not considered previously. However, the further step in the future development of the theory can be done, if one manages to perform the resonant excitation

of organic microcavities and observe the blueshift there. Such an experiment will provide an extra inside about the polariton's non-linear behavior.

The conducted research contains unique and essential results for the rapidly developing field of organic polaritonics, discovering the potential for organic polariton lasers with the broad tuneability of high precision. Despite the current progress, the application of polariton lasers in devices is limited to date. These limitations are mainly occurring from the fabrication difficulties – the oxidation and contamination of the organic films which contribute to the non-uniform potential formation and high disorders. Because of these adverse effects, organic polariton lasers are not very stable to photodegradation, and power conversion is not high. Moreover, the materials studied so far have a relatively high activation threshold, which, for example, cannot compete with the VCSEL lasers today. Another limiting point is the electrical pumping of the organic microcavities, which proven to be a challenging task.

Thus, we can expect that the next huge step should be done in electrical pumping realization with improved fabrication techniques. If humanity manages to achieve such a result, a low cost, efficient organic polariton lasers will be suited nicely in the applications where the tuneable emission of not high intensities is needed, for example, in microdisplays or scanning lasers for augmented reality with retinal projection. Taking into account the linewidth narrowness of such emitters (~0.1 nm), they will bring a huge impact into the spectroscopy of high resolution.

Appendix 1. *DBR reflectance measurement*

In order to find the reflectance of the DBR, we applied the same method, which we used in [93] for hybrid a-Si solar cells with single-walled carbon nanotubes reflectance measurements. The measurement principle is shown in **Figure S1**. A broad emission of a Xenon lamp was filtered with a monochromator and entered into an integration sphere. The
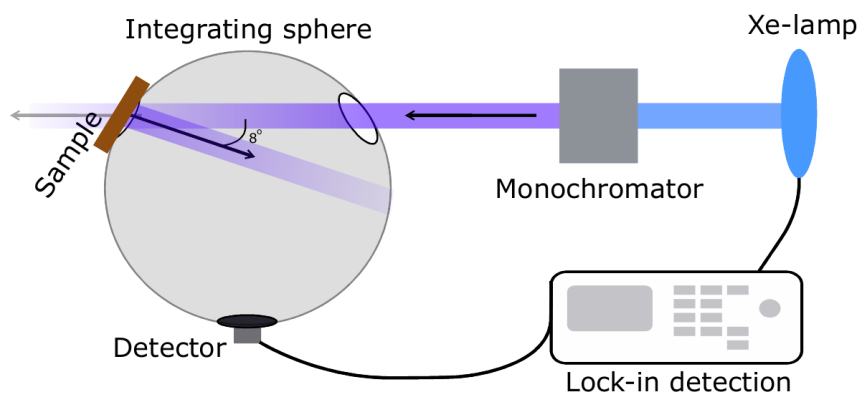
Figure S1. Schematical representation of the reflectance measurement.

internal surface of the sphere made from barium sulphate ($BaSO_4$), which is known to be a material with high reflectance (>98%) in the 250 - 2500 nm (UV-VIS-NIR) wavelength range. By placing the calibration sample from $BaSO_4$ to the sample slot, the incident radiation is confined in the sphere, and after several reflections, it is collected on the detector. The sensitive lock-in detection allowed to increase the signal-to-noise ratio. After the calibration, the curve corresponding to the Xe-lamp spectrum was recorded (100% reflectance curve). Following that, the sample which has to be measured is placed to the slot, and its reflectance is found by dividing the measured signal to the calibration values. Using this approach, we found that the first DBR reflects 20% of the incident pump. Therefore, only 4.8 mJ cm^{-2} is incident on the BODIPY-G1 film inside the cavity.

Appendix 2. *Microscopic model of the quenching of the Rabi splitting* [3*]

The origin of the nonlinear optical coupling between a cavity mode and Frenkel excitons comes from the observation that excitons correspond to bosons only in the limit of small excitation numbers. This is easy to see in the case of Frenkel excitons, where each excitation can be described by the Pauli creation (annihilation) operator σ_j^+ (σ_j^-), which are two-level raising and lowering operators, acting at the site j. The corresponding σ_j^z operator then describes the presence of an excitation (akin to density operator). In the limit when the total number of excitations n_T is much less than the total number of the sites n_0, one can perform Holstein-Primakoff transformation, collective excitation for the ensemble of two-level systems becomes a boson, and the system consisting of a cavity plus and active organic material can be nicely described by the model of two coupled bosonic modes. However, once the excitation power grows and condition $n_T << n_0$ does not hold anymore, the effects of the saturation of the absorption start to play a role and a simple model of two coupled oscillators breaks down.

To build the microscopic model corresponding to this regime, we describe a delocalized Frenkel exciton in the momentum-space form using the Fourier transformed operators: $\sigma_k^+ = \frac{1}{n_0}\sum_{j=1}^{n_e} \sigma_j^+ e^{ikr_j}$ where k is an in-plane wavevector for the exciton, and the density operator is defined through commutation relations $[\sigma_k^+; \sigma_{k'}^z] = -2\sigma_{k+k'}^+$, $[\sigma_k^-; \sigma_{k'}^z] = 2\sigma_{k-k'}^-$. The Hamiltonian for Frenkel excitons coupled to light reads

---

[3] The model was described by Oleksandr Kyriienko and Ivan Shelykh; there is no conflict of interests of authors.

$$\hat{H}_0 = \frac{1}{2}\sum_k E_X(k)\sigma_k^z + \sum_k E_C(k)a_k^+ a_k + \hbar g \sum_k (\sigma_k^+ a_k + \sigma_k^- a_k^+)$$

where the first term describes excitons with dispersion $E_X(k)$ the second term corresponds to the cavity mode with dispersion $E_C(k)$, and the last term describes the light-matter coupling term with characteristic constant g. The operators $a_k^+ (a_k)$ correspond to bosonic creation (annihilation) operators of the quantized electromagnetic cavity mode.

To describe the optical response of the system, we calculate the Green's function of a cavity photon [94] $\langle\langle a_k | a_k^+ \rangle\rangle_t = -i\theta(t)\langle[a_k(t); a_k^+(0)]\rangle$ where index t means that we work in the time domain, and the time dependent operators $a_k(t)$ can be readily obtained from the Heisenberg equations of motion. We then perform the Fourier transform of $\langle\langle a_k | a_k^+ \rangle\rangle_t$ and get the following equation:

$$(\hbar\omega - E_c(k))\langle\langle a_k | a_k^+ \rangle\rangle_\omega = 1 + \hbar g\langle\langle \sigma_k^- | a_k^+ \rangle\rangle_\omega$$

Here, the last term appears due to the light-matter coupling. In the same way the equation of motion for $\langle\langle \sigma_k^- | a_k^+ \rangle\rangle_\omega$ propagator can be derived, and the system of the equations can be closed by performing Wick-decoupling at the mean-field level which yields

$$\sum_k [(\hbar\omega - E_X(k))(\hbar\omega - E_C(k))\delta_{k,k'} - 2\hbar^2 g^2 \langle\sigma_{k-k'}^z\rangle]\langle\langle a_{k'} | a_k^+ \rangle\rangle_\omega = 1$$

The spectrum can be defined from the poles of the Green function corresponding to the zeroes of the determinant of the system. This gives the following equation for the dispersions of the polariton modes:

$$E_{UPB,LPB}(n_T) = \frac{1}{2}\left(E_C + E_X \pm \sqrt{(E_C - E_X)^2 + \hbar^2\Omega^2(n_T)}\right)$$

Where the characteristic vacuum Rabi splitting decreases with the increase of the total number of excitations in the system due to the saturable absorption and reads:

$$\hbar\Omega(n_T) = 2\hbar g\sqrt{n_0 - 2n_T} = \hbar\Omega_0\sqrt{1 - \frac{2n_T}{n_0}}$$

where $\Omega_0 = 2g\sqrt{n_0}$ is characteristic vacuum Rabi splitting in the linear regime, $n_T = n_x + n_p$ is the total number of excitation, namely the sum of excitons and polaritons. Note, that as expected vacuum Rabi splitting decreases with increase of the number of the excitations and becomes zero when half of the molecules become excited.

Appendix 3. *Kramers-Kronig mechanism analysis*

Here, we describe technical details related to the Kramers-Kronig analysis (KK) represented in Section 4.4.4 of the main text. First of all, we define an imaginary part of the complex refractive index by using the well-known relation in between of absorbance (*Abs*) and dimensionless values of $k(\omega)$:

$$k(\omega) = \frac{\lambda \cdot Abs}{L} \cdot \frac{ln10}{4\pi}$$

where λ is the wavelength attributed to the particular *Abs* value, and L is the film thickness.

We use the data from absorption measurements of a reference film having the same host material, dye concentration, and thickness as the cavity layer. Normalized absorbance is shown in Figure 4.1, so the peak value of *Abs* measured for 172 nm thick film is equal to 0.35. **Figure S2** shows the imaginary part of the cavity material (black/grey shaded curve).
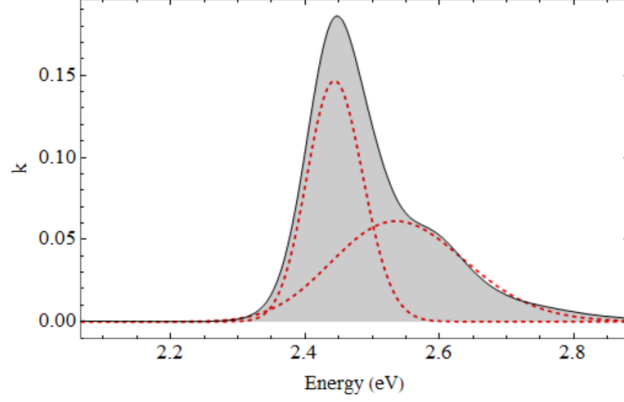
Figure S2. The imaginary part of the complex refractive index of the cavity material as a function of energy (eV). Black/grey shaded curve corresponds to the experimental data; red dashed lines represent the best-fit result using Gaussian functions.

The next step: we calculate the real part of the complex refractive index by means of KK relation. As it involves finding the Cauchy principle value of the integral, we use an analytic expression for the imaginary part $k(\omega)$. The best-fit of the experimental $k(\omega)$ dependence results in a sum over Gaussian functions in the following form:

$$k(\omega) = \sum_i A_i e^{\frac{-(\omega - \omega_{o,i})^2}{2\sigma_i^2}}$$

In our case, we have the sum over $i = 1,2$ as the spectrum consist of two inhomogeneously broadened molecular optical transitions, namely centred at $\hbar\omega_{o,1} = 2.446$ eV and $\hbar\omega_{o,2} = 2.548$ eV respectively. The best-fit parameters are the following: $\hbar\sigma_1 = 42$ meV, $\hbar\sigma_2 = 94$ meV, $A_1 = 0.15, A_2 = 0.06$. The fit result demonstrates an excellent agreement with the experimental dependence (Figure S2).

Here we recall the KK relation in the general form given in the main text is equivalent to Hilbert transform $H(\omega)$ as

$$n(\omega) = \frac{1}{\pi} P.V. \int_{-\infty}^{+\infty} \frac{k(\omega')}{\omega - \omega'} d\omega' = -H(\omega)$$

The Hilbert transform of a Gaussian distribution is a well-known function and can be related to the Dawson function (integral) as follows

$$H(\omega) = \frac{2}{\sqrt{\pi}} \cdot e^{-\omega^2} \int_0^\omega e^{t^2} dt = \frac{2}{\sqrt{\pi}} \cdot F[\omega]$$

where $F[\omega]$ is the Dawson function.

In case of the sum over Gaussian functions, the total real part of the complex refractive index describes by the Hilbert transform of the sum accordingly:

$$n(\omega) = -\sum_i H(\omega_i) = -\frac{2}{\sqrt{\pi}} \sum_i A_i e^{\frac{-(\omega - \omega_{o,i})^2}{2\sigma_i^2}} \int_0^{\frac{(\omega - \omega_{o,i})}{\sigma_i \sqrt{2}}} e^{t^2} dt$$

$$= -\frac{2}{\sqrt{\pi}} \sum_i A_i \cdot F[\frac{(\omega - \omega_{o,i})}{\sigma_i \sqrt{2}}]$$

where $F\left[\frac{(\omega - \omega_{o,i})}{\sigma_i \sqrt{2}}\right]$ is the Dawson function (integral) with the argument $\frac{(\omega - \omega_{o,i})}{\sigma_i \sqrt{2}}$.

We use this result in the main text and plot both real and imaginary parts of the complex refractive index in Figure 4.11(a). As the real part is proportional to $A_{1,2}$ parameters, any change in the absorption efficiency would immediately reflect in the values of the real part. We define the change in the real part Δn as a simple difference between $n(\omega)$ associated with saturated optical transitions to its initial value. Figure 4.11(a) of the main text demonstrates the effect of decreasing the imaginary part for 10% of its initial value. Therefore, the difference caused by saturating transitions is equal to:

$$\Delta n(\omega) = n(\omega)|_\xi - n(\omega)|_0 = -\xi \frac{2}{\sqrt{\pi}} \sum_i A_i \cdot F[\frac{(\omega - \omega_{o,i})}{\sigma_i \sqrt{2}}] = -\frac{1}{5} \xi \cdot \alpha \cdot F[\frac{(\omega - \omega_{o,i})}{\sigma_i \sqrt{2}}]$$

where $\xi \cong \frac{n_x}{n_0} \ll 1$ is the small saturation parameter as the number of excited molecules n_x

is much lower than the total number of molecules n_0.

In **Figure S3**, we illustrate the change in the real part of complex refractive index

Δn caused by the saturation of molecular optical transitions for 10% ($\xi = 0.1$).
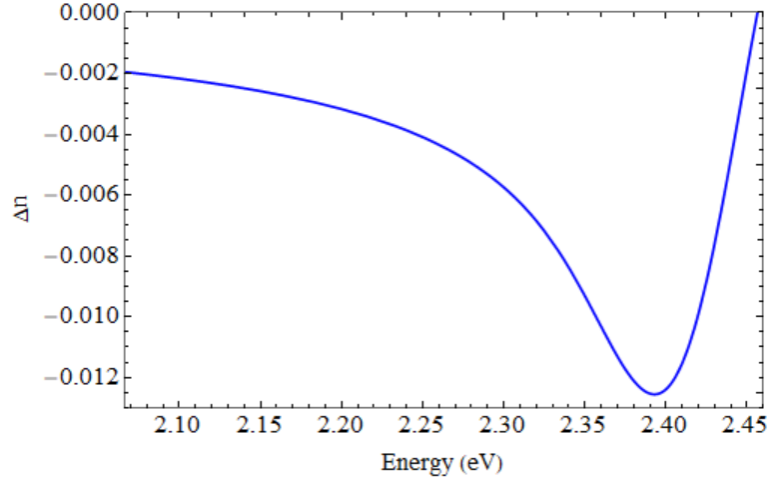
Figure S3. The change in the real part of refractive index Δn versus energy. The induced difference caused by the saturation of molecular optical transitions for 10% of the initial value ($\xi = 0.1$).

Appendix 4. Numerical simulations [4*]

Numerical simulations are based on the rate equations derived for the molecules with a parallel-aligned dipole moment $N_0^\parallel$ and with orthogonal optical alignment $N_0^\perp, N_0^\times$. Figure 4.13 of the main text shows a schematic of molecular transitions and relaxation paths of excited states considered within the model.

Explicitly, the rate equations are expressed as follows:

$$\frac{dN_0^\parallel(t)}{dt} = -P^\parallel(t)N_0^\parallel(t) + N_p^\parallel(t)\gamma_p + N_x^\parallel(t)\gamma_{\text{NR}} + N_x^\parallel(t)2\gamma_{xx} - N_x^\times(t)\gamma_{xx} - N_x^\perp(t)\gamma_{xx}$$

$$\frac{dN_0^\perp(t)}{dt} = N_p^\perp(t)\gamma_p + N_x^\perp(t)\gamma_{\text{NR}} + N_x^\perp(t)2\gamma_{xx} - N_x^\parallel(t)\gamma_{xx} - N_x^\times(t)\gamma_{xx}$$

$$\frac{dN_0^\times(t)}{dt} = N_x^\times(t)\gamma_{\text{NR}} + N_x^\times(t)2\gamma_{xx} - N_x^\perp(t)\gamma_{xx} - N_x^\parallel(t)\gamma_{xx}$$

$$\frac{dN_x^\parallel(t)}{dt} = P^\parallel(t)N_0^\parallel(t) - N_x^\parallel(t)\{N_p^\parallel(t) + 1\}\gamma_{xp} - N_x^\parallel(t)2\gamma_{xx} + N_x^\times(t)\gamma_{xx} + N_x^\perp(t)\gamma_{xx}$$
$$- N_x^\parallel(t)\gamma_{\text{NR}}$$

$$\frac{dN_x^\perp(t)}{dt} = -N_x^\perp(t)\{N_p^\perp(t) + 1\}\gamma_{xp} - N_x^\perp(t)2\gamma_{xx} + N_x^\parallel(t)\gamma_{xx} + N_x^\times(t)\gamma_{xx} - N_x^\perp(t)\gamma_{\text{NR}}$$

$$\frac{dN_x^\times(t)}{dt} = -N_x^\times(t)2\gamma_{xx} + N_x^\perp(t)\gamma_{xx} + N_x^\parallel(t)\gamma_{xx} - N_x^\times(t)\gamma_{\text{NR}}$$

$$\frac{dN_p^\parallel(t)}{dt} = N_x^\parallel(t)\{N_p^\parallel(t) + 1\}\gamma_{xp} - N_p^\parallel(t)\gamma_p$$

$$\frac{dN_p^\perp(t)}{dt} = N_x^\perp(t)\{N_p^\perp(t) + 1\}\gamma_{xp} - N_p^\perp(t)\gamma_p$$

---

[4] The numerical simulation has been fully performed by the Anton Zasedatelev; there is no conflict of interests of authors.

The pump term $P(t)$ corresponds to the linearly polarized 2 ps pulsed non-resonant optical excitation with Gaussian temporal profile. The effective non-radiative decay rate of the exciton reservoirs $\gamma_{NR} = 2.5 \cdot 10^8 s^{-1}$ is calculated from known values of quantum yield and a total lifetime of excited states according to [91]. The rates of an intermolecular energy transfer corresponding to depolarization processes are taken from time-resolved polarization anisotropy measurements. According to the study [91], polarization decay time for the material is less than 50 ps (limited by the setup time-resolution); thus we use the reasonable value of $\gamma_{xx} = 3.33 \cdot 10^{10} s^{-1}$. Polariton lifetime has been calculated from the full width at half maximum of the emission linewidth below the threshold (1.5 nm) as 100 fs, so that the decay rate is equal $\gamma_p = 10^{13} s^{-1}$ regardless optical alignment since the ground polariton state is degenerate for TE/TM modes at $k \sim 0$.

We estimated total dye density N_{tot} in the cavity as $1.3 \cdot 10^{20}$ molecules per cm^3 using Beer-Lambert law and taking into account experimental values of the film thickness L = 172 nm, absorbance at 507 nm is $A = 0.35$, molar extinction ratio $\varepsilon = 95500$ cm^{-1} M^{-1} [69] and molecular weight of the dye M = 384,18 g mol^{-1}. However, the only small fraction of molecules randomly distributed in the cavity undergoes strong light-matter interaction. We introduce a coupling coefficient f_c defining the density of coupled molecules as $N_0^{\parallel} = N_0^{\perp} = N_0^{\times} = \frac{f_c N_{tot}}{3}$. The coupling coefficient f_c as well as exciton-to-polariton relaxation rates γ_{xp} are the variable parameters. We impose an experimental criterion for them satisfying polariton condensation that appears at the exciton density of 5% of the total dye density N_{tot}. We assume that both exciton reservoirs exhibit the same exciton-to-polariton decay rate γ_{xp} which is reasonable approximation since the ground

polariton state is fully degenerate in terms of polarization, and the molecules are randomly distributed over the cavity volume.

By applying the following boundary conditions

$$N_0^\parallel(t=0) = N_0^\perp(t=0) = N_0^\times(t=0) = \frac{f_c\, N_{tot}}{3}$$

$$N_x^\parallel(t=0) = N_x^\perp(t=0) = N_x^\times(t=0) = N_p^\parallel(t=0) = N_p^\perp(t=0) = 0$$

we simulated the total time-integrated PL as a function of pump power:

$$PL = \int_0^T \{N_p^\parallel(t) + N_p^\perp(t)\}\, dt$$

where an upper bound of the numerical integration $T = 3\tau$, where $\tau = 4\ ns$ - effective lifetime of excited states of the dye molecule [91] is used to ensure reliable results as for below and above the condensation threshold. We fit the experimental dependence of the integrated PL on the pump power by using the model with f_c and γ_{xp} are being variable parameters. Figure 4.14(a) (solid black curve) shows the best fit result, where $f_c = 0.15$ and $\gamma_{xp} = 1.75 \cdot 10^5\ s^{-1}$. Surprisingly we find out an excellent agreement of the fit parameter γ_{xp} with the experimentally extracted rate of exciton-to-polariton relaxation. Following the extensive study of polariton population mechanisms in strongly-coupled dye-filled microcavities [95], the dominant process populating polariton states is the so-called intracavity radiative pumping. Briefly, the spontaneous radiative emission of the fluorescent dye effectively populates polariton states through a radiative decay inside the cavity. We perform the quantitative analysis of the exciton-to-polariton relaxation rate based on the phenomenology developed in Ref. [95]. The total radiative relaxation rate of exciton reservoirs can be considered as follows:

$$\gamma_R = W_R \cdot \int_{\omega_1}^{\omega_2} I_{PL}(\omega)d\omega$$

where the integration is done for the whole frequency range of $I_{PL}(\omega)$ which is the normalized emission (PL) spectrum, W_R is the effective scattering rate of the radiative relaxation process.

The scattering rate W_R defines overall radiative relaxation of the exciton reservoir according to the equation above. From the time-resolved photoluminescence measurements (TRPL) [91] we know the total relaxation rate $\gamma_R = 2.5 \cdot 10^7 \ s^{-1}$. The black/grey shaded curve in **Figure S4** shows the normalized PL spectrum as the function of photon energy (eV).
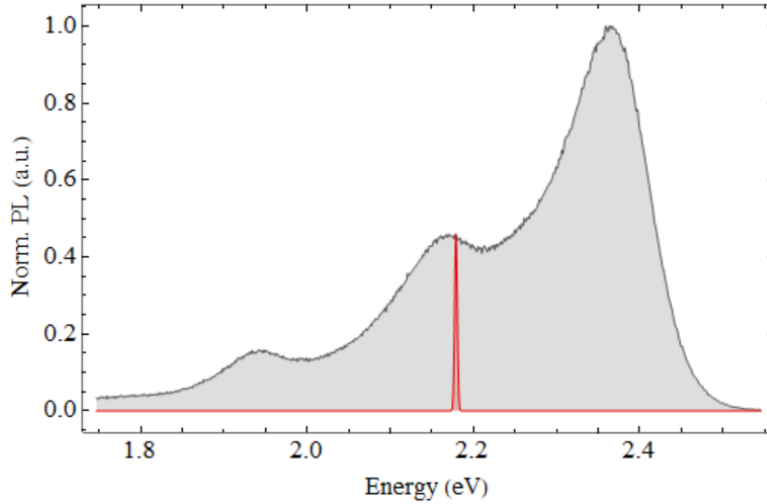
Figure S4. The black/grey shaded curve shows the normalized photoluminescence (PL) spectrum of the bare cavity. The red shaded curve shows the part of PL invoked to the population of polariton states in the vicinity to the ground state ($k_\parallel = 0$).

By integrating the PL spectrum over the whole spectral range, we retrieve the effective scattering rate from the above equation: $W_R = 4.15 \cdot 10^5 \ s^{-1}$. Following the same approach, we can now calculate the exciton-to-polariton relaxation rate as

$$\gamma_{xp} = |C|^2 \cdot W_R \cdot \int_{\omega_{p1}}^{\omega_{p2}} I_{PL}(\omega)d\omega$$

where the integral is calculated within the range of polariton states under investigation $\omega \in [\omega_{p1}, \omega_{p2}]$, $|C|^2$ is an average Hopfield coefficient within the polariton states of $\omega \in [\omega_{p1}, \omega_{p2}]$, it reflects photon fraction of the polariton wave-function.

The red shaded curve in Figure S4 indicates a part of the spectrum corresponding to the population of the polariton states invoked to the process. The calculation results in $\gamma_{xp} = 1.86 \cdot 10^5 \ s^{-1}$, as the photon fraction $|C|^2$ equals 0.93, according to Figure 4.9(d) of the main text. One can see the remarkable agreement between the model, $\gamma_{xp} = 1.75 \cdot 10^5 \ s^{-1}$, and experimental relaxation rates obtained independently. The values seem reasonable if one compares it with other studies, for instance, microscopic analysis of radiative pumping rate in anthracene based strongly-coupled microcavities came up with a similar value of γ_{xp} equals to $5 \cdot 10^5 \ s^{-1}$ [96].

The energy of the ground polariton state has been calculated numerically using time-dependent exciton and polariton densities $N_x^{\parallel,\perp}(t), N_p^{\parallel,\perp}(t)$ from the rate equations.

$$E_{LPB}^{\parallel,\perp}(t) = 1/2 \cdot \left(E_x + E_c \left(1 - \frac{\Delta n^{\parallel,\perp}(t)}{n_{eff}} \right) - \sqrt{ \left(E_c \left(1 - \frac{\Delta n^{\parallel,\perp}(t)}{n_{eff}} \right) - E_x \right)^2 + \{\hbar\Omega^{\parallel,\perp}(t)\}^2 } \right)$$

where $E_x = 2.446 \ eV$ and $E_c = 2.254 \ eV$ are the energies of the bare exciton and cavity modes respectively, $n_{eff} = 1.81$ is the effective cavity refractive index, $\hbar\Omega^{\parallel,\perp}(t) = $

$\hbar\Omega_0^{\parallel,\perp} \sqrt{ 1 - 2\frac{N_x^{\parallel,\perp}(t) + N_p^{\parallel,\perp}(t)}{N_0^{\parallel,\perp}(t)} }$ is the quenched vacuum Rabi splitting, $\hbar\Omega_0^{\parallel,\perp} = 116 \ meV$ is the average vacuum Rabi splitting measured across the detuning range at the limit of zero

occupancies, $\Delta n^{\parallel,\perp}(t) = -\frac{1}{5}\frac{N_x^{\parallel,\perp}(t)}{N_0^{\parallel,\perp}(t)} \cdot \alpha \cdot F[d]$ is the density-dependent change of the

effective cavity refractive index.

Since the cavity energy renormalization term invokes the subset of weakly-coupled

molecules, we calculate the time-dependent change in the refractive index $\Delta n^{\parallel,\perp}(t)$ by

using the same rate equations above without considering densities of polariton states

$N_p^{\parallel,\perp}(t)$ and applying the following boundary conditions:

$$N_0^{\parallel}(t = 0) = N_0^{\perp}(t = 0) = N_0^{\times}(t = 0) = (1 - f_c) \cdot \frac{N_{tot}}{3}$$

$$N_x^{\parallel}(t = 0) = N_x^{\perp}(t = 0) = N_x^{\times}(t = 0) = 0$$

To compare the result of modeling with experimentally observed values, we calculate time-

integrated blueshift:

$$E_{LPB}^{\parallel,\perp} = \frac{\int_0^T E_{LPB}^{\parallel,\perp}(t) \cdot N_p^{\parallel,\perp}(t)\, dt}{\int_0^T N_p^{\parallel,\perp}(t)\, dt}$$

$$E_{LPB}^T = E_{LPB}^{\parallel} \cdot \frac{1}{PL}\int_0^T N_p^{\parallel}(t)\, dt + E_{LPB}^{\perp} \cdot \frac{1}{PL}\int_0^T N_p^{\perp}(t)\, dt$$

Figure 4.14(b) of the main text demonstrates the quantitative agreement of the theory with

experimental data. It is worth noting that in Figure 4.14(b) we plot relative blueshift defined

as $\Delta E = E_{LPB}|_P - E_{LPB}|_{P=0.8P_{th}}$ as extracted from experimental data.

To demonstrate the role of the ET in the polariton dynamics we purposely forbid

the processes of energy migration between exciton reservoirs assuming $\gamma_{xx} = 0$. **Figure

S5** shows the energy of the ground polariton state predicted by the model with (black solid

curve) and without intermolecular energy transfer (black dashed curve).
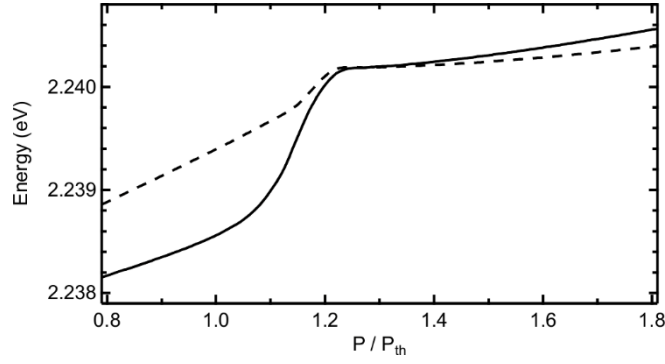
Figure S5. The ground polariton state energy versus relative pump power (P/P$_{th}$) simulated numerically using the model with (solid curve) and without intermolecular energy transfer (dashed curve).

In order to model the degree of linear polarization (DLP), we used time-dependent parallel and perpendicular aligned polariton densities $N_p^{\parallel}(t)$ and $N_p^{\perp}(t)$ respectively. Since we use horizontally polarized optical excitation time-integrated DLP has been calculated in accordance with the following expression:

$$DLP = \frac{\int_0^T \{N_p^{\parallel}(t) - N_p^{\perp}(t)\}\, dt}{\int_0^T \{N_p^{\parallel}(t) + N_p^{\perp}(t)\}\, dt}$$

Figure 4.14(c) of the main text shows the result of the numerical simulation of DLP versus pump power. Note, the condensate above the threshold follows horizontal polarization as initially induced by the pump beam.

Appendix 5. *Strong coupling and blueshifts for the 5% sample*

To gain an in-depth insight into the impact of cavity energy renormalization on the overall polariton blueshift, we fabricate the same strongly coupled microcavities but loaded with approximately twice lower amount of BODIPY-G1molecules, namely 5% concentration by weight. Fabrication procedures utilized are the same as for 10% samples.

We apply the same techniques investigating strong coupling phenomenon and use the same fitting model to extract vacuum Rabi splitting ($\hbar\Omega_0$), detuning (δ) and calculate Hopfield coefficients ($|C|^2, |X|^2$). **Figure S6** shows the typical angle-resolved reflectivity map acquired for the 5% sample. One can see clear anti-crossing between lower and upper polariton branches observed at ~40° incidence. We employ the two coupled-oscillator model described in Section 2.1.3 to extract the parameters of strong coupling. The model well describes the newly appeared polariton modes with the following parameter set: $\hbar\Omega_0 = 72$ meV, $\delta = -146$ meV, while reasonably keeping the energy of exciton mode and cavity effective refractive index fixed and being similar to the case of 10% sample: $E_X = 2.446$ eV, $n_{eff} = 1.81$.
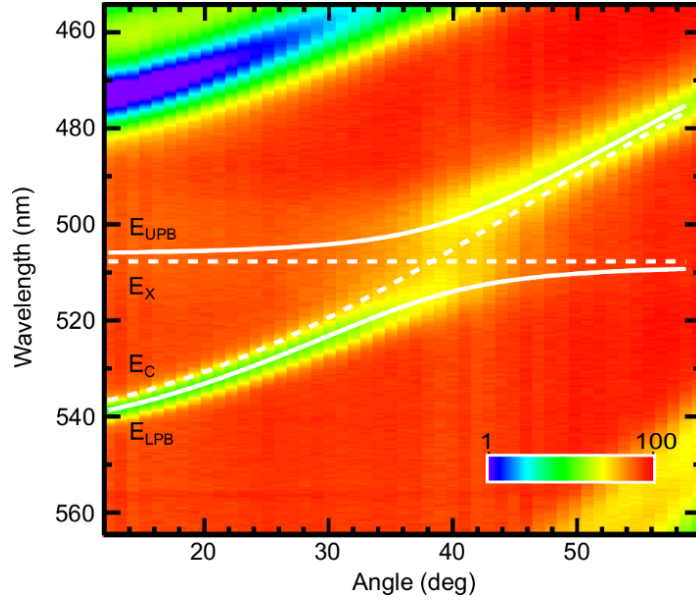
Figure S6. The angle-resolved reflectivity map measured for the 5% sample. Best-fit results for the upper (E_{UPB}) and lower (E_{LPB}) polariton branches all together with the cavity mode E_C and energy of exciton resonance E_X are shown as white solid and dashed curves accordingly.

Figure S7 shows the measured energy-shift for ~300 single-shot measurements of polariton condensation in the whole possible range of polariton ground state energies allowed within the 5% sample area. For each measurement, the energy-shift is defined by
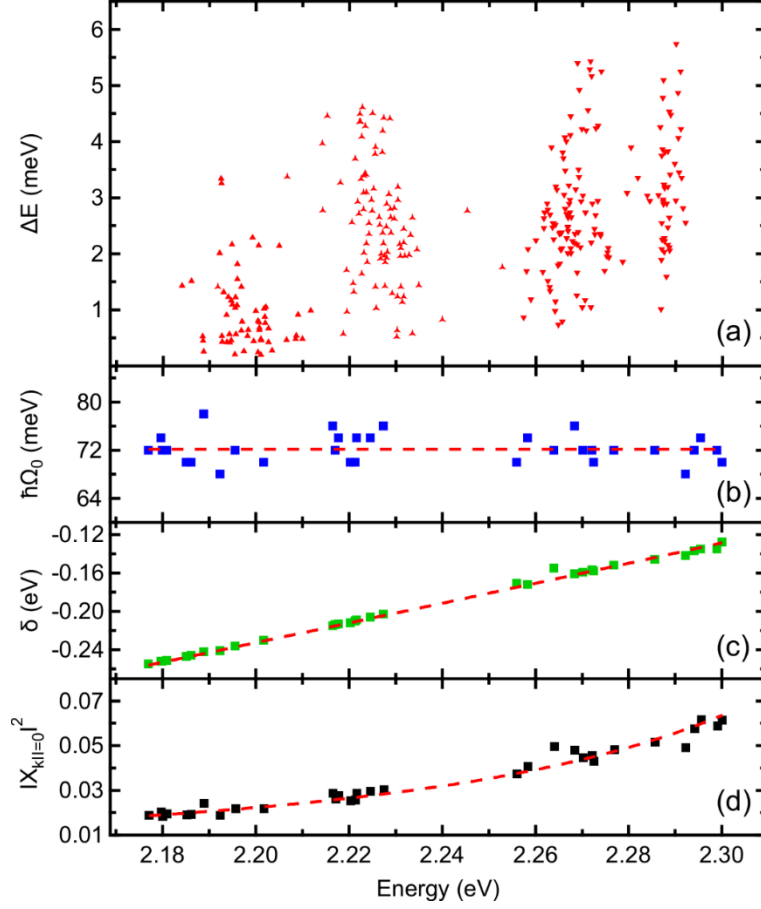
Figure S7. Analysis of strong coupling parameters and polariton blueshifts observed in a 5% sample. (a) Scattering plot that shows single-shot blueshift realizations across the whole sample area. (b) Vacuum Rabi splitting $\hbar\Omega_0$ with an average value of (72 ± 2.5) meV (red dashed curve) and (c) detuning δ extracted from the multiple angle-dependent reflectivity measurements carried out across the sample area. (d) The exciton fraction $\left| X_{k_{II}=0} \right|^2$ at the ground state of the polariton wave function, calculated from extracted $\hbar\Omega_0$ and δ values. Red dashed curves in (c) and (d) correspond to analytical fit functions for δ and $\left| X_{k_{II}=0} \right|^2$, respectively.

comparing the energy of the emission below (~0.8P_{th}) and above threshold (~1.4P_{th}). Here, we avoid averaging over the intensity fluctuations of the laser by utilizing a single-shot

dispersion imaging technique. By fitting angle-dependent reflectivity maps acquired for the 5% sample across the entire accessible polariton ground state energies, we extract the relevant strong coupling parameters represented in Figure S7(b-d), respectively. We find the vacuum Rabi splitting is invariant within the detuning range, with an average value of $\hbar\Omega_0 = 72 \pm 2.5$ meV.

Figure S7(c) indicates an excellent agreement between the fitting result for detuning values δ and theoretical predictions plotted as red dashed curve according to the analytical expression:

$$\delta = \frac{\left(\frac{\hbar\Omega_0}{2}\right)^2 - E_X{}^2 + E_{LPB} \cdot (2E_X - 1)}{E_X - E_{LPB}}$$

Similarly, from Figure S7(d) one can see an excellent agreement for the exciton fraction at the ground state of polariton wave-functions as it is described by the following:

$$|X|^2, |C|^2 = \frac{1}{2}\left(1 \pm \frac{\delta}{\sqrt{\delta^2 + (\hbar\Omega_0)^2}}\right)$$

where we use detuning δ in the form of the above analytical expression.

As the only difference between 5% and 10% samples is in dye concentrations, we can easily calculate real and imaginary parts of the complex refractive index just by scaling $k(\omega)$ and $n(\omega)$ according to the absorption maximum for the 5% cavity layer. Note normalized absorption spectra for both dye concentrations are the same, while the peak values relate to each other as $\frac{Abs_{10\%}}{Abs_{5\%}} = 1.75$. **Figure S8(a)** shows the imaginary and real parts of the complex refractive index as the function of energy.
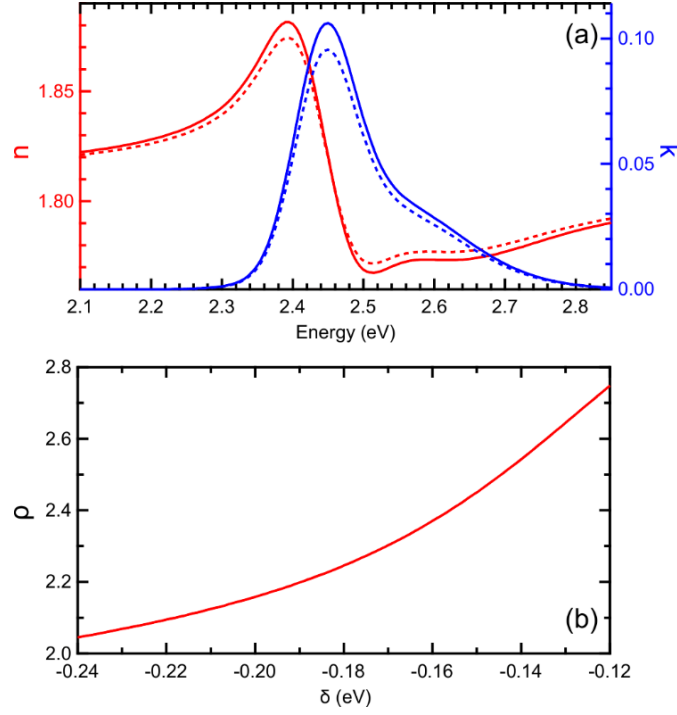
Figure S8. (a) Real (red) and imaginary (blue) parts of the complex refractive index for 5% sample plotted for the case of unperturbed (solid) and saturated (dashed) molecular transition, respectively. Here we saturate the transition for the 10 percent. (b) The ratio $\rho = \frac{\Delta E_{LPB}^{c}}{\Delta E_{LPB}^{\Omega}}$ shows relative contributions of renormalization in the cavity mode energy and the Rabi-quenching term to overall polariton blueshift as a function of exciton-photon detuning for 5% sample.

Using Eq. (4.11) of the main text and extracted parameters above, we calculate the relative contributions of the energy shift induced by the cavity mode energy renormalization and the Rabi-quenching terms by means of the ratio ρ.

$$\rho = \frac{\Delta E_{LPB}^{c}}{\Delta E_{LPB}^{\Omega}} = \frac{(E_x - |\delta|) \cdot F[d] \cdot \alpha \cdot \left(\sqrt{1 + s^2} + 1\right)}{5 n_{eff} \cdot s \cdot \hbar \Omega_0}$$

Figure S8(b) indicates the dominant role of cavity mode renormalization term in the overall polariton blueshift.

Appendix 6. *Polariton blueshift versus exciton fraction*

Since we experimentally observe nearly the same condensation threshold across the entire detuning range, it seems reasonable to assume nearly the same parameter set is valid for the rate equations with respect to all possible detuning values. Otherwise, it should affect the condensation threshold, which is not the case. Relying on this fact, one can easily simulate the total blueshift versus exciton fraction using Eq. (4.11), where saturation parameter ξ can be considered as the variable parameter to fit experimental data. Despite Eq. (4.11) is the approximate expression derived for the total blueshift mentioned above, it provides entirely accurate results in the limit of $\xi \ll 0$. Figure 4.15(b) of the main text shows best-fit results for the observed polariton blueshift versus exciton fraction of polariton wave-function at the ground state $\left|X_{k_{\mathrm{II}}=0}\right|^2$. Here we extend the dependences for a broad range of exciton fractions up to 0.5 and provide a separate analysis of both contributions: the cavity mode energy renormalization and Rabi-quenching. **Figure S9** represents polariton blueshifts as the function of exciton fraction.
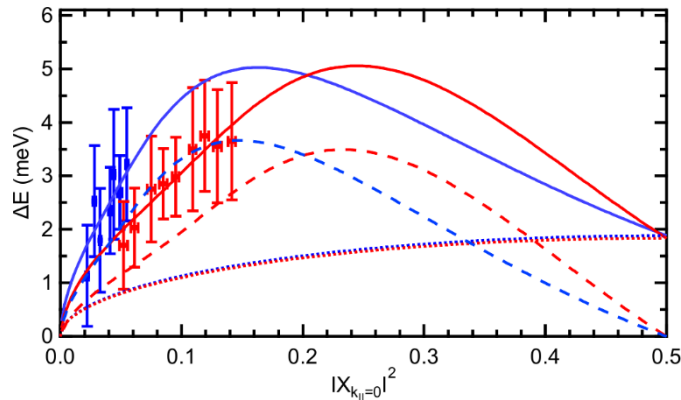

Figure S9. The blueshift ΔE versus exciton-fraction for 5% (blue) and 10% (red) samples. Solid curves show the best-fit results, according to Eq. (4.11). Short dashed

curves correspond to the Rabi-quenching term, while the long dashed curves are associated with the cavity mode energy renormalization.

In both 5 and 10 percent concentration cases, we have square root dependence for the Rabi-quenching term on the exciton fraction as expected from the conventional formalism of strong coupling. Moreover, the Rabi-quenching terms exhibit the same absolute values for both samples since the following equality is valid $\xi_{5\%} \cdot \hbar\Omega_{0(5\%)} \cong \xi_{10\%} \cdot \hbar\Omega_{0(10\%)}$. Regarding the cavity mode energy renormalization term, one can observe the higher contribution corresponding to the "diluted" – 5% sample with respect to 10%. It has quite a simple explanation associated with the Dawson function, which is larger for 5% sample as it exhibits $m = \frac{\hbar\Omega_{0(10\%)}}{\hbar\Omega_{0(5\%)}}$ times lower detuning $|\delta|$ at the same exciton fraction. However, it shows the opposite trend when a derivative of the Dawson function changes the sign, as shown in Figure S9. Extrapolating the assumption of the constant rates in the rate equations on the entire range of exciton fractions (up to 0.5), we come with a very peculiar dependence for the total blueshift. The blueshift demonstrates its maximum value around exciton fractions corresponding to the highest output of the Dawson function. Finally, we would like to emphasize the importance of the cavity mode energy renormalization term in connection to commonly-recognized hallmarks of polariton condensation in organic, namely the blueshift [10,13,15–17,49,70]. It turns out a system may also demonstrate the blueshift above condensation threshold being even uncoupled with a cavity mode since the saturation of optical transition invokes the change in the real part of the cavity refractive index that pulls mode energy towards higher values.

Bibliography

[1]   T. H. Maiman, Nature **187**, 493 (1960).

[2]   M. Dantus, R. M. Bowman, and A. H. Zewail, Nature **343**, 737 (1990).

[3]   O. Svelto, *Principles of Lasers* (Springer US, Boston, MA, 2010).

[4]   K. R. Nambair, *Lasers: Principles, Types and Applications* (New Age International (P) Limited, New Delhi, 2004).

[5]   P. P. Sorokin and J. R. Lankard, IBM J. Res. Dev. **10**, 162 (1966).

[6]   F. P. Schäfer, W. Schmidt, and J. Volze, Appl. Phys. Lett. **9**, 306 (1966).

[7]   B. H. Soffer and B. B. McFarland, Appl. Phys. Lett. **10**, 266 (1967).

[8]   A. Imamoglu, R. J. Ram, S. Pau, and Y. Yamamoto, Phys. Rev. A **53**, 4250 (1996).

[9]   H. Deng, D. Press, S. Götzinger, G. S. Solomon, R. Hey, K. H. Ploog, and Y. Yamamoto, Phys. Rev. Lett. **97**, 146402 (2006).

[10]   C. P. Dietrich, A. Steude, L. Tropf, M. Schubert, N. M. Kronenberg, K. Ostermann, S. Höfling, and M. C. Gather, Sci. Adv. **2**, e1600666 (2016).

[11]   D. G. Lidzey, D. D. C. Bradley, M. S. Skolnick, T. Virgili, S. Walker, and D. M. Whittaker, Nature **395**, 53 (1998).

[12]   S. Kéna-Cohen and S. R. Forrest, Nat. Photonics **4**, 371 (2010).

[13]   J. D. Plumhof, T. Stöferle, L. Mai, U. Scherf, and R. F. Mahrt, Nat. Mater. **13**, 247 (2014).

[14]   K. S. Daskalakis, S. A. Maier, R. Murray, and S. Kéna-Cohen, Nat. Mater. **13**, 271 (2014).

[15]   M. Gather, M. Dusel, S. Höfling, S. Betzold, C. P. Dietrich, M. Emmerling, L. Tropf, M. Schubert, N. M. Kronenberg, J. Ohmer, and U. Fischer, in *Quantum Sens. Nano Electron. Photonics XV*, edited by M. Razeghi, G. J. Brown, G. Leo, and J. S. Lewis (SPIE, 2018), p. 66.

[16]   T. Cookson, K. Georgiou, A. Zasedatelev, R. T. Grant, T. Virgili, M. Cavazzini, F. Galeotti, C. Clark, N. G. Berloff, D. G. Lidzey, and P. G. Lagoudakis, Adv. Opt. Mater. **5**, 1700203 (2017).

[17]   D. Sannikov, T. Yagafarov, K. Georgiou, A. Zasedatelev, A. Baranikov, L. Gai, Z.

Shen, D. Lidzey, and P. Lagoudakis, Adv. Opt. Mater. 1900163 (2019).

[18] S. K. Rajendran, M. Wei, H. Ohadi, A. Ruseckas, G. A. Turnbull, and I. D. W. Samuel, Adv. Opt. Mater. 1801791 (2019).

[19] M. Vladimirova, S. Cronenberger, D. Scalbert, K. V. Kavokin, A. Miard, A. Lemaître, J. Bloch, D. Solnyshkov, G. Malpuech, and A. V. Kavokin, Phys. Rev. B **82**, 075301 (2010).

[20] Y. Sun, Y. Yoon, M. Steger, G. Liu, L. N. Pfeiffer, K. West, D. W. Snoke, and K. A. Nelson, Nat. Phys. **13**, 870 (2017).

[21] A. Yariv, *Optical Electronics in Modern Communications* (Oxford University Press, New York, 1997).

[22] A. H. W. Choi, *Handbook of Optical Microcavities*, 1st Editio (Jenny Stanford Publishing, New York, 2014).

[23] A. Kavokin, J. J. Baumberg, G. Malpuech, and F. P. Laussy, *Microcavities* (Oxford University Press, 2007).

[24] E. Kamman, On the Dynamics of Spinor Condensates in Microcavities, UNIVERSITY OF SOUTHAMPTON, 2013.

[25] B. E. A. Saleh and M. C. Teich, *Fundamentals of Photonics* (John Wiley & Sons, Inc., New York, USA, 1991).

[26] D. S. Chemla and L. Zyss, *Nonlinear Optical Properties of Organic Molecules and Crystals* (Academic Press, New York, 1987).

[27] I. I. Sobelman, *Atomic Spectra and Radiative Transitions* (Springer Berlin Heidelberg, Berlin, Heidelberg, 1992).

[28] J. Frenkel, Phys. Rev. **37**, 17 (1931).

[29] G. H. Wannier, Phys. Rev. **52**, 191 (1937).

[30] N. F. Mott, Trans. Faraday Soc. **34**, 500 (1938).

[31] P. Martin and C. E. Swenberg, *Electronic Processes in Organic Crystals and Polymers* (Oxford University Press Inc, New York, 1999).

[32] M. Fox, *Quantum Optics: An Introduction* (Oxford University Press, USA, 2006).

[33] C. Weisbuch, M. Nishioka, A. Ishikawa, and Y. Arakawa, Phys. Rev. Lett. **69**, 3314

(1992).

[34] L. Novotny, Am. J. Phys. **78**, 1199 (2010).

[35] S. R.-K. Rodriguez, Eur. J. Phys. **37**, 025802 (2016).

[36] R. Houdré, C. Weisbuch, R. P. Stanley, U. Oesterle, P. Pellandini, and M. Ilegems, Phys. Rev. Lett. **73**, 2043 (1994).

[37] D. Comoretto, *Organic and Hybrid Photonic Crystals* (Springer International Publishing, Cham, 2015).

[38] Y. Yamamoto, F. Tassone, and H. Cao, *Semiconductor Cavity Quantum Electrodynamics* (Springer Science & Business Media, New York, 2000).

[39] M. Grundmann, *Nano-Optoelectronics : Concepts, Physics and Devices* (Springer-Verlag Berlin and Heidelberg GmbH & Co. KG, Berlin, Germany, 2002).

[40] A. Imamoğlu, Phys. Rev. B **57**, R4195 (1998).

[41] A. I. Tartakovskii, M. S. Skolnick, D. N. Krizhanovskii, V. D. Kulakovskii, R. M. Stevenson, R. Butté, J. J. Baumberg, D. M. Whittaker, and J. S. Roberts, Adv. Mater. **13**, 1725 (2001).

[42] B. Deveaud-Plédran, Nat. Photonics **6**, 205 (2012).

[43] L. V. Butov, Nature **447**, 540 (2007).

[44] L. V. Butov and A. V. Kavokin, Nat. Photonics **6**, 2 (2012).

[45] E. Kammann, H. Ohadi, M. Maragkou, A. V. Kavokin, and P. G. Lagoudakis, (2011).

[46] M. Litinskaya, P. Reineker, and V. M. Agranovich, J. Lumin. **110**, 364 (2004).

[47] J. Goodman, *Introduction to Fourier Optics* (Roberts and Company Publishers, 2005).

[48] D. W. Snoke and J. Keeling, Phys. Today **70**, 54 (2017).

[49] D. Sanvitto and S. Kéna-Cohen, Nat. Mater. **15**, 1061 (2016).

[50] D. G. Lidzey, D. D. C. Bradley, T. Virgili, A. Armitage, M. S. Skolnick, and S. Walker, Phys. Rev. Lett. **82**, 3316 (1999).

[51] P. Tsotsis, P. S. Eldridge, T. Gao, S. I. Tsintzos, Z. Hatzopoulos, and P. G. Savvidis, New J. Phys. **14**, 023060 (2012).

[52]   K. Georgiou, P. Michetti, L. Gai, M. Cavazzini, Z. Shen, and D. G. Lidzey, ACS Photonics **5**, 258 (2018).

[53]   S. B. Aziz, S. Hussein, A. M. Hussein, and S. R. Saeed, Int. J. Met. **2013**, 1 (2013).

[54]   F. J. Lu, E. Benedetti, and S. L. Hsu, Macromolecules **16**, 1525 (1983).

[55]   C. P. Tripp and M. L. Hair, Langmuir **8**, 241 (1992).

[56]   J. Lub, F. C. B. M. van Vroonhoven, E. Bruninx, and A. Benninghoven, Polymer (Guildf). **30**, 40 (1989).

[57]   R. S. Gurjar, V. Backman, L. T. Perelman, I. Georgakoudi, K. Badizadegan, I. Itzkan, R. R. Dasari, and M. S. Feld, Nat. Med. **7**, 1245 (2001).

[58]   R. K. Yonkoski and D. S. Soane, J. Appl. Phys. **72**, 725 (1992).

[59]   L. W. Casperson, Opt. Commun. **8**, 85 (1973).

[60]   J. B. Moreno, G. A. Fisk, and J. M. Hoffman, J. Appl. Phys. **48**, 238 (1977).

[61]   J. M. Hvam, J. Appl. Phys. **49**, 3124 (1978).

[62]   P. J. Martin, H. A. Macleod, R. P. Netterfield, C. G. Pacey, and W. G. Sainty, Appl. Opt. **22**, 178 (1983).

[63]   D. Depla and S. Mahieu, *Reactive Sputter Deposition* (Springer Berlin Heidelberg, Berlin, Heidelberg, 2008).

[64]   M. Born and E. Wolf, *Principles of Optics: Electromagnetic Theory of Propagation, Interference and Diffraction of Light*, 6th editio (Pergamon Press, Canada, 1980).

[65]   N. A. Reinke, C. Ackermann, and W. Brütting, Opt. Commun. **266**, 191 (2006).

[66]   E. M. Calzado, J. M. Villalvilla, P. G. Boj, J. A. Quintana, V. Navarro-Fuster, A. Retolaza, S. Merino, and M. A. Díaz-García, Appl. Phys. Lett. **101**, 223303 (2012).

[67]   T. Kunkel, S. Daly, S. Miller, and J. Froehlich, in *High Dyn. Range Video* (Elsevier, 2016), pp. 391–430.

[68]   N. P. Barnes, IEEE J. Sel. Top. Quantum Electron. **13**, 435 (2007).

[69]   A. Loudet and K. Burgess, Chem. Rev. **107**, 4891 (2007).

[70]   A. V. Zasedatelev, A. V. Baranikov, D. Urbonas, F. Scafirimuto, U. Scherf, T. Stöferle, R. F. Mahrt, and P. G. Lagoudakis, Nat. Photonics **13**, 378 (2019).

[71]   G. Lerario, A. Fieramosca, F. Barachati, D. Ballarini, K. S. Daskalakis, L. Dominici,

M. De Giorgi, S. A. Maier, G. Gigli, S. Kéna-Cohen, and D. Sanvitto, Nat. Phys. **13**, 837 (2017).

[72] C. Ciuti, V. Savona, C. Piermarocchi, A. Quattropani, and P. Schwendimann, Phys. Rev. B **58**, 7926 (1998).

[73] V. M. Agranovich and B. S. Toshich, Sov. Phys. JETP **26**, 104 (1968).

[74] M. Litinskaya, Phys. Rev. B **77**, 155325 (2008).

[75] V. M. Agranovich, M. Litinskaia, and D. G. Lidzey, Phys. Rev. B **67**, 085311 (2003).

[76] V. M. Agranovich and Y. N. Gartstein, Phys. Rev. B **75**, 075302 (2007).

[77] K. S. Daskalakis, S. A. Maier, and S. Kéna-Cohen, Phys. Rev. Lett. **115**, 035301 (2015).

[78] H. A. Sturges, J. Am. Stat. Assoc. **21**, 65 (1926).

[79] S. Yokoyama, T. Araki, and N. Suzuki, Appl. Opt. **33**, 358 (1994).

[80] E. Allaria, C. Spezzani, and G. De Ninno, (2011).

[81] Y.-F. Chou, K.-L. Deng, and J. Wang, Opt. Lett. **18**, 1247 (1993).

[82] S. Gupta, K. L. Moore, K. W. Murch, and D. M. Stamper-Kurn, (2007).

[83] M. Sheik-bahae, A. A. Said, and E. W. Van Stryland, Opt. Lett. **14**, 955 (1989).

[84] M. Sheik-Bahae, A. A. Said, T.-H. Wei, D. J. Hagan, and E. W. Van Stryland, IEEE J. Quantum Electron. **26**, 760 (1990).

[85] R. L. Sutherland, *Handbook of Nonlinear Optics* (CRC Press, 2003).

[86] A. S. Brichkin, S. I. Novikov, A. V. Larionov, V. D. Kulakovskii, M. M. Glazov, C. Schneider, S. Höfling, M. Kamp, and A. Forchel, Phys. Rev. B **84**, 195301 (2011).

[87] N. Peyghambarian, S. Koch, and A. Mysyrowicz, *Introduction to Semiconductor Optics* (1993).

[88] K. S. Daskalakis, S. A. Maier, R. Murray, and S. Kéna-Cohen, Nat. Mater. **13**, 271 (2014).

[89] A. Toffoletti, Z. Wang, J. Zhao, M. Tommasini, and A. Barbon, Phys. Chem. Chem. Phys. **20**, 20497 (2018).

[90] M. H. Chang, M. J. Frampton, H. L. Anderson, and L. M. Herz, Phys. Rev. Lett. **98**,

027402 (2007).

[91] A. J. Musser, S. K. Rajendran, K. Georgiou, L. Gai, R. T. Grant, Z. Shen, M. Cavazzini, A. Ruseckas, G. A. Turnbull, I. D. W. Samuel, J. Clark, and D. G. Lidzey, J. Mater. Chem. C **5**, 8380 (2017).

[92] T. Michalsky, M. Wille, M. Grundmann, and R. Schmidt-Grund, Nano Lett. **18**, 6820 (2018).

[93] P. M. Rajanna, E. P. Gilshteyn, T. Yagafarov, A. K. Aleekseeva, A. S. Anisimov, A. Neumüller, O. Sergeev, S. Bereznev, J. Maricheva, and A. G. Nasibulin, Nanotechnology **29**, 105404 (2018).

[94] M. Arikan, R. T. Pepino, S. Ingvarsson, and I. Shelykh, Superlattices Microstruct. **47**, 139 (2010).

[95] R. T. Grant, P. Michetti, A. J. Musser, P. Gregoire, T. Virgili, E. Vella, M. Cavazzini, K. Georgiou, F. Galeotti, C. Clark, J. Clark, C. Silva, and D. G. Lidzey, Adv. Opt. Mater. **4**, 1615 (2016).

[96] L. Mazza, S. Kéna-Cohen, P. Michetti, and G. C. La Rocca, Phys. Rev. B **88**, 075321 (2013).